Heterogeneous Active Matter in Confined Spaces: theory and simulations

Vladimir Khodygo

Institute of Biology, Environmental and Rural Sciences

&

Institute of Mathematics, Physics and Computer Science

Aberystwyth University

A thesis submitted for the degree of

Doctor of Philosophy

December 1, 2020

Statement of Originality

Word Count of thesis: 24206 words

Declaration

This work has not previously been accepted in substance for any degree and is not being concurrently submitted in candidature for any degree.

Signed ..... (candidate)

Date .....

Statement 1

This thesis is the result of my own investigations, except where otherwise stated. Where correction services have been used, the extent and nature of the correction is clearly marked in a footnote(s).

Other sources are acknowledged by footnotes giving explicit references. A bibliography is appended.

Signed ..... (candidate)

Date .....

Statement 2

I hereby give consent for my thesis, if accepted, to be available for photocopying and for inter-library loan, and for the title and summary to be made available to outside organisations.

Signed ..... (candidate)

Date .....

To *Kate*, for your endless patience and support.

A beginning is the time for taking the most delicate care that the balances are correct.

F. Herbert "Dune"

Acknowledgements

Firstly, I would like to thank Martin Swain and Adil Mughal for offering such an amazing opportunity to work on this project. Both of you were patient enough to let me take my time. I'm also grateful for all that guidance and support through the whole PhD.

I want to thank folks from the Math Department and from the Bioinformatics group for all the discussions — both scientific and non-scientific — and surely for all the food and drinks we shared over the years. It was really nice as I formally wasn't involved in the activity of both parties. I should especially mention Arthur Morris as the person who convinced me to keep the office window open — and that is not so surprising considering your regular weekend adventures. Kudos to Francesca Zaccagnino for organizing many of those lovely evening events and inviting me over.

I would also like to express my gratitude to both IBERS and IMPACS for the scholarship and COST Action for financial help that allowed me to visit other research groups. Additional thanks to the Supercomputing Wales project for provided hospitality and computational resources. As any other MD-based research, active matter can be costly in terms of data volume and computational hours, letting a single person use 10% of the whole cluster storage for such a long time was very kind of you.

Finally, I should say 'thank you' to my friends (both *Sasha*s, *Vladimir*, *Alex* and all members of *Polozov seminars*) who — one way or another

— helped me during my PhD. Your patience is too great even for an average-sized deity.

Abstract

In this project I studied the collective behaviour of dense swarms of rod-shaped particles with heterogeneous properties. I consider confined systems as well as unbounded domains with periodic boundary conditions and (ir-)regular obstacles of various nature. All results that I provide are based on my own molecular dynamics based code and can be used in various cases of collective behaviour such as bacterial motion, artificial active particles (swarm robotics), animal interaction, for example, flocking of birds or schooling of fish or even crowd control.

Ch. 1 provides an introduction to active matter. I give a brief explanation of this phenomena and provide various examples that naturally arise in living and artificial systems. I also discuss various models of active matter, including the one that is used in the following chapters, and their pros and cons.

In Ch. 2, I thoroughly discuss the model for heterogeneous active matter I present it as an extension for an existing method to simulate homogeneous self-motile particles. I also provide the numerical background for the simulation code as well as some solutions to particular problems that come out in computer simulations of confined heterogeneous active matter. The results will be submitted in the form of a computational package in the near future.

Ch. 3 introduces self-propelled rods moving in a periodic (quasi-) 2D channel. I start with conventional active systems where all particles are identical. I compare them to systems where rods have heterogeneous properties i.e. every active particle has its own hardness and/or self-propellant force picked from a given distribution. I study how this introduced heterogeneity affects the resulting distribution of active matter in the confinement comparing to homogeneous systems. The results of this study have been published in *Physical Review E* [1].

In Ch. 4, the statistical properties of the homogeneous active matter are given using the mean square displacement and the so-called giant density fluctuations metric. This part of the thesis shows how a variety of behaviours emerges in confined systems of self-motile rods. The main finding here is that all patterns of motion observed in such systems can be arranged according to the corresponding values of the metrics above.

Conclusions and the perspective of all unanswered questions are given in Ch. 5. Whereas the area of active matter has been developed for more than 20 years, many problems still have to be solved. This chapter provides a potential direction of further active matter development as well as a summary of the thesis.

Contents

List of Figures

Chapter 1

Introduction

1.1 Active matter

Active matter is defined as a condensed state of matter [1] which is out of thermodynamical equilibrium [4, 5]:

- In such systems every *"active agent"* consumes energy to propel itself through the surrounding medium.
- The direction of propulsion is defined by the orientation of the particle.
- Self-propelled motion is force-free in the sense that the forces that particle and fluid exert on each other cancel out. Motion exists due to self-propellant force (SPF).

A few examples of active matter are given in Fig. 1.1, these include a group of ants, fish and birds.

To my best knowledge, the very first attempt to simulate active matter was in 1987 [6]. The original paper describes general rules for the simulation of bird flocks. It provides basic results such as aggregate motion of the simulated a flock (although, the simulation is limited due to hardware constraints of the time and also due to the simplicity of the model). The simulation is based on individuals following the same rules:

[1] Evolution of such system can't be represented as evolution of separate particles.

a) b) c)

Figure 1.1: a) A swarm of ants which have discovered a food source. b) Schooling predator bluefin size up schooling anchovies. c) A swarm-like flock of starlings. (Courtesy of Wikipedia)

- avoid collisions with nearby flockmates,
- attempt to match velocity with nearby flockmates,
- attempt to stay close to nearby flockmates.

This interaction can be approximated by a simple pairwise potential, which is repulsive at short distances (to prevent collisions) and attractive at long distances (to keep all the flockmates together). From which it follows that there is an optimal distance between neighbours.

1.1.1 Agent classification

Current research in active matter is concentrated around (but not limited by) several main topics: colloids, crowd and animal behaviour, and bacterial swarms.

- **Flocks of birds and shoals of fishes** It's a common behaviour in nature for living creatures to move in groups. It appears to be a good mechanism for defence against predators, it also enhances foraging at the same time leading to excessive competition within the group [7–9]. However, increasing of the pack size doesn't work well for every species [10].

  I've already mentioned early simulations of interacting birds, however, recent computer analysis of real-time dynamics reveals that contrary to the expecta-

tions *Sturnus vulgaris* adjust to the motion of the flock by measuring topological distance (i.e. the number of neighbours) rather than conventional metric distance [11]. Statistical analysis of flocks of hundreds to a few thousand of individuals has revealed that a typical starling interacts mostly with its 6 or 7 closest neighbours, regardless of the flock density (see also Ref. [12] for an analytical model based on metric-free interactions). Such activity has its own benefit such as improved safety [11]. It allows the flock to avoid large density changes. At the same time, more recent observations [13] of another bird species *Chaetura pelagica* shows exactly the opposite — i.e., that they prefer to stay at some distance from their neighbours.

- **Colloidal particles** A Janus particle has two surfaces with distinct physical properties. One side of the Janus particle is chemically or physically active [14]. This result in a chemical gradient which propells the particle (self-diffusiophoresis). The resulting dynamics is governed by equations similar to those used for bacterial motion [15]. Current research is concentrated on the control of self-assembly [16] and the development of functional nanoparticles [17].

- **Swarms of locusts** Despite the fact that locusts are not truly social insects — they do not need to stay in a group to breed and do not need a social organization — they exhibit collective (swarming) behaviour. For example, recent studies [18] of *Schistocerca gregaria* show that these insects in their non-flying state can form huge collective marching units which forage all vegetation in their path. Such coherent motion can possibly be explained by cannibalism: insects in the group tend to bite their neighbours but at the same time risk to get bitten themselves [18–20].

- **Collective human behaviour** Collective human behaviour can range from extreme dynamics in confined spaces [21] (where conventional social norms are dominated by purely physical interactions e.g. in moshpits [22]) to pedestrian interactions [23, 24] and highway jamming [25]. Such studies may potentially help with real-time crowd management and attendee protection during large social events [21].

- **Swarming bacteria, algae and sperm cells** According to Kearns [26], swarming motility is defined as a rapid multicellular movement of bacteria across a surface, powered by rotating flagella. However, this definition does not cover all those phenotypes that are associated with swarming motility [27] despite it being simple, accurate and mechanistically meaningful. Furthermore, it is important to distinguish swarming from behaviours such as swimming, twitching, gliding and sliding, which can also occur within or on top of solid surfaces (see Fig. 1.2).

  In a broad sense, swimming is a type of motility that happens in a bulk fluid by rotation of one or more flagella [26, 28] whereas all other types happen on a surface [26, 28]. There is no collective component, all cells move randomly and individually [26].

  According to [27] twitching is not related to flagella but rather to the presence of pili [26, 28]. It can be characterized by small displacements, frequent change of the direction of motion, not necessary in the direction of long axis [27].

  Sliding is different comparing to other types of motion in the sense that it is associated with colonies of organisms rather than with individuals [27]. The source of motion in this case is the growth of cells. Whereas the position changes cannot be perceptible, the shift of the colony border is actually observable [27].

Another type of surface motion — gliding — doesn't need flagella or pili, it happens by the means of focal adhesion complexes [26, 28]. According to observations [27], it occurs only when the cells are actually in contact with the surface.

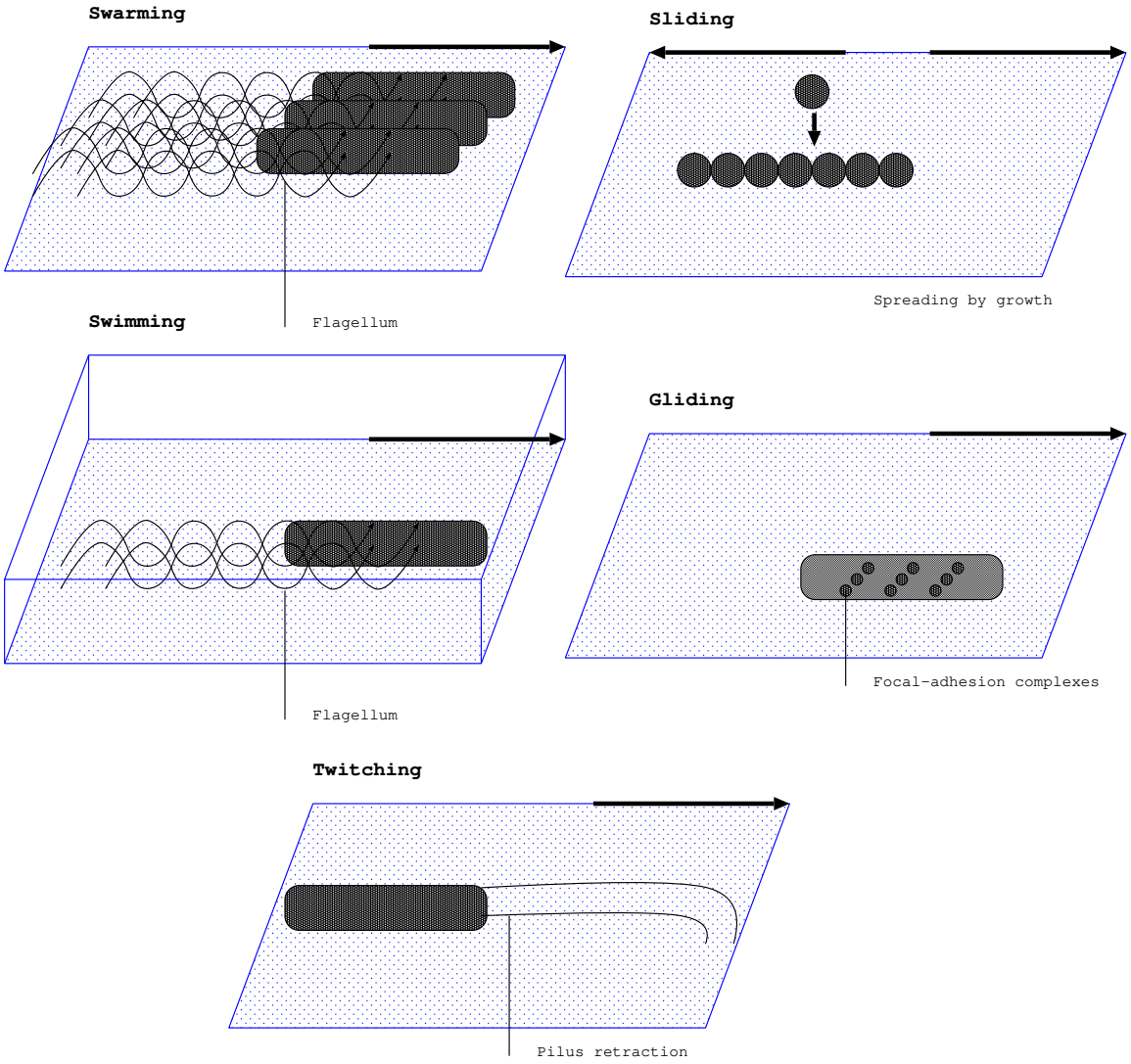

Figure 1.2: This simplistic diagram shows various mechanisms of cellular motion described in the text above. Black arrows denote the direction of motion.

1.1.2 'Dry' and 'wet' active matter

Active matter[2] systems are classed as either "wet" or "dry". In the case of wet systems the agents propel themselves by propagating through a fluid. In general the hydrodynamic forces generated by swimming have to be modelled explicitly. The effect can be significant when there are external boundaries in the system [29, 30]. Recent computer measurements of hydrodynamic friction coefficients show quantitative agreement with experimental results of swimming *Escherichia coli* [31]. In the case of dry active matter the effect of the fluid is negligible (or non-existent). Nevertheless, the surrounding medium still can implicitly affect the resulting motion through the friction coefficients (see, for instance, Ref. [32]). In the limit of low Reynolds number bacterial colonies can be modelled as a dry system [33].

It is worthy to mention one recent work by Wioland *et al.* [34]. In this paper computer simulations of active matter and real experiments show that confinement in long and narrow microchannels stabilises bacterial motion. The resulting dynamics is classed as a steady unidirectional circulation rather than turbulent motion. The simulation reveals the crucial role that bacteria-driven fluid flows can play in the dynamics. In particular, cells close to the channel wall produce strong flows which advect cells in the bulk against their swimming direction.

1.1.3 Active matter in confinement

This project seeks to model systems where bacterial colonies are confined by a boundary. By confinement here I understand an obstacle presented in the domain such that it completely prevents active particles from moving to the infinity in one or more spatial directions. However, realistically speaking boundary effects in systems studied in this thesis are not observed at distances one order of magnitude longer than the particle's length. Thus, one has to consider effects that can be caused

[2]Here and below by active matter I mean bacteria unless otherwise stated.

by interactions between active particles and boundaries. For example, systems with non-trivial [3] boundary conditions reduce not only the degrees of freedom with respect to the 3D theory but also the number of viscosity coefficients [35]. In addition, it is possible to control collective behaviour in active systems using artificial obstacles. For instance, it is possible to create a 'Maxwell's demon': a system containing asymmetric fixed ratchets to sort particles [36–38]. The domain initially populated uniformly with active particles gets passively split into two areas, with lower and higher particle concentrations. In this way one rectifies a system of active agents [39]. At the same time, when a ratchet is not fixed in space, it is possible to induce its motility when necessary [36, 40]. It still aggregates active particles inside, however, their orientations are distributed non-uniformly resulting in a non-zero force acting on a wedge.

In confined active systems it is possible to observe an accumulation of self-propelled particles at the bounding walls [1, 41]. I simulate such systems in Ch. 3. I provide results and give a detailed explanation of this behaviour. In addition, boundaries of a particular form may lead to other effects, when, for example, clockwise-directional circle swimmers — which are driven by a constant force and torque — move counter-clockwise in Petri dish- and ring-like confinement [42]. Early studies that involved complex models with additional effects such as nutrient diffusion, reproduction, and sporulation (i.e. bacteria get dormant and stop self-propelling) of bacteria, have shown that ring-like confinement leads to formation of a stationary vortex state [43]. Nevertheless, even simple pairwise interactions of active particles in a ring-like confinement lead to stabilization of the bacterial suspension into a spiral vortex [44].

Quite peculiar behaviour exists when the shape of boundaries is far from trivial (i.e. disk- or rectangle-shaped). For example, in Ref. [34] authors show that confinement into a long and narrow macroscopic 'racetrack' geometry stabilises bacterial motion to form a steady unidirectional circulation similar to that observed in [43]. It

[3] By trivial I mean periodic boundary conditions (PBC).

leads to a simple conclusion: in domains with resembling geometry we should observe similar effects, i.e., those effects are caused by the geometry of the boundary as well as its topology. Another paper by Lee [45] contains analytical calculations of how the aggregation at the walls varies with the physical parameters of the system such as diffusion coefficients. It has been shown in Ref. [46] that in such confined systems highest-order hydrodynamical particle-wall interactions lead to oscillating behaviour (active rods have sinusoidal trajectories) which occurs even far from the confining walls. There are some theoretical studies which describe general behaviour of self-propelled particles in systems with non-convex boundary with curves and corners [47, 48].

When I talk about such systems I have to discuss possible applications as well. I start with a brief mention of passive systems which can be used as a basis for further studies of active systems. It is possible to engineer tube shapes to control confined transport [49]. Particular confinements can help with the control of dynamic properties as well, for instance, to increase or decrease the transport of matter across the system [50]. When it comes to active particles, it is worthy to mention again Ref. [34] where authors provide an example of a controllable system. There are some papers about experimental setups (see, for example, Ref. [51]), where it's been shown how to create microscopic channels with irregular boundaries to prevent biofilm formation in certain systems. One of recent researches shows how one can separate the particles in a channel using the balance between the self-propelled speed and the particle radius [52]. It happens due to the competition between self-propulsion and the combined alternating or direct current external forces. Moreover, systems which contain particles with different motilities exhibit spontaneous segregation [53]. The mechanism is understood as a function of particle velocities, particle density, or channel width.

To sum up, it is possible to use active matter for targeted delivery of drugs or

materials. Different strains of the same bacterial type can have different properties such as size, motility etc. Sorting of bacteria can potentially help with separation of such strains. Finally, bacteria can be removed from the stream or vice versa — concentrated far from the walls by employing various confinement geometries.

1.2 Background

1.2.1 Vicsek and Toner-Tu models

The most basic models of active particles interaction do not involve the surrounding medium, meaning that only interactions between active agents are considered (see Ref. [5] and references therein). Each point-like particle moves with a constant speed in a particular direction. When it has one or more neighbours within a given radius, the particle interacts with them through changing the direction of motion. This direction is realigned to coincide with its local mean value. Then the particle's position is shifted along this vector [54]. All Vicsek-like models are similar to the continuous-spin magnets. That means that they display a phase transition from an initially disordered state to a coherent phase. Fig. 1.3 provides an example where a system of particles is shown to evolve from a non-aligned to an aligned state. Comparing to planar spin models, such flocks exhibit a long-range order even in two dimensions (see Ref. [5] and references therein).

The position vector $\boldsymbol{r}$ of a single particle α evolves according to the following equation:

$$\boldsymbol{r}_\alpha(t + \Delta t) = \boldsymbol{r}_\alpha(t) + \boldsymbol{v}_\alpha(t)\Delta t. \tag{1.1}$$

Here, the self-propellant term $\boldsymbol{v}_\alpha(t + \Delta t)$ is constructed as a product of a constant speed v and the orientation vector based on the angle $\Theta(t + \Delta t)$.

$$\Theta(t + \Delta t) = \langle \Theta(t) \rangle_r + \Delta\Theta, \tag{1.2}$$

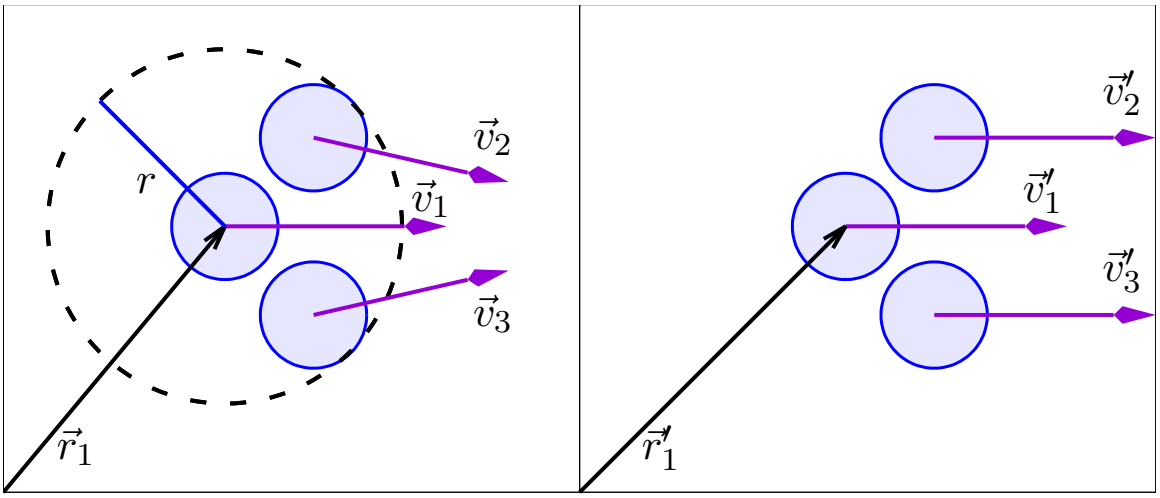

Figure 1.3: Diagram of Vicsek model. Solid disks denote particles, (magenta) vectors stand for velocities of particles whereas Solid (black) vectors mark positions of particles. Solid (blue) line denotes the radius of interaction r of the model. The (black) dashed circle covers the area of interaction. Left: particles at time t. Right: particles at time $t + \Delta t$, where their velocities are aligned according to the rule described in the text below. Primed labels denote updated variables.

where $\langle\cdot\rangle_r$ denotes the spatial average for all particles within a given radius r around a particular particle α. $\Delta\Theta$ term is responsible for noise corrections, the original research [54] used a uniformly distributed variable $[-\Theta'/2, \Theta'/2]$, contrary to the more widespread Gaussian noise [55, 56]. There Θ' served as one of the control parameters in the system, along with the number density and the amplitude of the self-propellant force.

Toner and Tu [57] suggested a continuous counterpart for the Vicsek model. The dynamics of the velocity field $\boldsymbol{v}$ now is given by the equations below.

The first equation 1.3 is responsible for conservation of active matter. The modified version of the Navier-Stokes equation given by Eq. 1.4 describes the state of active liquid, where additional terms are responsible for self-propulsion and collective behaviour. Finally, the last equation 1.5 is responsible for the effective pressure P, which depends on the mean of the local number density ρ_0. Here, $\rho(\boldsymbol{r})$ and σ_n are

coefficients in the pressure expansion.

$$\frac{\partial \rho}{\partial t} + \boldsymbol{\nabla} \cdot (\boldsymbol{v}\rho) = 0, \tag{1.3}$$

$$\frac{\partial \boldsymbol{v}}{\partial t} + (\boldsymbol{v}\cdot\boldsymbol{\nabla})\boldsymbol{v} = (A - B|\boldsymbol{v}|^2)\boldsymbol{v} - \boldsymbol{\nabla}P + D_L\boldsymbol{\nabla}(\boldsymbol{\nabla}\cdot\boldsymbol{v}) + D_1\boldsymbol{\nabla}^2\boldsymbol{v} + D_2(\boldsymbol{v}\cdot\boldsymbol{\nabla})^2\boldsymbol{v} + \boldsymbol{f}, \tag{1.4}$$

$$P = \sum^{\infty} \sigma_n(\rho - \rho_0)^n. \tag{1.5}$$

Here, $D_{L,1,2}$ are viscosity constants responsible for collective behaviour of the suspension. They are taken uniform to represent the process of alignment of particles with their neighbours [58]. The last one is the white noise term $\boldsymbol{f}$. When the noise is absent the system evolves to have all active particles moving in the same direction at constant speed [58]. The constants $A \neq 0$ ($A < 0$ and $A > 0$ for the disordered and the ordered phases, respectively) and $B > 0$ are responsible for the self-propulsion mechanism, resulting in the local self-propellant speed $\sqrt{A/B}$.

1.2.2 Naive active nematics

According to Boltzmann theory, two particles are colliding when they are within each others interaction radii [59]. Than means that any (active or not) particle can interact only with its direct neighbours and only through direct collisions. This is, in fact, an extremely short-ranged version of the Vicsek model where conventional realignment is absent. At the same time this approach allows one to simulate systems where active particles can have various shapes. I discuss the case of rod-shaped particles below (see Fig. 1.4) as the most relevant one for my studies. The dynamics of every particle evolves according to the following overdamped Langevin equations [55]

$$\eta_T \frac{d\boldsymbol{v}}{dt} = \mathcal{F}\hat{\boldsymbol{u}} + \sum \boldsymbol{F}_{int} + \boldsymbol{f}, \tag{1.6}$$

$$\eta_R \frac{d\hat{\boldsymbol{u}}}{dt} = \sum \boldsymbol{T} \times \hat{\boldsymbol{u}} + \boldsymbol{f}_R. \tag{1.7}$$

Here, constants η are responsible for translational and rotational friction where needed. The orientation of every particle is given by the unit vector $\hat{\boldsymbol{u}}$ that is affected by external torques $\boldsymbol{T}$ acting on the particle. The self-propellant force $\mathcal{F}$ is applied along the direction of motion, all pairwise collisions result in additional forces $\boldsymbol{F}_{int}$. In addition, noise terms $\boldsymbol{f}$ are added when required.

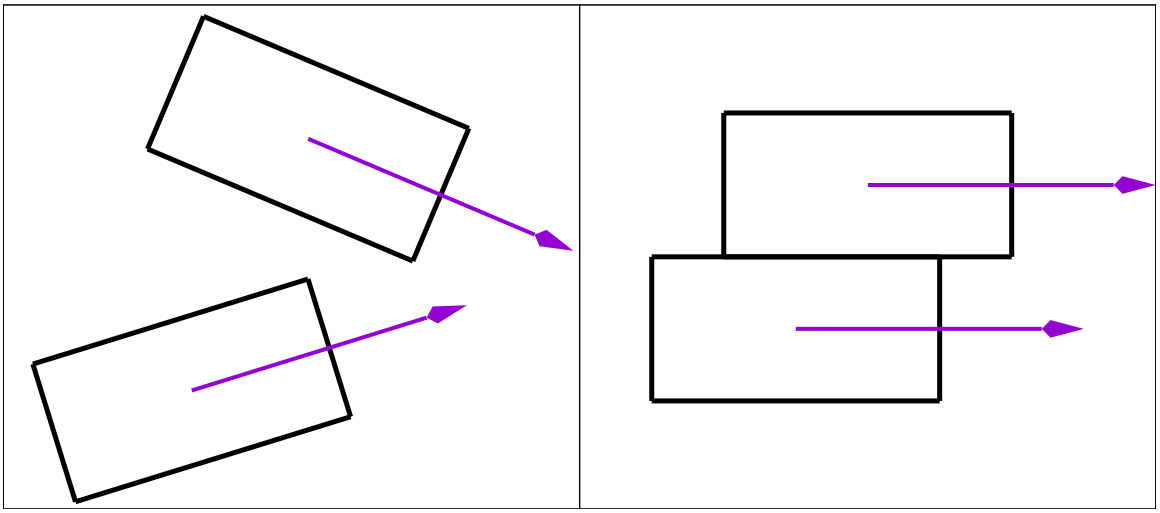

Figure 1.4: A simplistic diagram presenting naive interaction of two elongated particles. Left: rods before the collision, right: rods after the collision.

1.2.3 Pattern formation

As I mentioned earlier, both Vicsek and Toner-Tu models describe systems where every active particle can sense not only its direct neighbours but also other particles within a particular distance (I refer to Fig. 1.3 again). This can lead to some emergent patterns described below. I also provide additional examples of other common patterns that can emerge in systems with different models and/or confinements. All plots presented in Fig. 1.5 are results of my simulations.

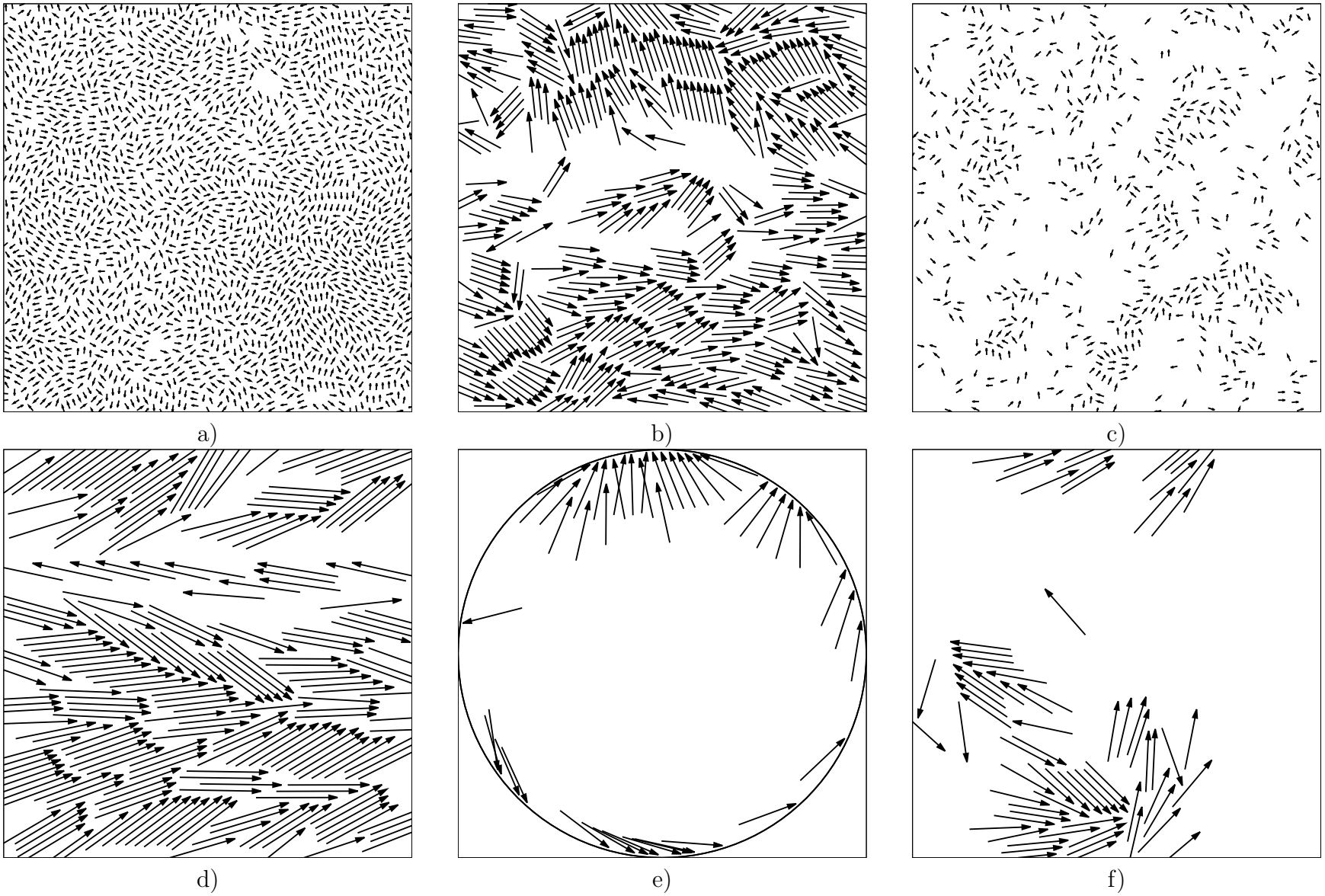

Figure 1.5: This diagram shows some of the described patterns. All active rods are represented by vectors. All simulations had enough time to relax and form some structures (if any). a) jammed short rods; b) turbulent state; c) disordered system; d) laning; e) a vortex-like formation in a disk; f) swarming rods. Figures may not show the most representative cases, they are given for illustrative purposes only.

Disordered. Low order in active Vicsek systems can be caused by low alignment strength or by low density resulting in all particles moving almost independently [54]. The same state can also be observed in systems where particles have their shape symmetry broken [55, 60, 61] — i.e., they are elongated instead of being disk-like. In summary, this is the most common pattern among all of them observed in active systems.

Uniform/Laning. The density of particles is uniform thus all their trajectories are correlated. This results in all particles moving in the same direction [54]. When a system is populated with rod-like active particles that interact through naive model [55, 60, 62] provided earlier, it is possible to observe a laning state. In this case rods do not necessarily move in the same direction but form a set of parallel streams running in the opposite directions.

Turbulence/Bionematic. According to the work of Cisneros *et al.* [63] a bionematic state is characterized by high concentration of active matter (nearly close-packed) which forms sub-domains that move chaotically and co-directionally similar to turbulence. It is also characterized by high spatial and temporal correlations of velocity and vorticity. I note that there is some discrepancy in the modern literature regarding these states. Whereas some papers consider both of them to be similar enough and to be treated as one (see, for example, Ref. [55]) there are other studies that provide a quantitative measure to separate these phases [62, 64]. However, a full discussion of this difference lies beyond the scope of this thesis.

Jamming. Active systems can also exhibit a jammed state meaning that almost all activity is suppressed. This happens in systems with no confinement (PBC), where something like glass is formed, and is caused by pairwise interactions themselves [3, 55, 61, 62] at moderately high densities. It can also happen in

confined systems, where interactions with the boundary increase local particle concentration and lead to jammed state [65].

Swarms. Active particles can form independent clusters when their density is moderately high. Within a single cluster all active swimmers move in the same direction, similar to the uniform case [54]. Rod-like particles that I introduced above can also form swarms [55, 61, 62]. However, in order to do that having relatively high density is not enough, they also have to have a high length-to-width ratio (see fig. 1.5).

Travelling bands. Active particles are localized in dense line-like formations with sparsely populated space between them; particles move along the high-density band in both directions [66]. However, other configurations are possible [60, 67–69]. Yamanaka and Ohta [70] provided another remarkable example of band formation. They studied systems of deformable self-propellant particles and have revealed that such particles can form soliton-like structures similar to those bands observed in systems with Vicsek-like models.

Vortices. Vortex formation is a universal characteristic of active matter and is not necessarily caused by presence of confining boundaries [44, 64, 71–74] but by the interaction itself [22, 67, 75–80]. It can also be a solitary object [81] or can emerge in the bulk as part of turbulence [62]. More complex structures are also observed when, for example, multiple vortices emerge [43, 63, 82–85] and form a hexagonal lattice [86, 87] (see also references [88, 89] for artificial vortex lattice formation). Moreover, formation of such non-trivial configurations is not limited by quasi-2D environments, other cases are possible where, for example, active particles exist on a surface with non-zero Gaussian curvature [90, 91] like sphere or torus. The patterns that are formed by active particles on a spherical surface are similar to what is observed in regular disk-like environments due to

presence of topological defects [92]. In addition, active particles in 3D space are capable of forming more complex patterns such as rings, toruses *etc.* (see references [81, 93] for more details).

The interplay between different models, confinements and particle shapes can result in extremely non-trivial results. For example, it is well known [44, 64] that active rods in disk-like chambers form vortices. However, real observations [94] show that this doesn't happen in systems with round self-propellant particles. At the same time, simulations of such particles in a square confinement [95] show that a vortex-like structure can be formed by them.

Exotic states. As mentioned earlier, active matter is capable of forming regular structures where every element of such an arrangement is an active vortex. Nagai *et al.* [87] have shown that in systems with a Vicsek-like model with memory more exotic states can emerge. When the memory time and the overall density are low, a vortex lattice transforms into a homogeneous disordered state. However, when the density is high enough, it becomes 'a spatiotemporally disordered cellular structure' [87] called an 'active foam'. The elements forming such a foam are the same as in the lattice, however, they are unstable. There is one more uncommon configuration that can be observed in simulations of flying flocks [96]. A single group of active particles can move as a single entity, however, a pair of particles can have their trajectories (i.e. worldlines) entangled resulting in their positions within the flock swapped.

1.2.4 Different confinements

In this thesis I concentrate my attention on collective behaviour of bacterial active matter in confined spaces. Whereas active matter itself can exhibit a lot of intriguing patterns like, for example, bands or swarms that are mentioned earlier, presence of boundaries of any kind can be of utmost importance.

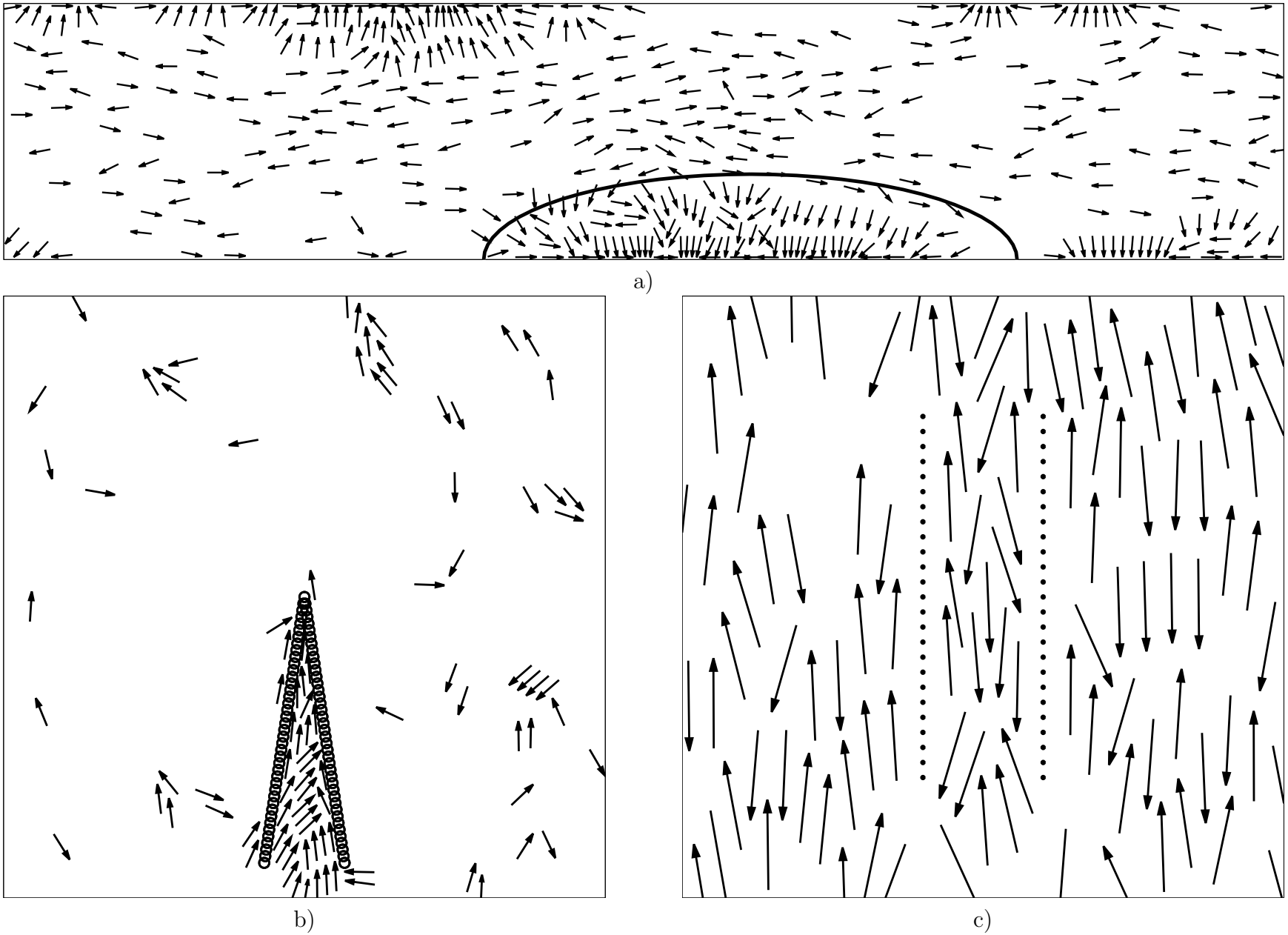

Figure 1.6: Examples of boundaries. a) a periodic channel , where hedgehogs — one of them is marked with an ellipse — are formed along horizontal walls, which are created by a continuous potential; b) a wedge formed with disk-like obstacles; c) two parallel plates formed with disk-like particles.

First, I start with the most trivial confinements: disk-like chambers and periodic channels (see figures 1.5 and 1.6) that are discussed in details in Chapter 3. Earlier studies of bacterial motion show that bacteria moving in quasi-2D microscopic droplets form vortices [44]. What's more fascinating is that there can be two or even three [65] vortices within a single disk-like chamber circulating at the same time in the opposite direction. Further studies of such systems using a continuous version of the model show that there are actually more patterns [65]. That includes the case when there is no azimuthal (clockwise or anticlockwise) flow at all meaning that the whole system is jammed. It is also possible to reach a turbulent state by tuning dynamic parameters of the system.

Collective behaviour of active particles in straight quasi-2D channels or their 3D [32, 97, 98] equivalents is also a matter of interest. Such particle formations as *hedgehogs* [1, 32] can be observed in some simulations of active rods (see Fig. 1.6). Two active rods near the bounding wall can collide and form a V-shaped configuration. Due to the resulting net force being close to zero, such a formation does not move (or does so slowly) and starts serving as a nucleation point for other active rods. The cluster of rods which are pointing towards *roughly* the same point in space is what is called a *hedgehog* [32] and can be observed in systems with planar geometry [1] as well as in 3D systems [32]. One of other intriguing phenomena is self-induced sorting of active particles in systems with bidisperse[99] or heterogeneous self-propellant forces.

Due to the effect of caging [100], a single rod-like particle can't escape its neighbours. However, when a system contains a heterogeneous population, particles with high self-motility produce higher active pressure resulting in slower particles being expelled into the interior of the domain. Since such systems do not require any external force for segregation of particles, this may be a way to create passive sorting devices.

A more advanced approach to confined active matter is simulation of custom

boundaries using disk-like (or spherical in the case of 3D systems) obstacles and merging them with simple polygonal environments creating custom microfluidic devices. Such formations can be created *in vivo* using simple lithography [88]. The variety of shapes ranges from single pins to more complex configuration like, for example, wedge-like structures. I discuss some the recent papers and their possible applications below.

Singular obstacles (not necessary disk-like) can be arranged to form an (ir-)regular lattice [101, 102] or can be placed randomly. Recent studies of the latter case have shown that presence of such obstacles can enhance the diffusivity of active rod-like particles [103]. The former case reveals some intriguing phenomena like, for instance, vortex formation [88], separation of parasites from blood [104] and separation of different type of bacteria [105]. Such configurations also have applications with regards to regular passive matter, i.e., blood or cancer cells. For example, Ref. [106] shows how a microfluidic device can be used to enrich blood with tumor cells, Davis *et al.* [107] separate blood components using the same concept whereas Wunsch *et al.* [108] go down to the nanoscale particles. In addition, it is possible to enhance regular channel walls with periodic structures to increase or decrease the rate of bacteria wall accumulation [51].

Using wedge-like obstacles in active matter simulations and experiments allows to control the direction of particle flow [101]. It is also possible to change the concentration of swimming bacteria in particular areas of the domain limited by wedges (see Ref. [36] for more detailed review, Ref. [109] for *in vivo* results).

Finally, it is possible to employ particular non-trivial geometries to reach particular results (see, for example, Ref. [110]). Hulme *et al.* [111] used a chain of joined cardioid-like chambers to direct cell movement and to sort *Escherichia coli* by length. Guidobaldi *et al.* [112] have shown that using a petal-shaped boundary actually disrupts the wall accumulation of human sperm cells. There are other studies

that explain how such periodic wall corrugations can rectify [38] self-motile particles by the self-propellant force [113].

1.3 Motivation

Conventional thermodynamics states that every system tends to minimize its own energy in order to reach a stable state. However, it works for closed systems only. There are many systems, both living and artificial, where this rule doesn't hold due to constant energy exchange. Typical examples are bacterial communities, where every bacterium uses energy sources from the surrounding medium to move itself, robotic swarms, where each robot has its own internal source of energy, or any other group of individuals (or a single individual) that is able to convert some energy to work or motion.

I am motivated by current achievements in the active matter area such as collective robotics, targeted drug delivery, crowd control and many other related fields. It is fascinating how simple interactions between active agents result in non-trivial collective behaviour. Thus, I seek seek understanding of emerging behaviour in bacterial communities in order to understand it and use for bacterial control and bacterial sorting in particular.

1.3.1 Applications

I categorize current studies of microscopic active matter as the following: transport & drug delivery, microscopic passive devices, and collective properties of active matter. Below, I provide examples of applications for each category.

Transporting of microscopic objects can be implemented in two different ways. First, it is possible to attach transported objects to active particles. For example, Ref. [114] shows how diatom microalgae-derived nanoporous biosilica are used to deliver drugs to cancer cells. The diatom *Thalassiosira pseudonana* is genetically engineered

to enable attachment of cell-targeting antibodies. Another way is to use magneto-aerotactic bacteria (i.e. *Magnetococcus marinus* strain) to deliver drug-containing nanoliposomes to tumour hypoxic regions [115]. Bacteria, each containing a chain of magnetic iron-oxide nanocrystals, tend to swim along local magnetic field lines and towards low oxygen concentrations based on a two-state aerotactic sensing system. Using self-propelling particles was proposed as a solution to deliver coagulant agents upstream through blood [116]. It was shown that in combination with active thrombin these particles worked effectively as a hemostatic agent. Second, it is possible to use non-zero resulting force formed by a set of roughly aligned bacteria to push an object. The resulting coherent motion has been shown to work as an engine *in silico* and *in vitro*. For instance, active rods are naturally aggregated within a micro-wedge moving it in a particular direction [117–119]. Also, some recent experiments show that microbots can be created by attaching bacteria to objects [120].

Modern devices in any area of application are often minimized to reduce energy consumption and to shrink their volume. However, sometimes it may lead to unexpected problems like, for instance, the impossibility to provide sufficient energy supplies to the required area where devices exist. It is virtually impossible to deliver energy locally to every microscopic element. One of the possible solutions is to use bacteria as a source of force since they can transform various types of energy to work. For instance, in Ref. [121] authors show how to create a passive microscopic water pump. Bacteria form a biofilm at the boundary of a channel, then, by aligning them in roughly the same direction it is possible to generate non-zero net fluid flux. Another remarkable work [122] shows how bacteria can be used to power microscopic engines. In systems where asymmetric gear-like rotor are placed motile *Escherichia coli* cells self-assembly along the boundaries of the obstacles and thus produce spontaneous and unidirectional rotation due to broken shape symmetry of the gears.

Active matter can exhibit many intriguing properties which can be of interest

in terms of practical applications. Below, I provide a few papers that show the importance of such studies.

Recent studies show the way to increase antibiotic sensitivity. Clusters of swarming *Bacillus subtilis* on semisolid agar are shown to exhibit enhanced resistance against antibacterial drugs due to their collective behaviour and motility. In fact, high activity of bacterial swarms prevents them from prolonged exposure to lethal drug concentrations. However, adding nontoxic polystyrene colloidal particles which are fixed on surface (i.e., corrugating the surface) leads to disruption of colonies and, therefore, to more effective action of antibiotics. Inert obstacles prevent motion of a swarm as a single entity. Bacteria have to manoeuvre, they lose their speed and group dynamics and expose themselves to a drug [123]. In a similar fashion it is possible to disrupt wall accumulation of human sperm cells by simple artificial wall corrugation [112].

It is possible to do exactly the opposite. Instead of disrupting collective dynamics it is possible to enhance it by encapsulating a bacterial swarm into a *swarmbot*. A single bacterium can't survive in a particular environment therefore all bacteria have to stay together as a single entity. It creates a perfect safeguard strategy to prevent unforeseen bacterial growth and allows to move a bacterial colony as a group as well [121]. I also show [1] (see also Ref. [53]) in Chapter 3 that some of the collective properties of active matter can be used to create an effective sorting strategy. Also, in Ref. [124] it's been shown that separation of yeast cells using a microfluidic system of conjoined spheres is possible.

Chapter 2

Active matter model

2.1 Introduction

In this chapter I introduce the numerical scheme used in the remainder of the thesis for the simulation of active rods. I start with a general model of active matter based on overdamped Langevin equations for microscopic particles. I introduce the definition of heterogeneous active matter, then I discuss various details of the model I used in my simulations. I also give a brief overview of other models and a short comparison of them to explain my choice.

2.2 Model

In this section I discuss heterogeneous active matter. Compared to homogeneous systems where all the particles are identical, in heterogeneous active matter I assume that every active agent is unique. That means each particle has at least one property such as the self-propellant force, that is different from all other particles in the system.

I provide the particular details of my model and compare it to other models used in simulations of active matter. Finally, I give a summary of various boundary conditions that can be employed in active matter simulations.

2.2.1 Heterogeneous Active Matter

I consider a (quasi-) two-dimensional (2D) system with a population of N active particles confined within a rectangular domain of length L_x, width L_y, and total area $A = L_x \times L_y$. The basic model can in principle be extended to 3D, here I restrict motion to a 2D plane. I do this to simulate systems qualitatively similar to bacterial communities in thin liquid films.

I use Greek indices to mark particles and Latin to enumerate segments of a particle comprised of disks (if any) as described below.

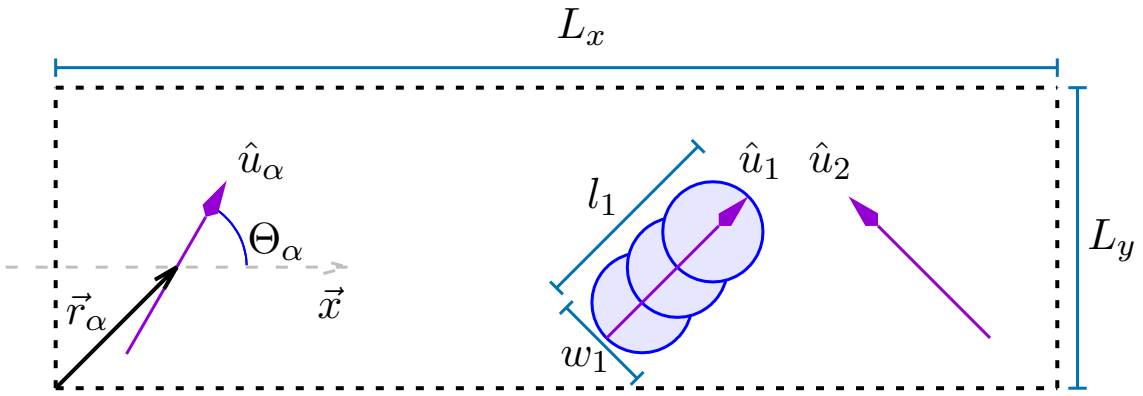

Figure 2.1: A diagram illustrating some of the variables I discuss in this subsection. An example of a segmented rod 1 comprised of three segments is given.

In this thesis all particles are assumed to be segmented rods unless otherwise stated (see Fig. 2.1). Every α^{th} particle is characterized by two dynamic variables — its centre of mass $\boldsymbol{r}_\alpha(t) = (x_\alpha(t), y_\alpha(t))$ and orientation, given by a unit vector $\hat{\boldsymbol{u}}_\alpha(t) = (\cos\Theta_\alpha, \sin\Theta_\alpha)$ (see Fig. 2.1). In addition, the population is assumed to be heterogeneous unless otherwise stated. This means that every rod is defined by a set of characteristic values such as width w_α, length l_α, and aspect ratio $a_\alpha = l_\alpha/w_\alpha, \forall\alpha = \overline{1, N}$, where $\overline{1, N}$ denotes all integer values from 1 to N inclusive. I keep the width of every rod constant so that $w_\alpha \equiv w = 1$ to reduce the total number of parameters. That means that $a_\alpha \equiv l_\alpha$ throughout the text. Furthermore, active particles move with self-propellant force $\mathcal{F}_\alpha$ applied along $\hat{\boldsymbol{u}}_\alpha$ and have hardness (softness) κ_α. Here,

κ_α defines the strength of pairwise interactions (see Sec. 2.2.2 for more details). That means that when $\kappa_\alpha = 0 \quad \forall\alpha$ there is effectively no repulsive forces between particles. I pick every variable from a corresponding continuous uniform distribution $\mathcal{U}$. However, any other suitable distribution (e.g. Gaussian) can be chosen to simulate systems close to real communities, provided that it is bounded and positive. A limiting case that I mentioned above, when such a distribution is non-negative, is when $\kappa_\alpha = 0$. Nevertheless, even with such limitations some interesting phenomena can be observed. For example, given enough time such an active gas in a periodic channel degenerates[1] from a 2D system to a 1D linear gas as presented in Fig. 2.2.

This happens because in the absence of noise the walls are the only objects in the system that can change the orientation of particles. The boundaries force all active rods to align along the direction of the channel while keeping them at the same distance from the walls themselves. Since active particles do not interact with each other, they just keep running parallel to the walls forever being in fact a 1D gas.

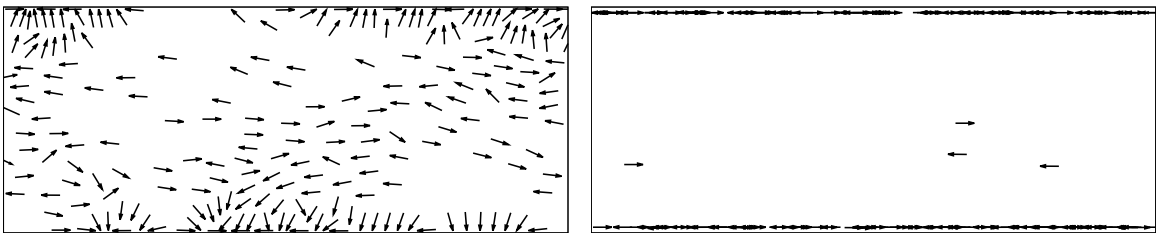

Figure 2.2: Left: a system with moderately strong repulsive forces between active rods. Right: a system where all interactions between active rods are switched off. In both cases rods are represented by vectors.

I assume that all hydrodynamic interactions are negligible (see Chapter 1 for a more detailed explanation) and, thus, any two active rods α and β interact through a repulsive potential only (i.e., "dry" active matter):

$$U_{\alpha,\beta}(\boldsymbol{r}_\alpha, \hat{\boldsymbol{u}}_\alpha, a_\alpha, \kappa_\alpha; \boldsymbol{r}_\beta, \hat{\boldsymbol{u}}_\beta, a_\beta, \kappa_\beta), \tag{2.1}$$

[1]Degeneracy here is used in its usual sense when a class of objects changes so that it belongs to another, potentially more simple, class [125].

of arbitrary nature (see, for example, references [1, 126, 127]). Here I assume two-body interactions only. I provide a more detailed description of some potentials below in this section.

In the simulations I use three different types of boundaries: periodic boundary conditions (PBC), disk-like and channel-like confinements (see figures 2.10, left and 2.13). First, when I need to explore phenomena caused by interparticle collisions only I use PBC. This is probably the most common approach which I discuss in detail later in the text. Second, when I need to restrict activity of rods in one or both spatial directions, I employ an external potential $U^b_\alpha(\boldsymbol{r}_\alpha, \hat{\boldsymbol{u}}_\alpha; a_\alpha)$ (see, for example, Ref. [1] and Chapter 3). In this case a closed domain can be simulated using a 2D potential well of some kind. I get periodic channels by combining both PBC and external potentials. More complex geometries can be incorporated, including $3D$ versions of the ones above.

Next step is to combine all the terms responsible for pairwise, boundary and self-propellant forces in one system of equations for translational and rotational motion. Given that, I have overdamped Langevin (see Chapter 1) equations for translational and rotational motion of a rod α:

$$\text{Translation} \quad \eta^T_\alpha \frac{d\boldsymbol{r}_\alpha}{dt} = -\boldsymbol{\nabla}_{\boldsymbol{r}_\alpha} \sum_{\beta\neq\alpha} U_{\alpha,\beta} - \boldsymbol{\nabla}_{\boldsymbol{r}_\alpha} U^b_\alpha + \mathcal{F}_\alpha \hat{\boldsymbol{u}}_\alpha, \tag{2.2}$$

$$\text{Rotation} \quad \eta^R_\alpha \frac{d\hat{\boldsymbol{u}}_\alpha}{dt} = -\boldsymbol{\nabla}_{\hat{\boldsymbol{u}}_\alpha} \sum_{\beta\neq\alpha} U_{\alpha,\beta} - \boldsymbol{\nabla}_{\hat{\boldsymbol{u}}_\alpha} U^b_\alpha, \tag{2.3}$$

where $\boldsymbol{\nabla}_{\boldsymbol{r}_\alpha}$ denotes the derivative w.r.t. the position of the centre of mass, and $\boldsymbol{\nabla}_{\hat{\boldsymbol{u}}_\alpha}$ is the gradient on a unit circle. Here η^T_α and η^R_α are the translational and rotational damping tensors adapted from Ref. [55]; their explicit tensor forms are given by equations 2.4 and 2.5, respectively. In both equations all pairwise interactions result in the sum of $U_{\alpha,\beta}$ gradients whereas wall collisions are given by the gradient of U^b_α. The last term containing $\mathcal{F}_\alpha$ is responsible for self-propellant motion.

2.2.1.1 Friction coefficients

I assume that there is some surrounding fluid that is viscous enough to affect translational and rotational components of motion, however, its own speed is zero everywhere. Thus, the friction coefficients take the following form (see Ref. [55]):

$$\eta_\alpha^T = f_0[f_\parallel^\alpha \hat{\boldsymbol{u}}_\alpha \otimes \hat{\boldsymbol{u}}_\alpha + f_\perp^\alpha(\mathbb{1} - \hat{\boldsymbol{u}}_\alpha \otimes \hat{\boldsymbol{u}}_\alpha)], \tag{2.4}$$

$$\eta_\alpha^R = f_0 f_R^\alpha \mathbb{1}, \tag{2.5}$$

where f_0 is a Stokesian friction coefficient and $\mathbb{1}$ is a unit tensor. The symbol $\otimes$ stands for the dyadic product. The subscripts $\{\parallel, \perp, R\}$ mark longitudinal, transversal and rotational components of rod motion, respectively. The factors $\{f_\parallel^\alpha, f_\perp^\alpha, f_R^\alpha\}$ are dimensionless and depend only on aspect ratio a_α:

$$f_\parallel^\alpha = \frac{2\pi}{\ln(a_\alpha) - 0.207 + 0.980 a_\alpha^{-1} - 0.133 a_\alpha^{-2}}, \tag{2.6}$$

$$f_\perp^\alpha = \frac{4\pi}{\ln(a_\alpha) + 0.839 + 0.185 a_\alpha^{-1} + 0.233 a_\alpha^{-2}}, \tag{2.7}$$

$$f_R^\alpha = \frac{1}{3}\frac{\pi a_\alpha^2}{\ln(a_\alpha) - 0.662 + 0.917 a_\alpha^{-1} - 0.050 a_\alpha^{-2}}. \tag{2.8}$$

These coefficients take their origin in a theory for the translational and rotational motions of extremely long cylinders ($a_\alpha \to \infty$) [128, 129]. Tirado *et al.* [130] corrected them to be valid for moderately short rods.

I plot these friction coefficients as a function of the aspect ratio a_α in Fig. 2.3. It can be seen that for rods with high aspect ratio the translational components of friction asymptotically decay to zero when $a_\alpha \to \infty$ whereas the rotational component keeps growing to infinity. From that it is possible to infer that long rods can move easily, however, it is difficult for them to change orientation. Note that the range of valid aspect ratios in the paper by Tirado *et al.* [130] starts at approximately

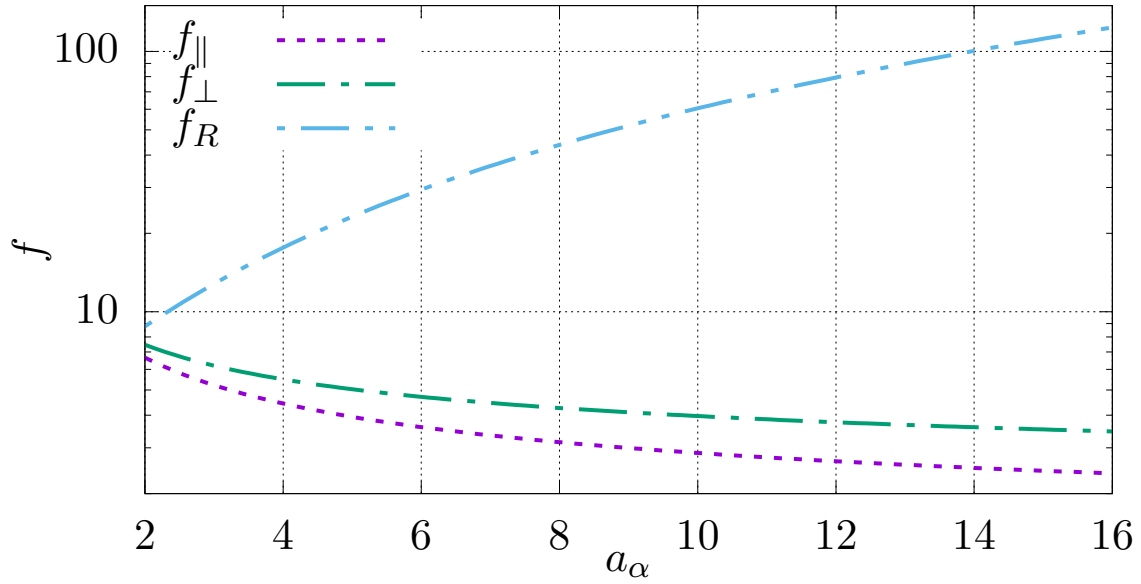

Figure 2.3: Behaviour of friction coefficients $f_\parallel$, $f_\perp$ and f_R depending on aspect ratio a_α.

$a_\alpha = 4.6$. However, since the same formulas are also used in simulations of short active rods (see, for instance, Ref. [55]) I use these coefficients assuming that they are valid in short range as well.

2.2.1.2 Units of measurements

I use a system of characteristic units as in Ref. [55] such that $f_0 = 1$, $w = 1$, and $\bar{\mathcal{F}} = 1$. Here I have to introduce a reference value of self-propellant force $\bar{\mathcal{F}}$ since I simulate systems with heterogeneous motility. All the units used in simulations are provided in the table below.

Table 2.1: System of characteristic units

Variable	Unit
f_0	1
$\bar{\mathcal{F}}$	1
w	1
Speed	$\bar{\mathcal{F}}/f_0$
Time	$\tau_0 = wf_0/\bar{\mathcal{F}}$
Energy	$\bar{\mathcal{F}}w$

2.2.1.3 Gaussian noise

It is also possible to simulate systems with rotational Gaussian noise which I introduce as an additional term $\Delta\hat{\boldsymbol{u}}_\alpha$ in Eq. 2.3 for rotational motion. It has the following properties:

$$\begin{aligned}\langle\Delta\hat{\boldsymbol{u}}_\alpha\rangle &= 0,\\ \langle\Delta\hat{\boldsymbol{u}}_\alpha(t)\Delta\hat{\boldsymbol{u}}_\beta(t')\rangle &= 2D^*_{R,\alpha}\delta_{ij}\delta_{\alpha\beta}\delta(t-t').\end{aligned}$$

An in-depth study of real bacteria confirmed by additional computer simulations [131] reveals the following features of rotational diffusion processes in bacterial active matter. First, it is non-Brownian at short times, nevertheless, its long-time behaviour is described by a regular diffusion process. However, its diffusion constant D^*_R is much larger than the Stokes-Einstein value $D_R = k_BT/f_0f_R$ (see Ref [55] and references therein for a detailed explanation). The direct consequence of this is that intrinsic random orientation changes of bacteria are much higher than those caused by thermal motion of the surrounding medium. Second, there is a phenomenological relation between bacterial parameters such as SPF and length and the effective diffusion constant D^*_R [55, 131]:

$$\frac{l_\alpha D^*_{R,\alpha} f_0 f_{\parallel,\alpha}}{\mathcal{F}_\alpha} \sim 0.01,$$

where $l_\alpha f_0 f_{\parallel,\alpha}/\mathcal{F}_\alpha$ is the characteristic time required for an active rod to traverse a distance comparable to its size. Its typical value for swimming bacteria such as *Escherichia coli* is ~ 0.01 [55, 131], for larger bacteria it can take large values due to noise in swimming mechanism rather than thermal noise of the surrounding solvent. From this equation it follows that longer and slower (in terms of self-propellant force) active rods are less prone to noise (see Fig. 2.4).

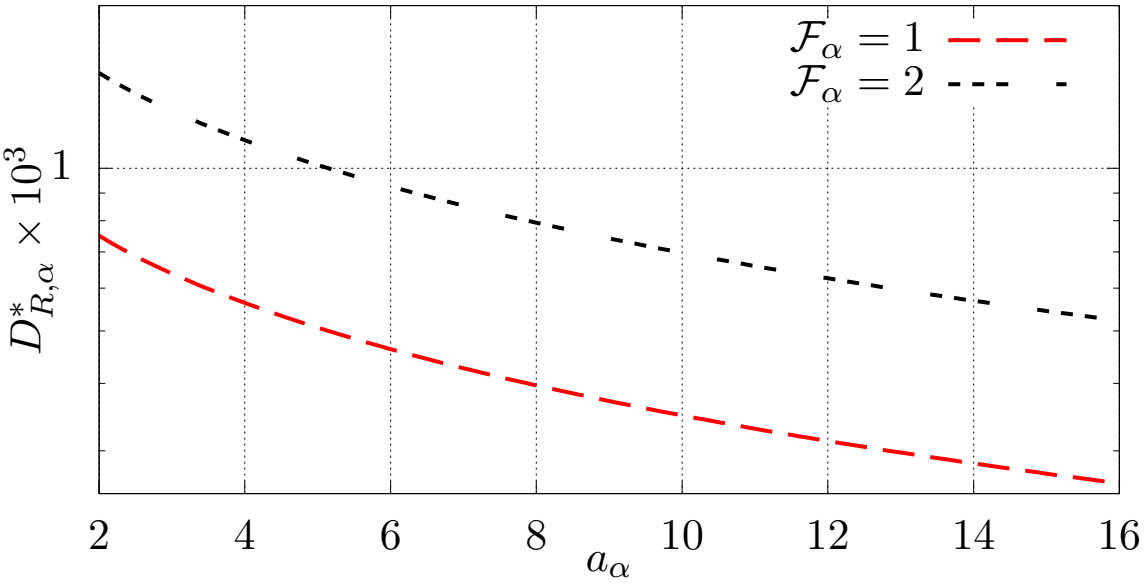

Figure 2.4: Behaviour of rotational diffusion coefficient provided for $\mathcal{F}_\alpha = 1, 2$.

2.2.2 Models of active rods and their interaction

Originally, active rods were introduced in the paper by Peruani *et al* [126]. They were represented as $2D$ polygons (see Fig. 2.5, (c)) and interaction was calculated by measuring the overlap between any two rectangles, i.e., 'soft' volume exclusion.

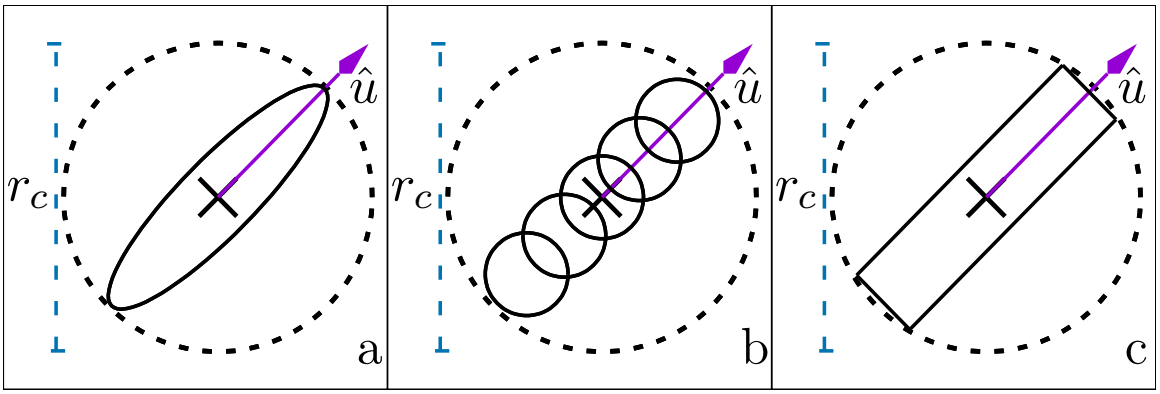

Figure 2.5: Different discrete-element models of active rod-like particles.
a) elliptic model; b) stack of segments; c) rectangle; Solid vectors represent orientations $\hat{\boldsymbol{u}}_\alpha$. Centres of mass are marked with solid crosses. Effective distance of interaction r_c is given by the dashed line. Note, that for rectangles r_c doesn't coincide with the length.

Other models that are widely used include rods consisting of segments or ellipses

[55, 127]. I employ the first type of simulation whereby rods are represented as a series of n_α segments — i.e., disks of diameter[2] d — stacked along the long axis of the rod (see Fig. 2.6 for a detailed diagram of the model). Both the distance between neighbouring segments l^0_α and n_α allow one to change the aspect ratio a_α. I also use linear density defined by Eq. 2.9 (first introduced by Wensink and Löwen [55]) of segments Λ as a global parameter in systems of segmented rods. I set it to a constant that is in fact a number of segments per unit length. This approach allows me to have rods of different length while maintaining a constant density of segments per rod length — this point means that all rods interact via *roughly* the same effective potential.

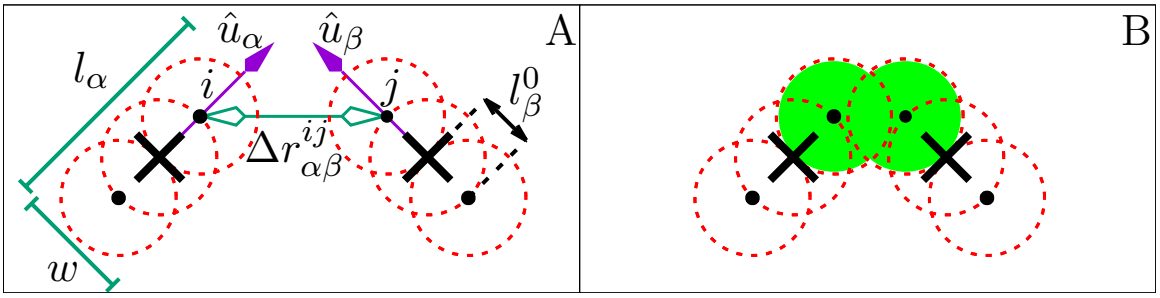

Figure 2.6: The diagram showing a) the general interaction scheme, b) two interaction rods of the same size, overlapped segments are marked (shaded) with green. Red dashed circles represent rod segments, their centres are marked with black dots. Black crosses denote centres of mass of rods.

Thus, assuming that l_α and Λ are given, the number of segments in an active rod can be calculated using the following formula:

$$n_\alpha = \lfloor \Lambda l_\alpha \rfloor, \tag{2.9}$$

where $\lfloor \cdot \rfloor$ denotes an integer part of a number. Now, the resulting force between two rods α and β is not zero when the distance $\Delta r^{i,j}_{\alpha,\beta} \leq d$ for any segment i of particle α and for any segment j of particle β. A representative example of such model is given

[2]Since all segments lie on the same rod axis the diameter of every segment d and the width of every rod w are essentially the same quantity. However, for the sake of clarity I consider them as two independent variables throughout the text.

in Fig. 2.6. Here, I depict two rods comprised of 3 segments each. Part A of Fig. 2.6 shows two particles before interaction. Part B shows the same rods interacting. Here, two top segments overlap resulting in repulsive force that pushes particles apart and results in a torque that realigns the rods.

There is an alternative model, where rods are assumed to have elliptic shape, the interaction is of Kihara-type [132] that depends on the minimal distance between two finite line segments (see, for example, [127]).

It is also possible to use both representations simultaneously. In such case all pairwise interactions are calculated using a segmented model, however, when a particle interacts with its medium fluid it is modelled as an ellipse (see, for example, Ref. [34]).

There is also a difference between simulations of soft matter and simulations of elementary particles. In both cases centres of mass are represented by points and any interaction has to be calculated between them. However, elementary particles are small comparing to the distance of interaction as opposed to soft matter where the distance of interaction coincides with the size of particles.

There is a variety of potentials that are used to simulate repulsive or repulsive-attractive interactions. I discuss some of them that are widely used (see, for instance, [1, 32]) and provide a figure (see Fig. 2.7) with a comparison of the most widely used potentials. However, for simulations in this thesis I use only the Hookean potential. In all discussed cases (see Sec. 2.2.2) I use a modified version of hardness κ — $\kappa^{i,j}_{\alpha,\beta}$, — assuming that: a) every rod can have its own κ_α, thus, it interacts with other particles through some effective potential (like in Ref. [1]); b) segments comprising a rod can have different hardness and, therefore, different effective size. For example, Kaiser *et al.* [117] employed this technique to break axial symmetry of active rods. Nevertheless, in my simulations I consider active rods that have homogeneous structure.

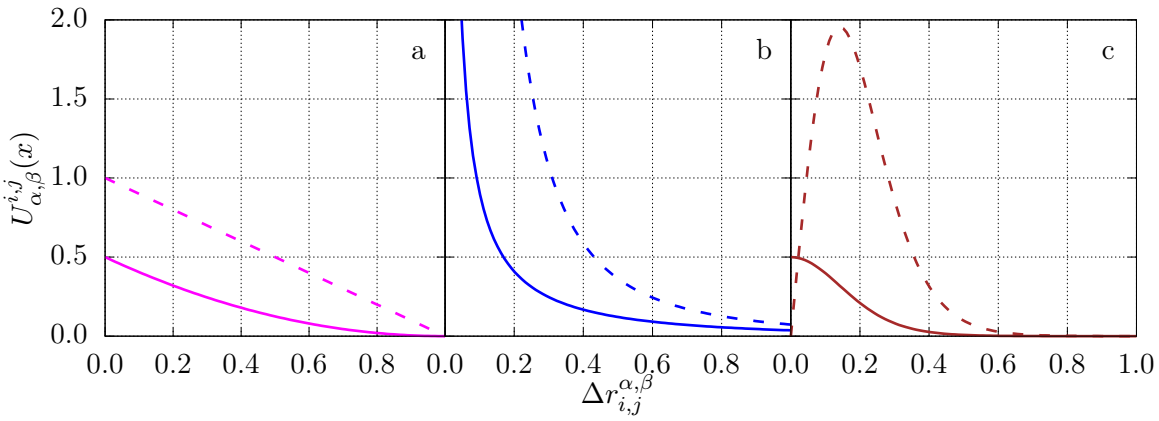

Figure 2.7: Comparison of potentials provided for $\kappa^{i,j}_{\alpha,\beta} \equiv 1$. a) Hookean potential; b) Yukawa potential; c) Lennard-Jones potential. All parameters of Lennard-Jones potential are chosen so that it is bounded ($E = 0.5$ in particular). The number of segments per rod is set to 10, this affects only the Yukawa potential since it's the only one that has explicit dependency on n. Solid lines denote potentials, dashed lines stand for corresponding forces.

First is the Yukawa potential from colloidal soft matter which is used to simulate interactions between charged colloidal particles as in Ref. [133]. For two segments i and j of rods α and β, respectively, I have:

$$ {}^{Y}U^{i,j}_{\alpha,\beta} = \frac{\kappa^{i,j}_{\alpha,\beta}}{n^2} \frac{\exp[-\Delta r^{i,j}_{\alpha,\beta}/d]}{\Delta r^{i,j}_{\alpha,\beta}}. \tag{2.10} $$

Here, all rods are assumed to have the same length so that $n_\alpha = n_\beta = n$.

Second is another well-known potential — Lennard-Jones (LJ). Again, the interaction of two segmented rods is described by the following (separation-shifted, see, for instance, Ref. [134] for additional details) potential:

$$ {}^{LJ}U^{i,j}_{\alpha,\beta} = 4\epsilon[\frac{1}{(b^2 + (\Delta r^{i,j}_{\alpha,\beta})^2)^6} - \frac{1}{(b^2 + (\Delta r^{i,j}_{\alpha,\beta})^2)^3}] + U_0, \tag{2.11} $$

where U_0 is a potential shift assuring that I do not have a discontinuity at $\Delta r^{i,j}_{\alpha,\beta} = d$. The interaction energy $\epsilon = b^{12}E/(b^{12} - 4b^6 + 4)$, where $E = {}^{LJ}U^{i,j}_{\alpha,\beta}(0) - {}^{LJ}U^{i,j}_{\alpha,\beta}(d)$ is the energy of interaction of two completely overlapping segments serving as a control parameter. The capping parameter $b = \sqrt{2^{1/3} - d^2}$ allows switching between

the divergent and non-divergent functions. When $b \neq 0$ ${}^{LJ}U^{i,j}_{\alpha,\beta}$ does not diverge at $\Delta r^{i,j}_{\alpha,\beta} = 0$ making the complete overlap of segments possible. The other case leads to a truncated version of the Lennard-Jones potential. This function is used because: a) it can be switched between two regimes where one allows complete overlap between two segments and the other one doesn't; b) it has lower computational cost comparing to, say, exponent (see Ref. [135]).

Finally, the last one is a spring-like (Hookean) potential. Since it has only two control parameters and has a low computational cost I use it in all my simulations:

$$ {}^{H}U^{i,j}_{\alpha,\beta} = \frac{1}{2}\kappa^{i,j}_{\alpha,\beta}(d - \Delta r^{i,j}_{\alpha,\beta})^2. \tag{2.12} $$

This comparison gives an insight on what can happen in active matter systems. In summary, both Hookean and LJ potentials allow complete overlap of two particles due to finite energies at zero distances as opposed to the Yukawa potential. However, the LJ potential can be switched between two regimes — one that allows complete overlaps and the other one doesn't — by tuning its parameters. Moreover, its gradient changes non-monotonically with distance in contrast to other two potentials. I also mentioned that all three potentials have different computational complexities which can be important in simulations of systems with large number of particles.

2.3 Numerical approach

In this section I discuss some potential difficulties that might arise in simulations of soft matter systems. That includes the performance of some numerical algorithms and simulations of systems with 'solid' boundaries. Next, I discuss the numerical scheme employed in the simulations and provide arguments to justify its usage. Finally, I introduce a generalized version of the numerical scheme that can be used in systems with arbitrary boundary conditions.

2.3.1 Boundary conditions

In this subsection I discuss various types of boundary conditions that are used in active matter systems. I provide the most widely used types such as periodic boundary conditions, external potentials, walls made of discrete elements and the method of images.

I start with periodic boundary conditions (see Fig. 2.8 for a schematic diagram). I assume that the domain has rectangular shape and its left bottom corner is placed at the point with coordinates $(0, 0)$. When a particle leaves the domain, meaning that $x_\alpha < 0; x_\alpha \geq L_x$ or $y_\alpha < 0; y_\alpha \geq L_y$, its image enters the domain from the opposite direction (see Fig. 2.8) This method is widely used in molecular dynamics simulations as well as in simulations of active particles (see, for example, references [55, 135]). Such boundaries are useful for simulation of bulk phases, however, there exist finite-size effects [136, 137]. For example, global orientational order, that is observed in moderately small systems of active rods, at some point disappears in large systems with the same packing fraction of rods [138].

Next, I discuss various methods of simulation of hard boundaries, I am aware of two general approaches described below. First, one can represent a solid wall or any other suitable boundary as a set of particles fixed in space [139] (see Fig. 2.9, a). This approach is more flexible in terms of the simulated boundary shape, however, one has to be careful to choose the distance between boundary elements to prevent particles in the simulation from leaving the domain. Obviously, it is possible to make this distance sufficiently small, however, that increases the number of boundary particles belonging to the wall. That, in its turn, makes the method computationally expensive due to higher number of interactions between active and boundary particles. I discuss possible ways to avoid this limitation further in this section, see Subsec. 2.3.4. There is one more method of images (see, for example, references [34] and [140]) which is based on the following: when an (elongated) particle approaches the boundary line,

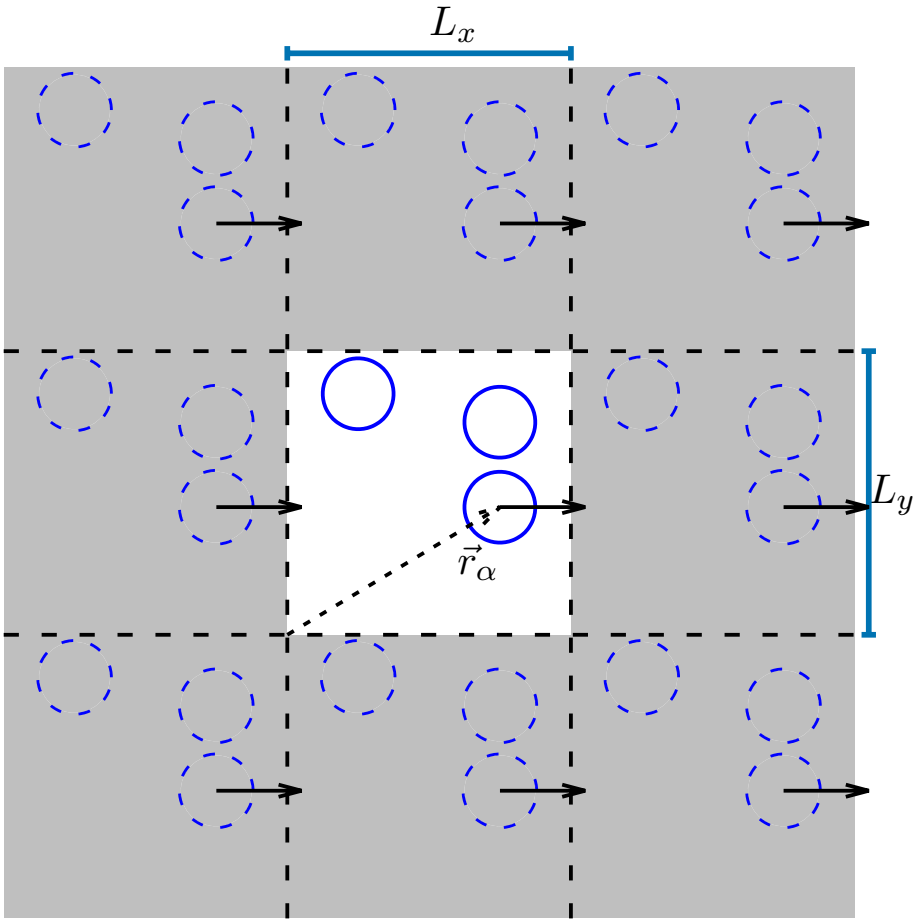

Figure 2.8: An example of two-dimensional square box with PBC in both x and y directions. Gray regions contain images of the initial domain (white square). Solid (blue) circles stand for particles, dashed (blue) — for their images. Solid (blue) lines denote the size of the initial domain. Particles leaving the domain or its images are marked with solid vectors. Dashed vector $\boldsymbol{r}_\alpha$ stands for the position (x_α, y_α) of particle α.

its image is placed on the other side of the wall. This method of simulating boundaries has some advantages since it has low computational cost and also allows simulations of flowing liquid *and* solid boundaries at the same time [140].

Second, one can use an external (it can also be time-dependent as described in Ref. [61]) potential of arbitrary nature as an additional term in the equations of motion (see Fig. 2.9, b).

Below I discuss a variety of potentials that can be used to confine active rods at walls. I start with a family of exponential potentials, first in this list is the Yukawa

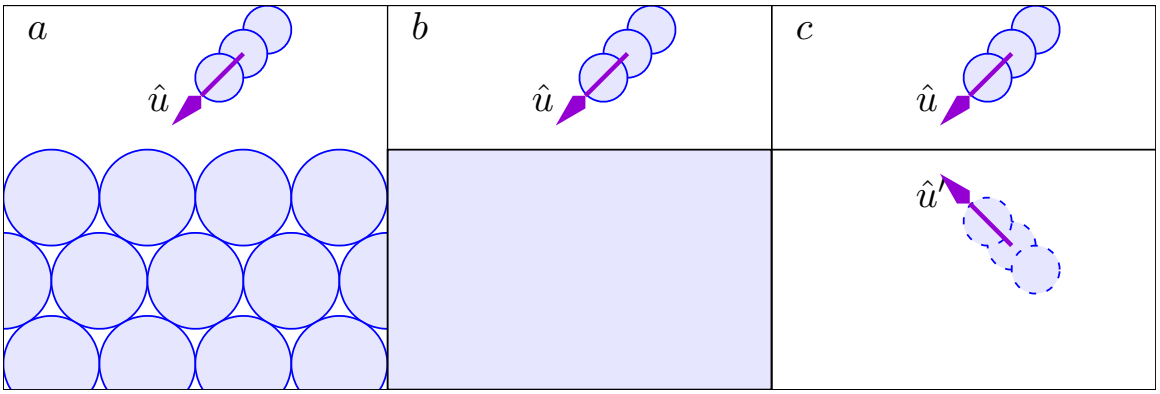

Figure 2.9: Schematic depiction of various boundaries. Solid ellipse represents an active particle. a) elements of the wall are given by disks; b) shaded area is unreachable by active particles due to high potential, its gradient is omitted to simplify the diagram; c) solid line stands for the border of the domain, it serves as the axis of mirror symmetry, dashed ellipse is the mirrored particle.

potential which is given by the following:

$$U(r) = \frac{U_0 \exp(-\kappa r)}{\kappa r},$$

where (assuming a homogeneous population) κ has the same meaning as in Sec. 2.2, r is the distance between a disk-segment and the wall, and U_0 is the magnitude of the potential [32]. Another option is to use $\mathrm{erf}(x)$ [141] or $\tanh(x)$ [1]. Whereas the first one (and its force) is unbounded as compared with the last two which are finite (as well as their forces), they have one thing in common — they all have exponential terms which make them computationally expensive. One possible way to avoid this is to use Lennard-Jones potential or its shifted and truncated version: the Weeks-Chandler-Andersen potential. Both of them can be computed (see Ref. [135] for reasonable arguments) easily — i.e., faster — comparing to the family of exponentials. I note that in all this cases every particle interacts with the boundary only once as opposed to the case with discrete boundaries (discussed earlier in this section). This means that the complexity of this method grows as $O(N)$ and can even be reduced to $O(1)$ in some cases which I discuss below in Sec. 2.3, again, see Subsec. 2.3.4.

2.3.2 Cell-linked list method

The cell-linked list (CLL) method was first introduced by by Allen and Tildesley in Ref. [135] as a way to significantly reduce the computational cost of simulations of particles with short range interactions. In a system with N particles each particle can potentially interact with $(N-1)$ neighbours resulting in $N(N-1)$ interactions, regardless of their nature and presence of any boundaries. Newton's 3$^{\text{rd}}$ law reduces this number to $N(N-1)/2$, nevertheless, the required computation still has $O(N^2)$ asymptotic behaviour. However, in systems with short-ranged interactions calculating pairwise distances between distant particles is wasteful since the resulting force between them is virtually zero.

Let's assume that such a population is confined within a $2D$ box of size $L_x = L_y = L$. In such cases [3] it is possible to split the domain into M strips of width L/M. Further splitting of every strip into M identical cells results in M^2 cells in total as presented in Fig. 2.10, left. Now, every one of them is a square of size $l_c = L/M$. The conventional approach first introduced by Allen and Tildesley [135] states that l_c has to satisfy one condition only — it has to be greater or equal than the effective cut-off distance r_c of the interaction potential.

In this thesis particles interact through direct collision meaning that for a system of identical disks the interaction distance r_c equals the diameter of a disk. From this statement it follows that a single particle can interact only with neighbours that are in the same or adjacent cells (see Fig. 2.10, left, black solid square). Assuming a homogeneous density throughout the domain every cell on average contains $N_c = N/M^2$ particles. That results — again, on average — in $\approx 3^2 N_c$ interactions per particle or, employing Newton's 3$^{\text{rd}}$ law again, can be reduced to $\approx 3^2 N_c/2$. That is a tremendous improvement compared to the naive approach. Now the number of

[3] Note that all conclusions can be extended to the case of three spatial dimensions.

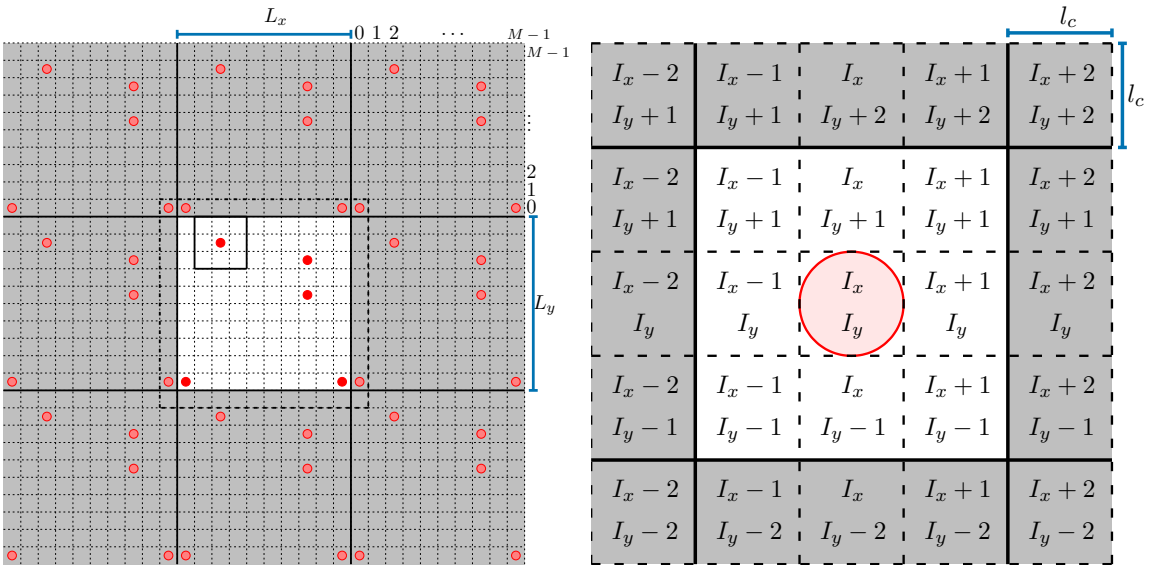

Figure 2.10: Left: An example of two-dimensional square box with PBC in both x and y directions. Gray regions contain images of the initial domain (white square). *Ghost* cells introduced in Ref. [2] lie between the central white square and the surrounding larger square marked with dashed lines. Central solid square denotes a cell with a particle inside and all neighbouring cells. Solid (blue) lines mark the domain dimensions, L_x and L_y. Right: a magnified region of the CLL grid. Solid (blue) lines denote the size of a single cell l_c. Red disk represents a particle, which size coincides with l_c. The cell that contains this particle is marked by a pair of indices I_x, I_y. Thus, all other cells can be uniquely identified by adding or subtracting a corresponding pair of offsets. This diagram can also serve as an example of index folding in the case of PBC. In this case the domain is marked with white cells. All indices that are congruent *modulo* 3 denote *exactly* the same cell, for example, $I_x - 1 \equiv I_x + 2 \bmod 3$.

computed pairwise interactions behaves like $O(N)$ which is significantly better than the initial asymptotic $O(N^2)$.

Here, I discuss issues that might arise in active matter systems with various boundary conditions (see, for instance, Subsec. 2.3.4.1).

First, I provide a basic algorithm to split the domain using the dimensions of the system [135]. Again, the system contains a population of of N (polydisperse) particles. Since I keep the width of all rods the same polydispersity implies a variety of lengths l_α of rods in the population. I use a uniform distribution $\mathcal{U}(s_{\min}, s_{\max})$ for the size of a rod. This distribution is set to be strictly positive to avoid non-physical particles of zero or negative size. Here, $s_{\min}$ and $s_{\max}$ are minimal and maximal sizes, respectively. In the case of monodisperse populations $s_{\min} = s_{\max} \equiv s$. The domain

is a square of size L as in Fig. 2.10, however, other shapes such as disks or rectangles are possible.

Next, I compute the size of a single cell l_c. As mentioned earlier in this subsection (see also Fig. 2.5, a, b & c), for the interaction distance r_c and the maximal possible particle size $s_{\max}$ holds the following identity:

$$r_c \equiv s_{\max}.$$

An estimate for the number of cells per domain side is given by this equation:

$$M' = L/r_c.$$

However, in general this equation gives a non-integer result which is not suitable for this particular problem. The solution here is to round down this estimate M' so that it becomes a positive integer $M \leq \lfloor M' \rfloor$. This particular choice of rounding also allows me to satisfy the condition between r_c and the cells size l_c:

$$l_c = L/M \geq r_c,$$

Now, any two particles in any two *non-adjacent* [4] cells are separated by a distance that is certainly greater than r_c and, thus, do not interact.

It is possible to identify a cell that contains a particle α with its centre-of-mass coordinates (x_α, y_α). In fact, the whole set of cells is a discrete coordinate system where I_x and I_y denote horizontal and vertical coordinates (indices) of a cell, respectively. Division of x_α and y_α by l_c and rounding the result down results in a pair of indices $I_x = \lfloor x_\alpha/l_c \rfloor$ and $I_y = \lfloor y_\alpha/l_c \rfloor$. Both indices lie in range $\overline{0, M-1}$, or, for a non-square domain, M is replaced with a pair M_x, M_y for x and y coordinates. Additionally, this method requires $I^{\min}_{x,y}$ and $I^{\max}_{x,y}$ as minimal and maximal indices of cells that are checked, respectively. For a system with PBC $I^{\min}_{x,y} = 0$ and $I^{\max}_{x,y} = M_{x,y} - 1$.

[4] By non-adjacent I understand cells that do not share sides or angles.

I show below that the ranges have to be modified when there is any external boundary present.

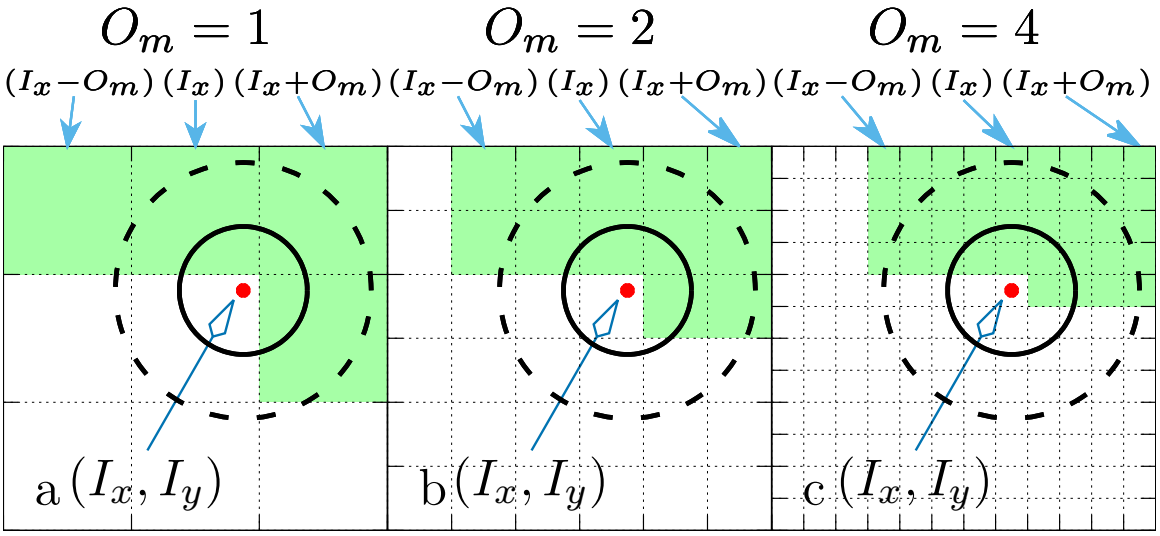

Figure 2.11: An example of 2D grids with various masks, red solid circle represents the centre of mass of a particle, black solid circle is a particle, black dashed circle is of radius r_c, shaded (green) cells have to be checked during the evaluation of the algorithm. All white cells have already been checked. In all cases empty-headed vectors point to the cell (I_x, I_y) containing the centre of mass of the particle, whereas solid vectors point to cells with indices $I_x - O_m$, I_x, $I_x + O_m$. a) $O_m = 1$; b) $O_m = 2$; c) $O_m = 4$, some cells that are checked stay outside r_c. The algorithm for this particular mask is provided below in the text. This given particle interacts with any other one whose centre of mass lies within the dashed circle.

I mentioned earlier this method requires checking not only the cell containing a given particle but also its neighbours. Here, I define the maximum offset number $O_m = \lceil r_c/l_c \rceil$ as the following: for a cell with indices I_x and I_y, all neighbouring cells have their absolute indices in ranges $I_x^n = \overline{I_x - O_m, I_x + O_m}$ and $I_y^n = \overline{I_y - O_m, I_y + O_m}$, respectively (see, for example, Fig. 2.11, (a)). For the conventional CLL method $O_m = 1$.

I also define a mask as a subset of neighbouring cells with the following properties: for any cell this is a subset of the neighbouring cells always containing a half of them. In addition, their relative indices have to stay the same for a given cell grid. For instance, in Fig. 2.11, a) those relative indices are $(-1, +1)$, $(0, +1)$, $(+1, +1)$ and

$(+1, 0)$. The choice of the mask has to satisfy only the condition that two cells with the opposite indices — i.e., $(I_x'^n, I_y'^n)$ and $(-I_x'^n, -I_y'^n)$ — can't belong to the same mask (see Ref. [135]). Folding of indices I_x^n and I_y^n is also required when toroidal topology of PBC is employed. Here, folding follows the rules of modular arithmetic. That means that, for example, for a cell with $I_x = 0$ adjacent cells to the left have their horizontal indices $I_x^n = -1 \equiv M_x - 1 (\mathrm{mod} M_x)$. Initially, for every cell all 8 of its adjacent — in the case of the conventional CLL method — neighbours are checked. Since the process is repeated for every cell, all distances are calculated twice. Thus, introducing a mask leads to half the number of neighbouring cells checked during the simulation, allowing to reduce the number of total calculations using Newton's 3^{rd} law.

Anisotropy of particles such as ellipses or rectangles (see Fig. 2.5 (a) and (c)) with two characteristic sizes — i.e., length and width — prevents direct usage of the conventional CLL approach. For example, any two elliptic particles of length a and width b can have their major axes of symmetry oriented along the same line. Here the minimal distance of potential interaction equals b. Changing the orientation so that now minor axes are parallel modifies the minimal distance of potential interaction so that it is equal to a now. Since there is no *a priori* knowledge about the orientations of particles, to ensure that all potential interactions have been taken into account, I have to consider the worst possible i.e., the latter case. That allows to capture all possible orientations of rods resulting in a circumcircle of diameter r_c that effectively describes a particle of a particular size (see Fig. 2.5). In this case r_c coincide with the largest dimension of a particle.

2.3.2.1 Ghost cells

It is important to briefly introduce another method to deal with unbounded domains since I use a similar approach in Subsec. 2.3.4.1.

A modified version of the conventional CLL with PBC that introduces *ghost* cells (see Ref. [2]) can be used (see Fig. 2.10, left). These are extra cells placed outside the domain and populated with images of real particles to simulate periodic boundary conditions.

In this case the domain is extended in all spatial directions so that there is an additional layer of width r_c surrounding the simulation box that is equivalent to an additional layer of cells in the case of the conventional CLL. Every iteration this extra space is populated with the images of particles that are within the distance r_c from the boundary *inside* the domain.

2.3.3 Adaptive grid

The CLL method is effective compared with the naive approach. However, even this method can be slow when it deals with a large number of particles in a system. There is a way to improve it even further, it does give an additional speed-up in some systems, nevertheless, even here there are advantages and disadvantages. I introduce it below, I also discuss its use with various geometric confinements.

First, I discuss the modification of the conventional CLL method first mentioned in Ref. [135]. As mentioned earlier, the conventional CLL method on a plane requires checking $(3^2 - 1)/2$ neighbouring cells. However, it is possible to decrease the size of a cell l_c increasing their total number instead. This can improve the performance, however, certain disadvantages exist even here [135, 142, 143].

The main idea is to improve performance of simulations by minimizing the number of so-called spurious interactions, I discuss it in detail below. Here, spurious interactions emerge when any two particles separated by a distance greater than the cut-off one resulting in zero repulsive forces by definition. The conventional CLL method requires the size of a cell l_c to be greater or equal to the cut-off distance of interaction r_c, resulting in 8 adjacent cells. This ensures that for *any* particle within a given

cell neighbouring cells completely cover its domain of interaction (see Fig. 2.11, A). The area within which all pairwise distances are calculated is $9l_c^2$ — that is the cell containing a particle and 8 its neighbours. The area within the cut-off distance of a single particle is πr_c^2. Assuming the most optimal case where $l_c = r_c$, the conventional approach results in about 65% of spurious interactions [5]:

$$1 - \pi r_c^2 / 9 l_c^2 = 1 - \pi/9 \approx 0.65.$$

Since the CLL method is based on tiling the particle's domain of interaction, it is possible to decrease the size of a box l_c, thus, having a better approximation of a disk of radius r_c. Dividing the cell size by two so that $l_c = r_c/2$ results in an increased number of neighbouring cells that have to be checked, since $O_m = \lceil r_c/l_c \rceil$. From that a condition also follows for minimization of the area that is covered with cells and outside the interaction distance r_c: the most optimal choice is when $r_c/l_c \in \mathbb{N}$. So, for $O_m = 2$ the total number of neighbouring cells completely covering the required area is 24. However, the total area of all $24 + 1$ cells is now $6.25 r_c^2$ leading to $\approx 50\%$ of forces being virtually zero. Further decreasing of the cell size l_c results in even better tiling results since now some cells are for sure outside the range of interaction (see Fig. 2.11, C). The algorithm 1 for a given cell in a system with PBC is provided below.

Nevertheless, this approach has its disadvantages first discussed in Ref. [2]. First, the total amount of memory that is used. Decreasing the size of a cell l_c by a factor of 2 quadruples the memory required to store the whole CLL structure as well as the time, required to clear it (see Fig. 2.12,h). I note here that all results are compared to the reference value, obtained from the system with $O_m = 1$, i.e., from the system with the conventional CLL implementation. This shows the relative performance cost

[5] This estimate is correct only for the case of monodisperse disks

Algorithm 1 This algorithm shows how all neighbouring cells belonging to the mask given in Fig. 2.11 are checked. Changing the mask results in different neighbours, however, the algorithm requires almost no modification after that. It also doesn't depend on O_m.

Require: $I_{x,y}$ ▷ Indices of a cell
  $i \Leftarrow 1$
  $j \Leftarrow 0$
  while $i \leq O_m$ **do**
    $I_x^n \Leftarrow (I_x + i)(\mathrm{mod} M_x)$ ▷ I assume PBC here
    $I_y^n \Leftarrow I_y$
    $CLL(I_x, I_y; I_x^n, I_y^n)$ ▷ Run regular CLL routine for cells $I_{x,y}$ and $I_{x,y}^n$
    $i \Leftarrow i + 1$
  end while
  $j \Leftarrow 1$
  while $j \leq O_m$ **do**
    $I_y^n \Leftarrow (I_y + j)(\mathrm{mod} M_y)$
    $i \Leftarrow -O_m$
    while $i \leq O_m$ **do**
      $I_x^n \Leftarrow (I_x + i)(\mathrm{mod} M_x)$
      $CLL(I_x, I_y; I_x^n, I_y^n)$
      $i \Leftarrow i + 1$
    end while$j \Leftarrow j + 1$
  end while

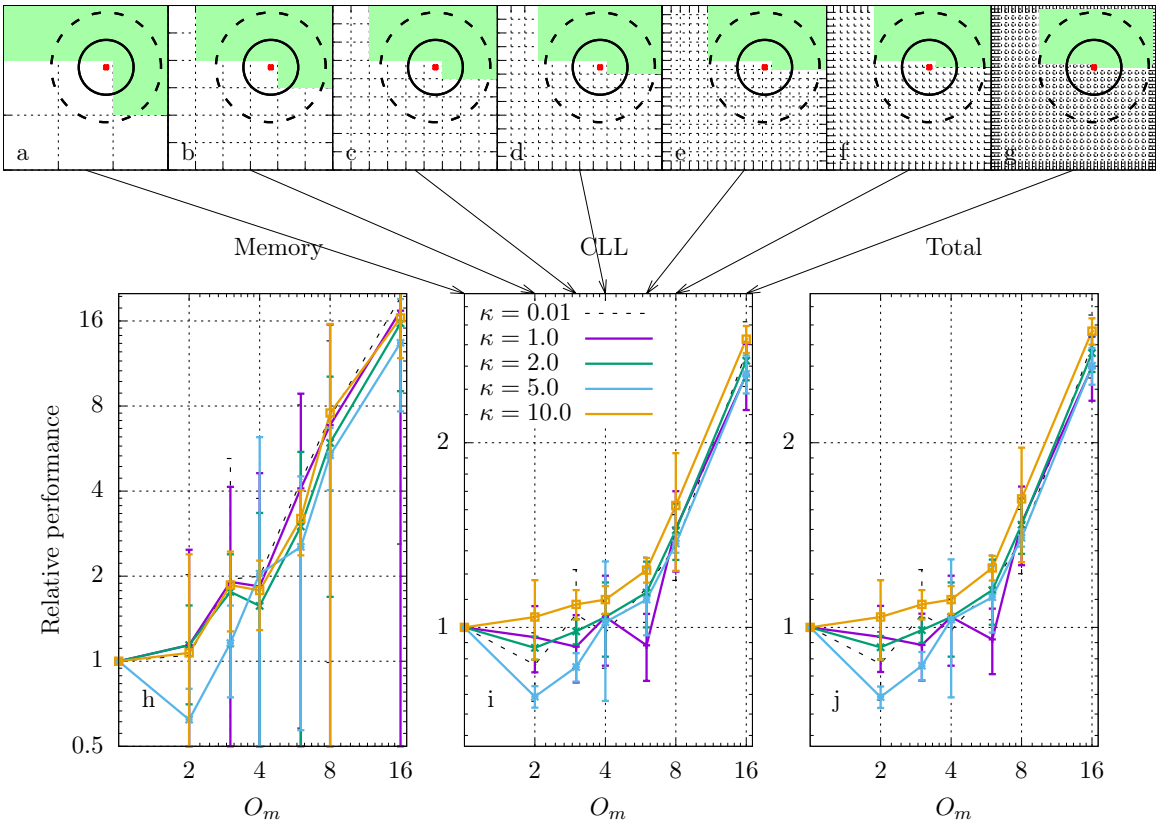

Figure 2.12: Benchmarks, measured in homogeneous dense systems with channel-like boundaries ($\log - \log$ scale). The total population in every simulation is ≈ 1000 3-segmented rods. All results are compared to the reference value, obtained from the system with $O_m = 1$ thus showing the relative performance cost (lower is better). That means that all values that are lower than 1 are better than the reference implementation. The value of softness parameter κ ranges from the ultra-soft case where $\kappa = 0.01$ to the hard case with $\kappa = 10.0$. Data is collected over 2.5×10^6 iterations. a-g) From left to right, corresponding masks for different values of $O_m = (1, 2, 3, 4, 6, 8, 16)$; h) clearing and re-populating the CLL structure; i) looping through all CLL cells; j) a sum of two metrics. Arrow point from the masks to the corresponding values of O_m.

(lower is better). That means that all values that are lower than 1 are better than the reference implementation.

Whereas the method itself still has linear asymptotic behaviour $O(N)$, where N is the total number of particles, constant factors such as O_m that are usually ignored in such cases start playing a significant role. Thus, the resulting asymptote looks like $O(O_m^2 N)$ giving a more accurate estimate. That means that any further change of the cell size l_c results in the same quadratic dependency. Therefore, at some point even the simplest procedure of memory clearing starts having an intolerable overhead. Second,

there is additional overhead associated with determining whether a cell is occupied. There is a point when checking all empty cells starts requiring more time than has been saved by reducing l_c (see Fig. 2.12, i & j). One more idea was to vary values of the softness coefficient κ while keeping other parameters constant and see how it might affect the performance. I based this assumption on the following observation: when the system has had time to evolve, various values of κ (or alternatively $\mathcal{F}$) produce a variety of configurations of active rods with distinct density distributions, resulting in different numbers of interactions i.e., collisions, per particle. The data given in Fig 2.12, i) prove this point.

The discretization time step $\Delta\tau = 0.002$ is also adapted from Ref. [55] with an assumption that there is no density dependency here. That is to keep measurements in systems with different populations consistent and also to simplify the simulations. Further decreasing of the time step doesn't change the results so, no additional checks regarding the numerical scheme's accuracy and stability has been made as it is sufficient enough for such simulations (see Ref. [55] and references therein).

I note that provided results are for illustrative purposes only. Nevertheless, the conclusion is that: a) this modification of the conventional CLL method can be employed in various simulations to speed up calculations; b) it has a limited range of used parameters, any significant decrease of l_c leads to intolerable overheads, thus the size of a cell l_c has to be at most 2-3 times smaller than the distance of interaction r_c; c) such parameters as, for example, κ can also affect the execution time. Points b) and c) clearly show that one needs to calibrate CLL parameters carefully before running any serious large scale simulations i.e., in my case it starts around 10^5 rods.

The obtained results coincide with early predictions from Ref. [2]. First, as expected, the time required to clear the CLL structure grows *roughly* quadratically. Whereas the standard deviation is high, it can be explained by unstable computing environment used for benchmarking i.e., it was a shared cluster. Second, average time

required for checking all cells and calculating the forces decreases (see, for instance, 2.12, i, blue line) when the value of O_m gets greater than one. Moreover, it does depend noticeably on the value of κ (compare blue and yellow lines given in Fig 2.12, i). That means for each κ and possibly for other static parameters there is an optimal value of O_m resulting in better performance. Nevertheless, further growth of O_m makes all the benefits of this method disappear. Thus, after careful considerations I picked $O_m = 2$ for all my simulations.

From that I can conclude the following. For any system there exists an optimal value O_m – in my case $O_m = 2$ – that may vary depending on the hardware and particular code implementation [2]. However, it may also depend on the parameters of the simulated system. For example, I simulate non-equilibrium active systems where local density can fluctuate significantly. That may result in a different average number of interactions per particle leading to a longer execution time of the simulation. The difference in performance is especially noticeable in systems with soft interactions. I presume here that this dependence on κ is a feature of confined systems, however, a proper case study of systems with different boundary conditions (including PBC) is beyond the scope of this thesis.

2.3.4 CLL method with arbitrary boundary conditions

A variety of different boundaries can be used to simulate active system such as bacteria or other microscopic active particles in microchannels or microscopic droplets. It is possible to simulate small systems with $\approx 10^2$ active agents and any boundary without involving serious optimization (e.g. CLL method or parallel computing). However, increasing the number of particles by an order of magnitude leads to significantly longer execution times. Moreover, active matter simulations sometimes involve up to $10^5 - 10^6$ particles meaning that more sophisticated programming techniques are needed.

In this subsection I introduce a new construct in discrete element methods — *shadow* cells. They are essentially extra cells of the same size that are *always* outside the domain boundary (see Fig. 2.13). I also provide a simplistic algorithm that allows the following: a) a variety of the boundary shapes can be used without any changes of the code, however, the performance of such simulations can be sub-optimal; b) the time required to calculate all particle-to-boundary interactions is significantly reduced compared to the conventional implementation.

I start with a $2D$ system populated with (active) particles. In addition, extra boundary conditions of an arbitrary nature are imposed, making the system completely closed (disk-like chambers as in Fig. 2.13, b) or semi-closed [6] (see Fig. 2.13, a). The results of simulations of the latter case and their in-depth analysis are presented in Ch. 3. Additionally, Ch. 4 contains a detailed analysis of some statistical properties of such systems.

2.3.4.1 *Shadow* cells

Next step is to define a new object — *shadow* cells. They are extra cells (a layer or more when $O_m \neq 1$) that are always outside the domain similar to the *ghost* cells. but always empty as opposed to the *ghost* cells discussed in Sec. 2.3.2. They are used to avoid indexing problem after introducing a new boundary. I provide a thorough explanation in the text right below.

I start with the simplest case of a $2D$ domain with PBC. The domain is split so that now there is a CLL grid of some suitable size $M_x \times M_y$ such that $O_m = n'$. The algorithm checks all cells and their corresponding neighbours in range from 1 to M_x and from 1 to M_y, one by one. Since all cells are identical, this task becomes a trivial problem. Now, I introduce the simplest case of boundaries i.e., straight walls of some nature, so that any particle inside the domain can't move from cells with

[6] Note, that confining particle motion in one direction automatically requires that minimum image convention [135] in the same direction doesn't hold. Folding of indices in the same direction is also not required.

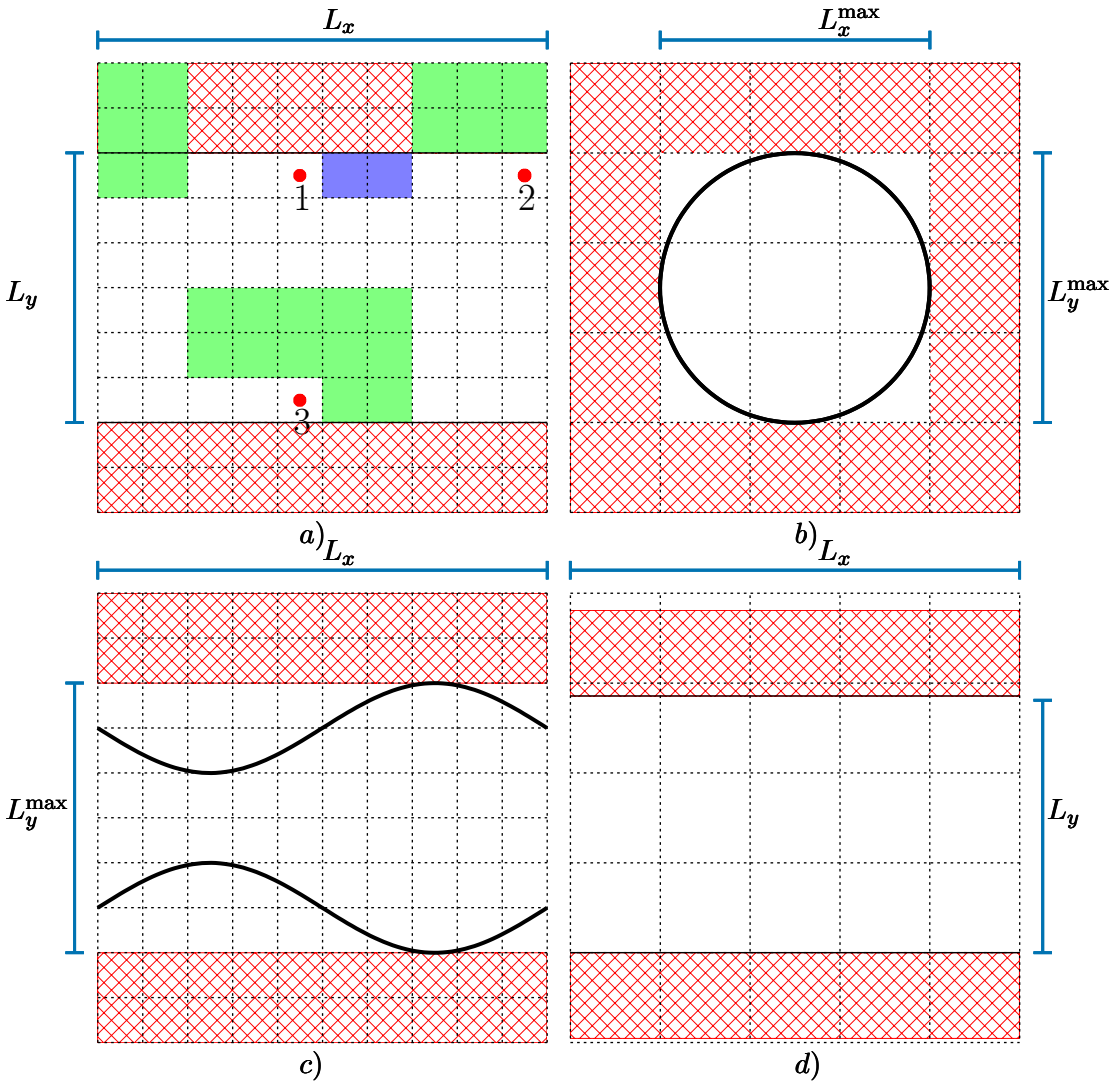

Figure 2.13: Examples of domains with different boundaries. *Shadow* cells are marked with (red) crossed regions. Left column shows domains where $O_m = 2$, whereas right gives examples of systems with $O_m = 1$. Walls are represented by solid (black) lines. Particles $(1, 2, 3)$ are marked with red dots, solid cells surrounding them belong to corresponding masks. Here, green colour stand for the conventional mask (particles 2 & 3) whereas blue colour (particle 1) is used to mark the mask for cells adjacent to the walls. Solid (blue) intervals stand for the sizes of every system $L_{x,y}$, where superscript max means that the size varies.
a) two-dimensional square box with PBC in x direction and external potential in y direction;
b) two-dimensional square box with a disk-like domain inside;
c) a periodic channel with sin-like walls;
d) the case of a periodic channel where cells actually cover some area not accessible by particles.

indices $I_x = M_x$ to cells with indices $I_x = 1$ and vice versa. Essentially, there is no more PBC in y direction as well as no index folding in the same direction. In this case all cells are classed as internal or adjacent to the walls. The former have their indices $n' < I_x < M_x - n'$, the latter are the remaining cells. Whereas all internal elements of the CLL grid are treated in the same way as in the case of the conventional CLL method, there is no conventional way to deal with the boundary cells. The problem here is that for a given cell there might be neighbours which indices are outside the given range $\overline{1, M_x}$ and, since there is no index folding in this direction, such neighbours are essentially not defined. There exists a straightforward solution to this problem: one can treat boundary cells separately and use a different mask. An example of such a solution is provided in Fig. 2.13, a). However, this solution despite being correct, has two potential issues. One is that the number of masks depends on the value of n' and on the shape of the boundary. The other is that changing the shape of the boundary might result in different masks leading to incorrect results.

I suggest another way to treat the CLL cells that are close to the confining walls. First, there is no need to have any *a priori* knowledge about the particular shape of the boundaries. The only information required is the size of the confinement, it has to be $L_x^{\max}$ and $L_y^{\max}$ i.e., maximal length and width (see, for example, Fig. 2.13, c), and the direction of restricted motion such as x or y. It is easy to notice that the whole domain is enclosed within a rectangle of size $L_x^{\max} \times L_y^{\max}$. Now I assume that this rectangle can be split into square cells of some suitable size l_c with the corresponding offset $O_m = n'$. I also introduce 4 auxiliary parameters $n_x^+, n_x^-, n_y^+, n_y^-$ that can characterize a given mask. For a cell with indices I_x, I_y and all its neighbours I_x^n, I_y^n covered by the mask the parameters are defined as the following:

$$
\begin{aligned}
n_x^+ &= |\max_{n\in\overline{1,O_m}}(I_x - I_x^n)|,\\
n_x^- &= |\min_{n\in\overline{1,O_m}}(I_x - I_x^n)|,\\
n_y^+ &= |\max_{n\in\overline{1,O_m}}(I_y - I_y^n)|,\\
n_y^- &= |\min_{n\in\overline{1,O_m}}(I_y - I_y^n)|.
\end{aligned}
$$

For example, for the mask provided in Fig. 2.11, a) the parameters take the following values: $n_x^+ = 1, n_x^- = 1, n_y^+ = 1, n_y^- = 0$.

Next step is to expand the CLL grid in the corresponding direction or directions by adding $n_{x,y}^{+,-}$ extra layers of *shadow* cells. I note that the parameters of the domain stay the same, the only thing that has changed is the number of CLL cells. A few examples of such expanded grids are provided in Fig. 2.13. The CLL algorithm discussed earlier in this chapter is slightly changed as well. The initial size of the CLL grid was $M_x \times M_y$, now, if there is no PBC in x, y directions $M_{x,y} = M_{x,y} + n_{x,y}^+ + n_{x,y}^-$. This change also implies — again, with the same idea about PBC in mind — that there is a shift of $I^{\min}$ and $I^{\max}$ so that $I_{x,y}^{\min} = n_{x,y}^-$ and $I_{x,y}^{\max} = M_{x,y} + n_{x,y}^- - 1$. This means that during simulations the CLL algorithm loops through the internal cells only (see Alg. 2), everything that is outside $\overline{I^{\min}, I^{\max}}$ range is by definition a *shadow* cell.

This approach allows to employ a variety of confinements without modifying the source code, however, it comes at the cost of minor performance degradation. It is caused by checking the *shadow* cells that are always empty.

2.3.4.2 Domain tiling

The choice of l_c in the case of rectangular domains is a bit more complex comparing to regular square-shaped domains. Here, I provide a detailed explanation starting with a rectangular domain with PBC.

Algorithm 2
Cell-linked list algorithm for a system with arbitrary non-periodic boundaries.

Require: $M_{x,y}, n^-_{x,y}, n^+_{x,y}$ ▷ CLL grid size, mask parameters
Require: $I^{\min}_{x,y} \Leftarrow 0; I^{\max}_{x,y} \Leftarrow M_{x,y} - 1$ ▷ Limits of indices
Ensure: $I^{\min}_{x,y} \leq I_{x,y} \leq I^{\max}_{x,y}$ ▷ Indices of a cell are restricted
Ensure: $0 \leq I^n_{x,y} \leq M_{x,y} + n^-_{x,y} + n^+_{x,y} - 1$ ▷ Indices of neighbouring cells are in range

```
if !PBC_{x,y} then
    I^min_{x,y} ⇐ n^-_{x,y}
    I^max_{x,y} ⇐ M_{x,y} + n^+_{x,y} − 1
end if
I_{x,y} ⇐ I^min_{x,y}
while I_x < I^max_x do
    while I_y < I^max_y do
        CLL                                   ▷ Run regular CLL routine
        I_y ⇐ I_y + 1
    end while
    I_x ⇐ I_x + 1
end while
```

For a given rectangle it can be perfectly covered with identical squares iff the ratio of its sizes is a rational number. This means that the total number of domains available for simulations in coupling with the CLL method is infinite, but countable. That is comparing to an infinite uncountable set of all possible rectangles. It's not like it makes a noticeable difference, nevertheless, picking a domain for such simulations can't be arbitrary.

At the same time, having extra boundaries imposed actually makes this problem easier. I elaborate this point right below. For now, I use a simple case of a rectangular domain of size $L_x \times L_y$. It is periodic in x direction, whereas the motion of particles is restricted in y direction. Some particles of effective size r_c populate this domain. Application of the CLL method gives the cell size $l_c = r_c$. First, I consider the case when $L_y/l_c \in \mathbb{N}$ and $L_x/l_c \notin \mathbb{N}$ so that,

$$L_y/l_c = M_y,$$

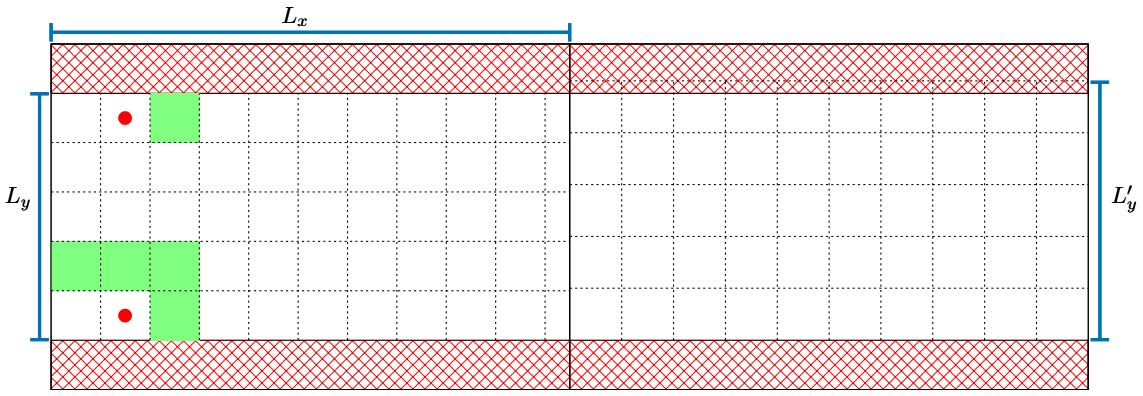

Figure 2.14: An example of the cell resizing procedure. Red crossed regions represent areas behind the walls. Red solid dots stand for particles, green solid cells are corresponding masked neighbours. Here the conventional approach requires two different masks. In this particular case $L_x = 10.5, L_y = 5, l_c = 1$. Left part of the figure is the initial domain and its tiling, right — the same domain with a resized grid. After resizing $l'_c = 1.05$, it is easy to notice that now top row of cells occupies part of area that initially doesn't belong to the domain and is not accessible for particles. However, for computational purposes it's irrelevant.

and

$$\lfloor L_x/l_c \rfloor = M_x \in \mathbb{N}. \tag{2.13}$$

The solution to the problem of non-integer number of cells is to increase the size of a single cell so that

$$l_c \to l'_c = l_c + \Delta l : L_x/l'_c = M_x. \tag{2.14}$$

However, that automatically means that,

$$M_y > L_y/l'_c \notin \mathbb{N}. \tag{2.15}$$

It can be easily resolved by stretching the domain in y direction to make it fit an integer number of cells M'_y. Since all area beyond the walls is *virtually* inaccessible by particles, the emerging behaviour is not affected by this procedure. Now I need to introduce an estimate for M'_y. The size of a cell has been increased so that $l'_c = l_c + \Delta l$,

the additional term Δl can be extracted from Eq. 2.13 and Eq. 2.14:

$$\Delta l = \frac{L_x - \lfloor L_x/l_c \rfloor l_c}{\lfloor L_x/l_c \rfloor}. \tag{2.16}$$

It is easy to notice that L_y can fit a certain number of cells of new size l'_c and still has some extra space left. Systems, where $L_y/l'_c \in \mathbb{N}$ are also possible (consider, for example, the case when $L_x = 10.5$, $L_y = 21.0$, $l_c = 1.0$) but these are the exception rather than the rule.

Here, to estimate the number of cells M'_y I use two auxiliary inequalities for rounding of real numbers:

$$\begin{cases} \forall a : \{a > 0, a \notin \mathbb{N} | a < \lfloor a \rfloor + 1 = \lceil a \rceil\}, \\ \forall a : \{a \in \mathbb{N} | \lfloor a \rfloor + 1 > \lceil a \rceil = \lfloor a \rfloor = a\}. \end{cases} \tag{2.17}$$

This means that the correct way to treat this *potential* extra space in Eq. 2.18 is to round up. I put Eq. 2.13, 2.14 and 2.15 together:

$$M_y > \frac{L_y}{l'_c} = \frac{L_y}{l_c + \Delta l} = \frac{L_y \lfloor L_x/l_c \rfloor}{L_x}.$$

Now I need to find a corresponding M'_y using the auxiliary inequalities 2.17 provided above:

$$M'_y = \lceil \frac{L_y \lfloor L_x/l_c \rfloor}{L_x} \rceil. \tag{2.18}$$

The other case of domain tiling is when $L_y/l_c \notin \mathbb{N}$ and $L_x/l_c \in \mathbb{N}$. It simply reduces to the previous case by expanding the domain in y direction. Since $L_x/l_c \in \mathbb{N}$, $\lfloor L_x/l_c \rfloor = L_x/l_c$, Eq. 2.18 becomes trivial,

$$M'_y = \lceil L_y/l_c \rceil.$$

The scheme of tiling here becomes the same as in Fig. 2.14, right.

2.3.5 Boundary tiling

Earlier in this chapter (see Subsec. 2.3.1) I introduced various types of boundaries used in discrete element methods and in simulations of active matter in particular. Here I present a simple way to reduce the cost of particle-to-wall interactions regardless of the boundary type and its particular implementation — i.e., external potential, particles fixed in space or the method of images.

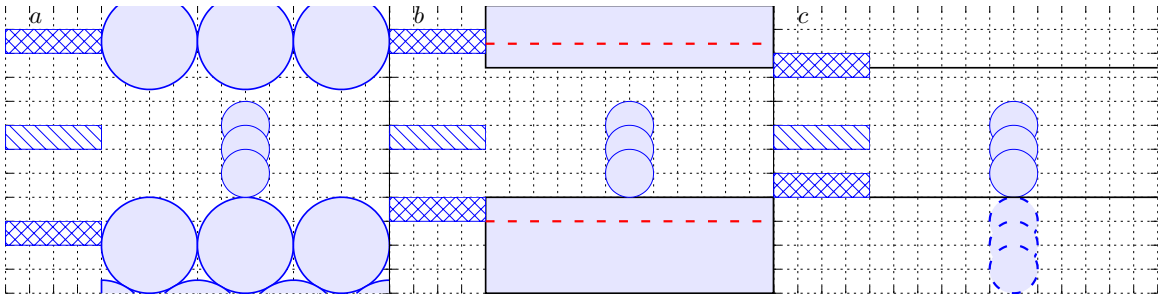

Figure 2.15: Examples of various boundaries: a) segmented wall; b) 'solid' wall, red dashed lines denote the effective borders of the domain that are discussed in this section; c) method of images. Solid disks — segments of a real particle, dashed disks — segments of a virtual particle. Crossed rectangles mark rows of CLL cells containing: a) centres of the innermost layer of wall segments; b) the effective borders of 'solid' walls; c) the borders of the domain. Lined rectangles mark rows of CLL cells containing the centre of mass of a test real particle.

Again, N (active) particles move across the domain. To keep this chapter consistent the domain is chosen to be a periodic channel. A generalization for other confinements is also possible albeit a more mathematically sophisticated one. I also consider same ways to implement a walls as I discussed earlier. All of them are given in Fig. 2.15.

2.3.5.1 Walls made of particles

Here, every boundary is represented by a collection of hard disks that have positions fixed in space. Regular (active) particles within the domain interact with such walls through a repulsive potential. Compared to other two methods discussed here this one is the most advantageous in terms of possible configurations of walls, since it allows to create a greater variety of shapes, regular or not.

However, this is not the most efficient way to imitate a solid wall. First, the number of obstacles making the boundary can be quite high (see, for example, Fig. 2.15, a). Assuming that the conventional method i.e., checking *all* pairwise distances, is used to calculate forces between particles, the total number of interactions between active rods and wall segments grows like $O(N_w N)$, where N_w is the number of particles comprising the wall. Second, the surface itself is highly irregular resulting in spurious friction. I note, however, that such surfaces are possible in real life. Such structure might also lead to the situation when an active particle is trapped between the innermost wall segments or slips even further into the wall. Last two problems can be avoided by increasing the size of the wall elements so that they partially overlap. It is also possible to increase their hardness κ to make the whole boundary harder.

Here, I treat boundary segments as part of the simulation, resulting in an exotic mixture of active and passive particles. In this case the conventional CLL method can be used, however, some parameters like, for example, the domain size have to be changed. Nevertheless, I talk only about the way to decrease the computational cost of wall-to particle interactions.

To keep the problem simple I assume that disk-like wall segments and active particles have the same effective size (see Fig. 2.15, a). The case of different sizes can be easily reduced to a simulation of a bidisperse mixture of active and passive particles. Whereas active rods interact with wall segments, the latter by definition have their positions fixed in space. The wall doesn't contribute to the dynamics of active particles when the distance between the centres of the innermost layer of boundary elements and the centre of an active rod are separated by the distance greater or equal than r_c. However, for the purpose of combining the described approach with the CLL method, it is better to talk in terms of CLL cell indices I.

As I mentioned above, the employed geometry here is a periodic channel. This means that wall elements form straight lines with the same y coordinate (see Fig.

2.15, a). Taking into the account only the innermost boundary layers and applying the method for finding cell indices described earlier in this chapter, I get I_y^w CLL indices for a given wall. Now, from Subsec. 2.3.3 it follows that two particles do not interact when their respective CLL cells are separated by more than O_m cells. That result in the following inequality:

$$|I_y^w - I_y| \geq O_m,$$

where I_y is the y index of a CLL cell. Of course, this is the most trivial case of a straight channel, however, a generalization for other shapes follows easily. This means that to calculate interactions with the boundaries the code needs to contain an additional loop for particles within a distance from the wall,

$$|I_y^w - I_y| < O_m.$$

This way only the particles that can potentially be affected by the walls are involved. The cell scaling procedure that is described in Sec. 2.3.4.2 doesn't affect this estimate since it is based on the indices and doesn't depend explicitly on the cell size. I note that this condition might be not enough in the case an active particle slips inside the boundary. However, I work under the assumption this never happens.

2.3.5.2 'Solid' walls

This way to simulate a wall (see Fig. 2.15, b) is more computationally effective comparing to the previous one. The force between the wall and a particle is calculated only once as opposed to the previous case where an active particle can interact with more than one wall segment. However, there is one serious disadvantage using this method. As mentioned earlier, such boundaries are based on functions which are quite expensive to calculate. It is harder to design arbitrary containers since this requires an appropriate analytical function to be derived.

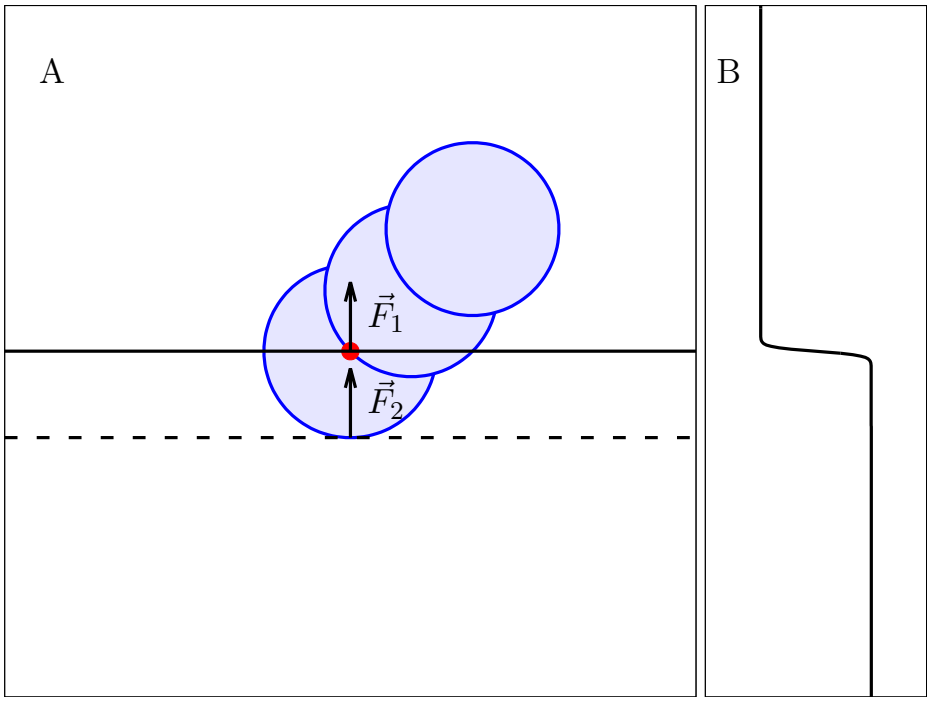

Figure 2.16: This diagram shows how a particle can actually 'penetrate' the wall. A) Solid line denotes the real boundary, dashed line denotes a virtual wall with the y coordinates w_y and w_y^e, respectively. $\boldsymbol{F}_1 \equiv \boldsymbol{F}_2$, however, $\boldsymbol{F}_1$ acts on the segment's centre of mass, marked by the red dot whereas $\boldsymbol{F}_2$ acts on the segment's surface. B) The form of the potential at this point.

In addition, this method has its own issues. First, since here the boundaries are essentially external force fields, they act on the centres of mass of particles or other points within them rather than interact through direct contact. That leads to particles 'penetrating' the wall as depicted in Fig. 2.16. That results in the effective size of the domain being greater than that of the initial one. This doesn't affect the dynamics of systems, the only variable that requires a correction is the total packing fraction of particles. Second, such boundaries are not perfectly 'solid'. In my simulations I used a sum of two hyperbolic tangents $tanh(x)$ to create a rectangular channel. I tuned the boundary parameters so that the resulting boundary started to look like the Heaviside function ($H(x) = 1 \forall x > 0, H(x) = 0 \forall x < 0$). The default tanh or any similar function might lead to non-zero boundary forces away from the wall itself. Zarif & Naji show in Ref. [144] that this leads to confinement induced collective behaviour even when particles are sufficiently far from the confining boundaries.

Anyway, under the assumption that the potential is 'sharp' enough I provide a simple criterion for a particle α in the vicinity of the wall:

$$\Delta r = |w_y^e - y_\alpha| < r_c/2,$$

where w_y^e is the effective y coordinate of the wall (see Fig. 2.15, b) and 2.16, dashed lines).

Assuming that the boundary belongs to a cell row with the y index I_y^w, it is possible to move from relative coordinates to relative CLL indices again. Dividing the distance Δr by the cell size l_c and applying the auxiliary inequalities 2.17 to the obtained fraction, I get:

$$|I_y^w - I_y| \leq \lceil \Delta r/l_c \rceil. \tag{2.19}$$

Only particles that are within the cells this close to the wall can actually interact with it.

2.3.5.3 Method of images

As before, I discuss possible issues and potential benefits of this method (see Fig. 2.15 , c) for a representative example). The problem here is — again — difficulty of realizing complex domain shapes, however, it has been shown by Lushi in Ref. [64] and by Wioland in Ref. [34] that it works well in disk- and channel-like confinements, respectively. The advantage of this method is that every real particle interacts with its own 'image' and this significantly reduces the number of calculations when compared to the case of segmented walls. Surprisingly, the criterion for this boundary implementation is similar to the one for the 'solid' wall that is given by Eq. 2.19. However, w_y^e here is replaced by the actual position w_y of the wall since there is no

'penetration':

$$|I_y^w - I_y| \leq \lceil |w_y - y_\alpha| / l_c \rceil. \tag{2.20}$$

2.3.5.4 Discussion

To sum up, it is possible to make some simulations less computationally expensive. Densely populated passive systems with some rare exceptions have their densities uniformly distributed over the domain whether or not there is a confinement in there. In the case of active systems the situation can differ as observations *in vitro* and *in silico* show. Active particles in confined systems tend to stay in the vicinity of the walls resulting in non-uniform density distribution. This means that regardless of other parameters of the simulation — i.e., κ — the computational cost of the method described above is proportional to the total population — $O(N)$, but only in the case of sparsely populated systems. The only type of walls that can actually get performance benefits here is the segmented wall. In the case of an active particle staying close enough to the confinement edge it only interacts with some close wall segments due to this method applied. Whereas the complexity is still proportional to the number of segments in the wall $O(N_w)$, one more factor appears — the total number of cells in a particular direction M. In the case of rectangular channels parallel to x the cost becomes proportional to $O(N_w/M_x)$. The complexity is still linear, however, it is reduced greatly by this factor, potentially saving a lot of computational time.

When the packing fraction grows such behaviour starts to bifurcate. One case is when almost all particles accumulate strongly near the walls. This can happen when self-propellant forces dominate over repulsive ones. In the case of *ultra-soft* and soft systems all or almost all active agents can be found close to the boundaries. Whereas the *ultra-soft* regime is unrealistic, at least in biological context, *hedgehog* formations are observable not only in soft systems [1] but also in systems with hard rods that

have high aspect ratios [32]. Unfortunately, that results in the same computational cost as described in the passage above.

On the contrary, when steric interactions are sufficiently strong in dense systems, the overall situation changes significantly. In such simulations the density around the walls is limited by some critical value, say, N' particles per single CLL cell. From this it is possible to make a conclusion. At some packing fraction the population of particles in the vicinity of the confinement saturates, they no longer can increase their numbers in that area. This leads to a *roughly* constant number of interactions with the wall, regardless of the total population N. In dense systems where the ratio of the domain perimeter to its area is low this method might be extremely applicable.

Summarizing the whole section, it is possible to further improve the performance of the conventional LLC algorithm, however, a proper calibration of the simulation parameters is required beforehand. *Shadow* cells allow one to modify the boundaries in a wide range without the actual source code modification, however, it comes at the cost of performance i.e., the code that is responsible for interactions between the boundaries and the particles is potentially sub-optimal. I also note that using the tiling approach for various boundaries that I provide above it is possible to improve the performance at no additional cost.

2.4 Conclusions

In this chapter I've provided a general approach to simulations of heterogeneous active matter. The method used here is based on discrete soft particles. Additionally, I provided a thorough explanation of the numerical scheme as well as its modifications.

I also introduced a new method for simulations of (active) particles in arbitrary confined domains based around the idea of *shadow* cells. It is computationally effective albeit having sub-optimal performance, however, it can be used to simulate a wide range of boundaries which is more beneficial in many studies. Nevertheless,

I note that this method might be unsuitable for large-scale simulations. My intent was to create an algorithm that allows easy and correct modifications of the domain boundaries, however, it may potentially result in sub-optimal performance. It can be easily adapted to any suitable problem like, for example, generating of domains for sorting of active particles. At the same time, simulations of millions of particles might require heavy optimization for a given system while loosing some flexibility. This method was implemented by me and used in Ch. 3 and Ch. 4 of my thesis.

Finally, I properly discussed a method to reduce the cost of particle-to-wall interactions. To my best knowledge this idea haven't been introduced earlier. It was partially implemented and tested in my simulations.

Chapter 3

Homogeneous and heterogeneous populations of active rods in two-dimensional channels

3.1 Introduction

Active swarms are composed of individual self-propelled agents that are capable of converting energy into motion. Natural examples include bacterial swarms [64], bird flocks [11], fish shoals [9], and mammalian herds [145]. Anthropogenic examples include the behaviour of crowds [22, 23] and the flow of traffic [146]. In such systems the collective motion of a large number of simple individuals can result in complex non-equilibrium behaviour. While such phenomena are responsible for some of the most beautiful displays in the natural world, such as the murmuration of starlings or the collective motion of fish shoals; it can also be the source of deep inconvenience, such as, for example, the frustration of being stuck in stop-go traffic.

Recently, there has been considerable interest in the swarming of simple rod-like bacteria (for example, *Bacillus subtilis*) confined to the surface of a two-dimensional interface [34, 44, 63, 117]. Such swarms, captured within a free-standing film or between a solid-solid or solid-liquid interface, have the advantage that they can be imaged easily by real-space microscopy and provide an ideal environment for the study of active matter.

In this chapter I conduct numerical simulations of self-propelled rods on a (quasi-) two-dimensional surface. Such simulations provide an analogy for dense swarms of motile rod-like bacterial swarms on a flat interface. To prevent rods from overlapping I impose a simple steric interaction between rods: Each rod is divided into segments and segments from neighbouring rods repel each other using a Hookean potential. The model I am using was first introduced by Peruani *et al.* [126] to consider the effects of cell shape. It ignores hydrodynamic interactions due to the assumption that the cells are densely packed and move in a very viscous media. Myxobacteria gliding on a surface is an example of such a system [147], where the lengths of the rod-like bacteria are distributed heterogeneously. Similar approaches may use a repulsive Yukawa force that has been restricted to only act on overlapping rod segments [32]. The use of a Hookean potential has two advantages — first, the overlap energy between neighbouring rods scales in a simple manner, and second, by varying the magnitude of the spring constant the interaction between rods can be tuned continuously from soft to hard. Self motility is imposed by introducing a constant propulsion force along the axis of the rod. Collisions between rods are resolved into a force acting on the centre of mass and a torque that acts to change the orientation of the rod. The position and orientation of the rods, along with the centre of mass forces and torques, are used to perform an overdamped molecular dynamics simulation.

Despite the simplicity of the model it is capable of reproducing a wide range of behaviours commonly seen in dense bacterial swarms. Simulations of this type have provided insights into phenomena such as turbulence in active systems, corporative swarming, and alignment on long length scales [55]. In addition, features, such as *hedgehog*-like formations (whereby rods near a wall jam together forming a fan-shaped cluster) and giant density fluctuations were also successfully reproduced *in silico* [3, 32] and have been observed in real bacterial communities [28, 147] (and other active systems, e.g., Ref. [94]. The method has also been used to simulate directed

bacterial transport of mesoscopic carriers [117].

I study a swarm of self-propelled rods in a (quasi-)2D channel between two narrowly separated parallel walls. A similar confining geometry has been studied experimentally (and by means of simulations) by Wioland *et al.* [34]. I note that a key difference between the work of Wioland *et al.* and the present study is the effect of hydrodynamic forces, which I do not consider. Nevertheless, it was found by Wioland *et al.* that the nature of the flow could vary from turbulent to laminar depending on the width of the channel. I show that the presence of the channel boundaries leads to a layering effect whereby rods are densely packed along the channel boundaries, with subsequent internal layers forming behind the surface layer.

Previous studies (e.g., Refs. [32, 34, 138]) have focused on the highly idealised case of a homogeneous active population. These, however, are in contrast with the heterogeneity of natural environments, where multispecies swarms have been likened to moving ecosystems [148]. Even within a single species swarm, the cell aspect ratio may change, and this can be important for the ability of bacteria to swarm efficiently [149]. To date, typical studies of active matter have involved fully homogeneous populations or at most binary mixtures (e.g., with different chiralities [150–152], motilities [53, 153], or shapes [100, 154]). A notable exception is the study by active polydisperse disks which are found to form glassy states [3].

Here I directly consider the effect of heterogeneity in a population of active rods. I focus on the case where both the driving force for individual rods, and the nature of the steric interaction between any pair of rods, are chosen from a random distribution. The main finding is that the channel walls drive the segregation of a heterogeneous population, so that hard rods and strongly driven rods are found in greater concentrations at the channel boundaries. This finding may have consequences for developing passive systems that can sort or segregate bacterial populations by geometry alone.

This chapter is organised as follows. In Sec. 3.2 I describe my model and numerical scheme. Section 3.3 contains an analysis of the behaviour of dense homogeneous systems with various steric interactions. Following this, Secs. 3.4 and 3.5 are dedicated to heterogeneous active matter, where I define a heterogeneous system and investigate its properties by varying the self-propellant forces and steric interactions of the population.

3.2 Theory

3.2.1 Model

I consider a (quasi-) 2D system in which N active rods are confined within a rectangular channel of length L, width W, and area $A = LW$, where $L > W$. I define the origin of my coordinate system to lie in the middle of the strip and impose periodic boundary conditions on either side of the strip. In addition, distance is measured in units of diameter d, speed in units of $\mathcal{F}$, time in units of $d/\mathcal{F}$.

For computational ease, the rods are represented as a series of $2M + 1$ segments — i.e., disks of diameter d — stacked along the long axis of the rod. The distance between neighbouring segments is $l_o = d/2$ and in all my simulations I fix $M = 1$. Thus all my rods are composed of three segments — although clearly more segments can be included by increasing the value of M; see, for example, Refs. [55, 138].

A given rod is specified by its centre of mass point $\boldsymbol{C}_\alpha = (x_\alpha(t), y_\alpha(t))$ and by its orientation, given by the unit vector $\hat{\boldsymbol{u}}_\alpha = (\cos\theta_\alpha, \sin\theta_\alpha)$ [see Fig. 3.1(a)]. In addition, I also define the unit vector $\hat{\boldsymbol{v}}_\alpha = (-\sin\theta_\alpha, \cos\theta_\alpha)$ perpendicular to $\hat{\boldsymbol{u}}_\alpha$. Hence, the coordinates of the ith segment from the αth rod is given by,

$$\boldsymbol{r}_{\alpha,i} = \boldsymbol{C}_\alpha + i l_o \hat{\boldsymbol{u}}_\alpha,$$

where i is an integer ranging from $[-M, M]$ (so that if $M = 1$ I have $i = -1, 0, 1$).

Steric interactions between rods are implemented by pairwise interactions between *overlapping* segments from different rods; see Fig. 3.1(b). I define a repulsive interaction between segment i from rod α with segment j from rod β as being given by,

$$U^{ij}_{\alpha\beta} = \begin{cases} \frac{1}{2}\kappa(d - \Delta r^{ij}_{\alpha\beta})^2 & \text{if } \Delta r^{ij}_{\alpha\beta} \leq d, \\ 0 & \text{if } \Delta r^{ij}_{\alpha\beta} > d, \end{cases} \tag{3.1}$$

where $\Delta r^{ij}_{\alpha\beta} = \left|\boldsymbol{r}^i_\alpha - \boldsymbol{r}^j_\beta\right|$ is the distance between the centres of the segments, κ is the strength of the interaction and d is the segment diameter. Note the interaction energy falls to zero when there is no overlap between the segments thus giving a short-range force.

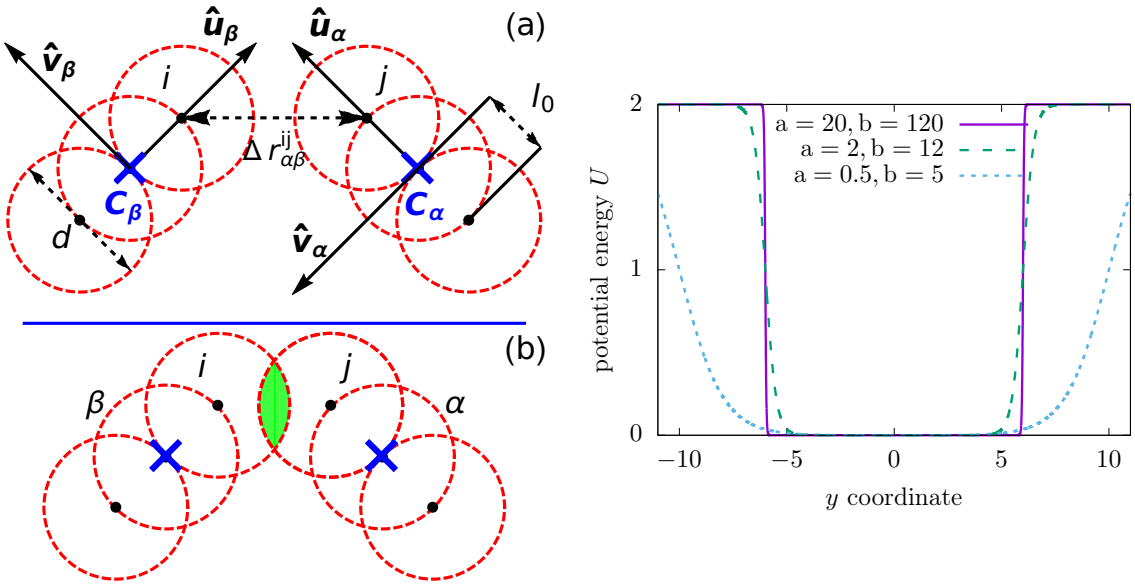

Figure 3.1: Left: (a) The diagram shows two rods α and β. Each rod is defined by a centre of mass (crosses showing $\boldsymbol{C}_\alpha$ and $\boldsymbol{C}_\beta$, respectively) and a unit vector ($\hat{\boldsymbol{u}}_\alpha$ and $\hat{\boldsymbol{u}}_\beta$, respectively) pointing along the forward direction of the rods. Each rod is composed of a series of $2M+1$ segments (of diameter d) stacked along the unit vector. The distance between successive segments is fixed to be $l_0 = d/2$. A self-propellent force $\mathcal{F}_\alpha; \mathcal{F}_\beta$ is directed along the corresponding unit vector $\hat{\boldsymbol{u}}_\alpha; \hat{\boldsymbol{u}}_\beta$ and drives the rod forward. (b) If there is an overlap between segments from two different rods (as shown by the shaded (green) region) then there exists a repulsive force between segments where $\Delta r^{ij}_{\alpha\beta} < d$ between segments i and j, as given by Eq. 3.1.
Right: A plot of the the confining potential $U^B_{\alpha,i}(a,b)$ for selected values of a and b. I plot only the cross-sections since scaling the length L does not bring new effects. In my simulations I set $a = 20.0$ and $b = 120.0$.

The rods are prevented from escaping through the walls of the channel (located at $y = \pm W/2$) by a repulsive force as shown in Fig. 3.1. This is modelled as a steric interaction between each segment in a given rod and the bounding walls of the channel. The bounding potential experienced by the ith segment in the αth rod is,

$$U^B_{\alpha,i}(a,b) = \tanh(-ay_{\alpha,i} - b) + \tanh(ay_{\alpha,i} - b) + 2, \tag{3.2}$$

where the width of a channel is defined as $W = 2b/a$ and both constants a and b define the slope as well.

Thus, the total force acting on the rod is the sum of the steric forces and the self-propellant forces, and is given by,

$$\boldsymbol{F}_\alpha = -\sum_{i=-M}^{i=M} \boldsymbol{\nabla} U_{\alpha,i} + \mathcal{F}_\alpha \hat{\boldsymbol{u}}_\alpha, \tag{3.3}$$

where the first term in Eq. (3.3) accounts for the potential acting on the ith segment of the αth rod due to all the steric interactions, i.e.,

$$U_{\alpha,i} = U^B_{\alpha,i}(a,b) + \sum_{\alpha\neq\beta}^{N} \sum_{j=-M}^{j=M} U^{ij}_{\alpha\beta}. \tag{3.4}$$

The second term in Eq. (3.3) is the self-propellant force of magnitude F_α acting along the direction of the rod, which drives it forward. The total force $\boldsymbol{F}_\alpha$ can be decomposed into a component acting on the centre of mass of the rod along the main axis and its orthogonal counterpart:

$$\boldsymbol{F}^{\text{c.o.m.}}_\alpha = (\boldsymbol{F}_\alpha \cdot \hat{\boldsymbol{u}}_\alpha)\hat{\boldsymbol{u}}_\alpha + (\boldsymbol{F}_\alpha \cdot \hat{\boldsymbol{v}}_\alpha)\hat{\boldsymbol{v}}_\alpha. \tag{3.5}$$

In addition, due to asymmetric shape of active rods, forces acting on segments induce a torque:

$$\boldsymbol{\tau}_\alpha = \sum_{i=-M}^{i=M} (\boldsymbol{r}_{\alpha,i} - \boldsymbol{C}_\alpha) \times \boldsymbol{F}_{\alpha,i}. \tag{3.6}$$

3.2.2 Numerical Scheme

I model the dynamics of the rods using overdamped Langevin equations for translational and rotational motion (see Sec. 2.2). My systems have zero noise — thus, the dynamics is purely deterministic. Moreover, since I am interested in collision-induced dynamics only, I omit all hydrodynamic interactions so that active matter is "dry".

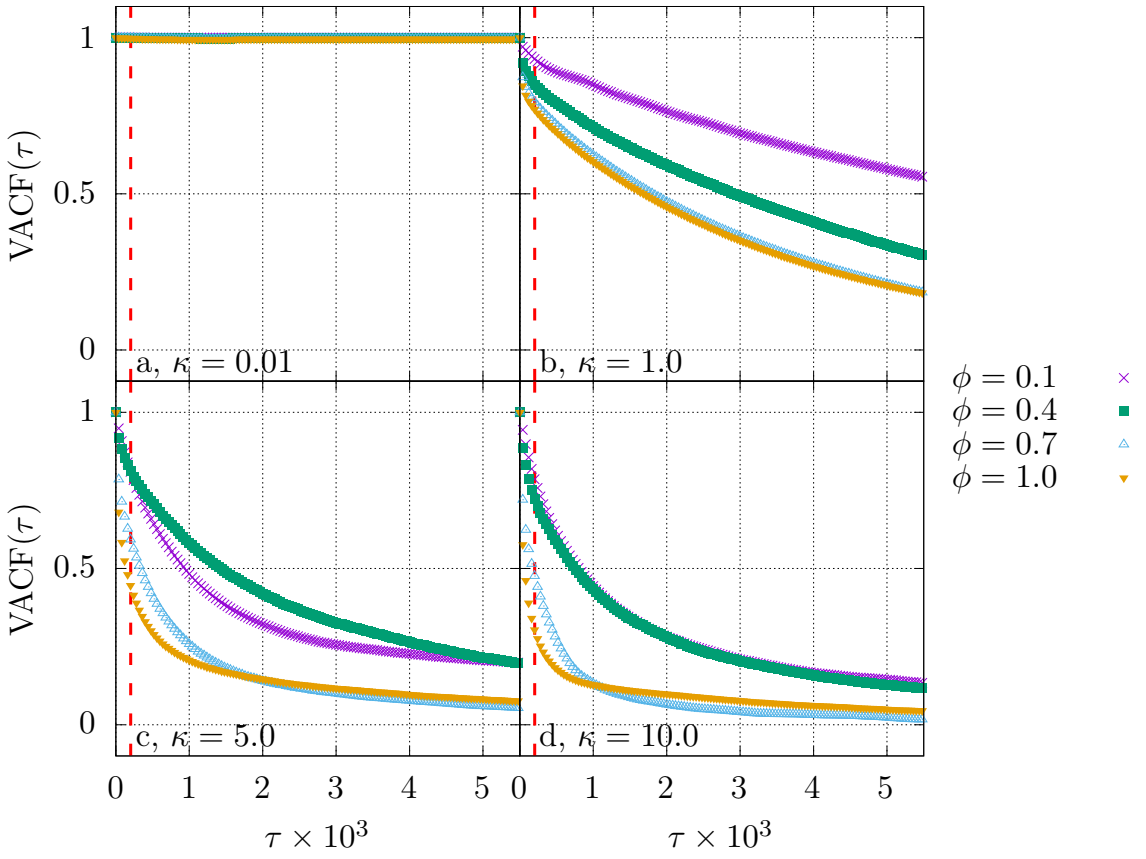

Figure 3.2: Velocity autocorrelation function (VACF) as a function of time lag τ for different values of packing fraction ϕ and $\kappa = 0.01, 1, 5, 10$. Red dashed line denotes the point where $\tau = 200$. Aside from the case of $\kappa = 0.01$ where all interactions are negligible resulting in non-decaying VACF for all densities all other systems exhibit similar behaviour. In particular, harder particles loose memories of their previous state faster since inter-particle collisions start playing more significant role in collective dynamics changing the direction of motion as well as speed greatly. Increasing ϕ results in a similar pattern. The number of points is intentionally reduced to make the figure more readable, that includes only 4 values of ϕ and 1% of data points per graph.

I obtain the rod dynamics by using a first-order Euler integration scheme. The

initial conditions for all simulations is that the rods are placed and orientated randomly and uniformly (i.e., equally distributed) in the channel. I run each system for a period of $t_0 = 10^5$ iterations (200 time units, i.e. the transient phase of the simulation) so that initial effects have — at least partially as I explain right below — died away before continuing the simulation for a longer time period of 5×10^6 over which I collect data and make measurements. This particular choice of the transient period has been made after measuring the velocity autocorrelation functions in various active systems discussed in this chapter. I note here that not all systems forget their initial states *completely* in a reasonable amount of time (see, for example, Fig. 3.2,b) so this approach should be considered a rule of thumb rather than a general principle. Depending on the parameters autocorrelations can drop relatively rapidly from 1 to $0.3 - 0.5$ instead of zero and keep decaying at much lower rates. Whereas the systems do not settle down completely due to non-conservative nature of active matter they reach a certain state of pseudo-stability. That's been confirmed by measuring various metrics such as average speed and orientation as well as by visual observations of the systems at different times.

By approximating each rod as a 2D spherocylinder, the packing fraction (i.e., the ratio of the total area of all rods relative to the channel area) is given as [55],

$$\phi = \frac{N}{A}\left(2dMl_0 + \frac{\pi d^2}{4}\right), \tag{3.7}$$

when there is no overlap between segments from adjacent rods assumed.

In the following simulations I use a channel of length $L = 120d$ and width $W = 12d$. The resulting area A of a domain is thus given by $L*(W+d)$, where d is a constant term introduced due to the point-like nature of active rods. This choice provides a channel which is sufficiently long for the rods to self-organize into a collective flow and sufficiently narrow as to prevent large scale vorticity from developing. In all simulations I consider dense ($\phi = 1.1$ to have reliable statistics in every region of

the channel) populations of active rods in periodic channels. However, there is a distinction between the packing fraction (reduced number density) ϕ and the true packing fraction in systems with soft particles. When using the former, the area of overlaps is counted more than once potentially resulting in values greater than one. The latter doesn't allow such an option and is always ≤ 1.0 [155].

3.3 Homogeneous population of rods in a periodic rectangular channel

I consider a homogeneous population of rods. Every rod α has same driving force $\mathcal{F}_\alpha = \mathcal{F}$ (where I set $\mathcal{F} = 1$), each rod segment has the same diameter $d = 1$ and hardness $\kappa_\alpha = \kappa$. Hence, the properties of the system depend *almost* solely on the ratio,

$$\gamma = \frac{d\langle\kappa_\alpha\rangle}{\langle\mathcal{F}_\alpha\rangle}, \tag{3.8}$$

(the exception to this is the confining potential used to simulate the wall boundaries, which does not depend on κ). Here I investigate the effect of γ on the distribution of rods in the channel.

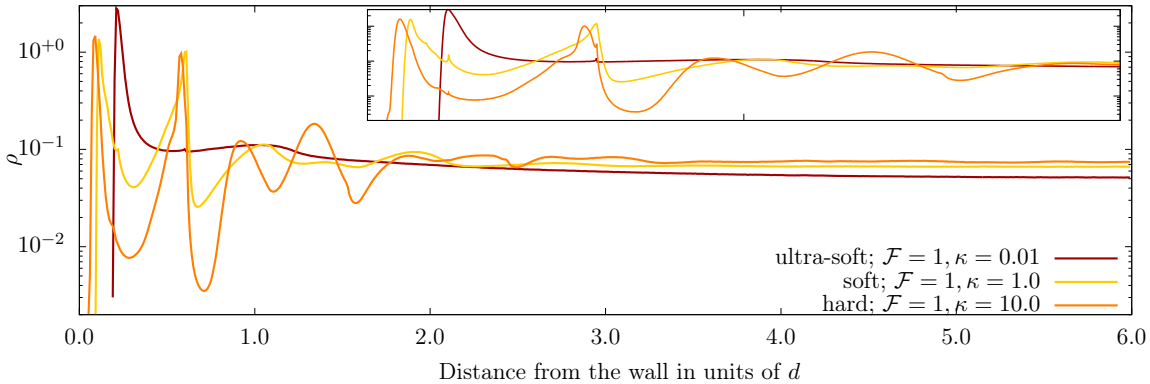

Figure 3.3: Rod density averaged over 100 realizations for rods in a channel. The inset contains a magnification of the region $\lambda \in [0 : 2]$.

For each realization, after the initial transient period I identify the centre-of-mass $\boldsymbol{C}_\alpha$ for each rod and compute the rod density distribution (using the standard procedure [135, 156]), given by:

$$\rho(\boldsymbol{r}) = \langle \sum_{\alpha=1}^{N} \delta(\boldsymbol{r} - \boldsymbol{C}_\alpha) \rangle_t. \tag{3.9}$$

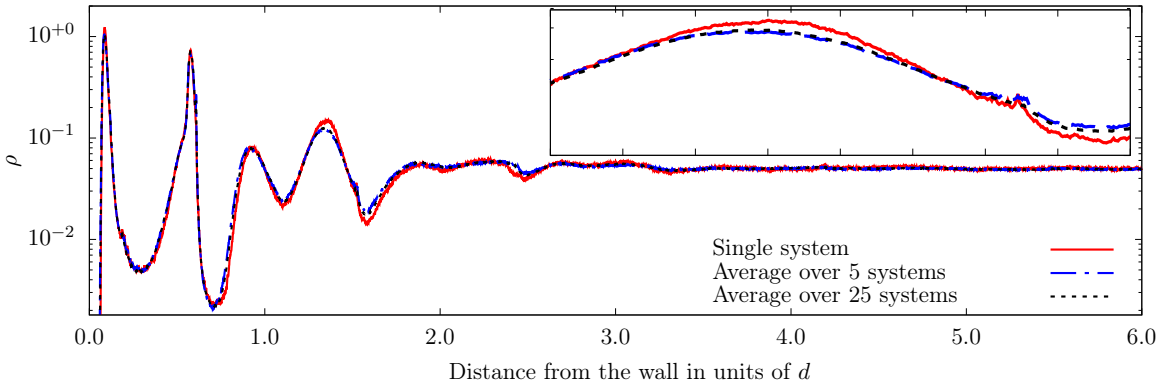

Figure 3.4: Rod density for one system (solid red line), average of 5 systems (dashed blue line) and average of 25 systems. The inset contains a magnification of the region $\lambda \in [1.2 : 1.6]$.

To obtain an average density distribution I also average over a series of snapshots from a given run and over an ensemble of 100 realizations (where each realization is obtained by starting the system from a random initial configuration). The average of realizations starts to converge when the total number of them is $25 - 30$ and barely changes when it is 50. To make it even more robust I doubled it up to 100. I provide an example of such convergence in Fig. 3.4, it is possible to notice that results for 5 systems and for 25 systems are barely distinguishable but the magnitude of noise reduces greatly as the number of realizations increases.

This results in an averaged distribution as plotted in Fig 3.3, in terms of distance from the wall $\lambda = \frac{W}{2} - |y|$. The function is computed by dividing the channel into strips parallel to the channel axis and counting the number of rod centres within the strip. In addition, I normalize by the strip width and by $1/N$ to have comparable results in systems with different populations.

I find that for soft steric interactions, i.e., $\gamma = 1$, most of the rods are concentrated at the boundaries of the channel, with a few rods in the interior (see yellow line in Fig. 3.3, and the top image in Fig 3.5). This is apparent as a large peak in the rod density close to the boundary wall followed by a second layer. After these surface layers the density is observed to drop rapidly. In the limiting case of ultra-soft interactions (such as $\gamma = 0.01$, as shown by the red line in Fig. 3.3), due to the extremely low repulsive forces almost all the rods are concentrated near the walls, tending to form a single boundary layer.

When steric interactions dominate (i.e., $\gamma = 10.0$) the rods are distributed more uniformly throughout the channel (see Fig. 3.3, orange line, and bottom image in Fig 3.5). In contrast to the soft systems, I observe a series of oscillations in the density going from the wall toward the interior indicating a layer like ordering.

The differences between the soft ($\kappa = 1.0$) and hard ($\kappa = 10.0$) regimes can be readily observed in a typical snapshot of the system. As shown in Fig 3.5, in soft systems the rods pile up at the boundaries forming short lived structures called *hedgehogs* [32, 34, 157], while in the hard regime the rods are spread more evenly throughout the system and *hedgehogs* are not observed.

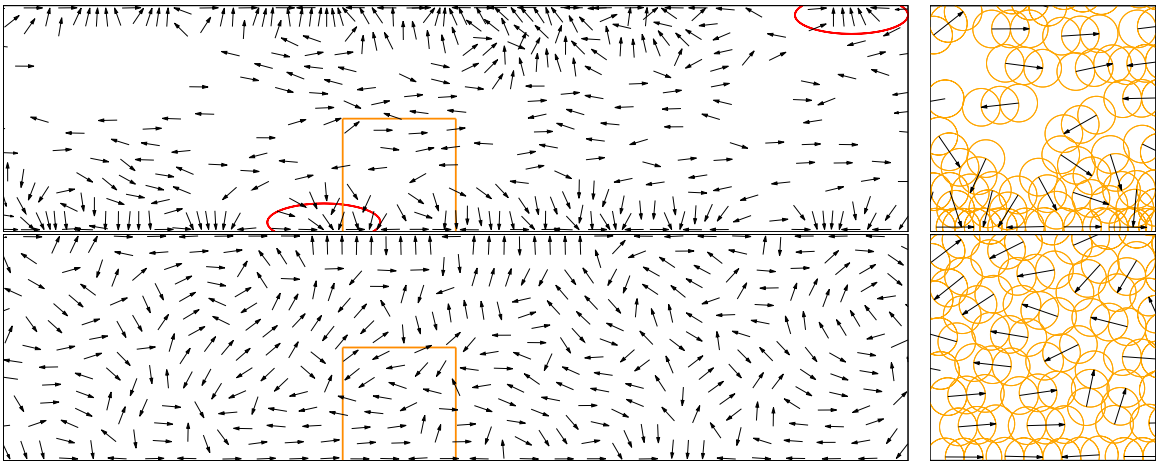

Figure 3.5: Top: $\gamma = 1.0$ (soft regime) and bottom $\gamma = 10.0$ (hard regime). *Hedgehog* structures are highlighted with (red) ellipses. Right column contains magnified boundary regions with plotted segments. In the case of strong repulsive forces strong layering is observed.

3.4 Heterogeneous populations in a periodic rectangular channel

My approach for heterogeneous systems is similar to that taken for the homogeneous cases described above in terms of simulation protocol, analysis, and numerical method.

While in the case of homogeneous populations each rod in the system has the same hardness κ and the same driving force $\mathcal{F}$, – in the heterogeneous cases considered below I randomly assign one (or both) of these parameters for the population. The cases I consider are: (i) keeping the hardness κ the same for every rod while choosing a random value $\mathcal{F}$ for the self-propellant force (picked from a uniform distribution for each rod); (ii) keeping the self-propellant force the same for each rod while assigning a random value κ for the hardness. Following this, in Sec. 3.5 I explore the problem of assigning a random value for κ *and* $\mathcal{F}$ to each rod in the population. I call these latter mixtures *doubly heterogeneous* populations.

My main finding is that in heterogeneous populations the presence of the channel boundaries leads to the demixing or segregation of rods. As in the homogeneous case where a strong layering effect is observed at the boundaries, so too in the heterogeneous populations I observe similar effects. However, here the rods are stratified into a sequence of layers, where the properties of the rods within a layer are roughly the same.

While the problem of mixed populations has been studied by some authors, they have mostly examined the case of binary mixtures. Here, two species with different motilities have been found to demix in periodic channels [53]: The fast moving rods are found in greater concentrations near the confining walls, while the slow rods are expelled to the interior. I show that this trend holds true even for populations where the motilities and hardness of the constituent rods are chosen from a continuous range of values.

3.4.1 Heterogeneous populations with randomly assigned self-propellant forces

The first case is where the magnitude of the self-propellant force, for each rod, is assigned a random value picked from a uniform distribution $\mathcal{F}_\alpha \in [1, 2) \quad \forall \alpha$. The hardness of all the rods in the population is assigned a single value κ, with sets of experiments generated with different values of κ.

Figure 3.6 shows a representative snapshot of a system (with $\kappa = 10.0$ and randomly assigned self-propellant forces) after the transient phase of the simulation. Fast and slow moving rods are coloured yellow and purple, respectively, a colour bar shows the range of $\mathcal{F}_\alpha$ values between these two extremes.

I refer to Secs. 3.2 and 3.3 for general details of the simulation procedure. Here I note that every time I simulated the system each rod started with its own random initial configuration (position and orientation) *and* a randomly assigned value for the self propellant force. In the first case I set $\kappa = 1.0$ (i.e., soft interactions) and ran 100 simulations. This provided an ensemble on which I base my averaged results (as described below). Following this I ran the same experiment with $\kappa = 10.0$ (i.e., hard interactions).

The question I am interested in answering is the following: Do rods segregate so that the strongly driven rods are found in greater concentrations toward the boundaries? To answer this I split the channel into a series of narrow strips (along the length of the channel) and for some quantity of interest $\mathcal{A}$ (e.g., the self-propellant force of the rods $\mathcal{F}$, their orientation θ, density ρ, and speed $|\boldsymbol{V}|$) I compute the average value of that quantity in the strip:

$$\langle \mathcal{A} \rangle (\boldsymbol{r}) = \frac{\langle \sum_{\alpha=1}^{N} \mathcal{A}_\alpha \delta(\boldsymbol{r} - \boldsymbol{C}_\alpha) \rangle_t}{\langle \sum_{\alpha=1}^{N} \delta(\boldsymbol{r} - \boldsymbol{C}_\alpha) \rangle_t}. \tag{3.10}$$

An analysis of the systems with $\kappa = 1.0$ and $\kappa = 10.0$ is summarised in Fig. 3.7.

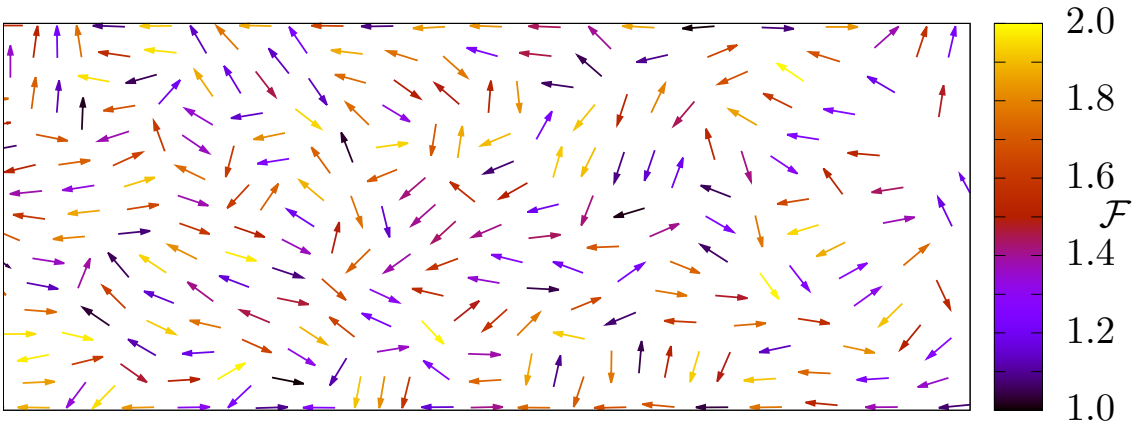

Figure 3.6: A snapshot of a system with heterogeneous self-propellent forces. All active rods are represented by arrows coloured according to the values of their assigned self-propellant forces; the colour bar shows the range of $\mathcal{F}$ magnitudes, whilst $\kappa = 10.0$ in this case.

I interpret Fig. 3.7 as follows. The plot of the density distribution ρ shows a large concentration of rods at the boundaries where $\lambda \approx 0$ regardless of the value of κ. These surface rods are orientated *parallel* to the walls (as inferred from the the orientation parameter $\langle \sin^2 \theta \rangle$) and are on average more strongly driven than the rods in the interior (as shown by plotting $\langle \mathcal{F} \rangle$) — similar to previous studies of mixed populations [3]. Thus, a universal feature of these systems is that strongly driven rods are found at the channel boundaries as the result of an *expelling* process [3] whereby weakly driven rods are pushed out of the surface layer. However, the distribution of rods is also sensitive to the choice of κ, so that the layer-like ordering is less pronounced in softer systems. I also observe a slight decrease in the average motility of the rods, i.e., $\langle \mathcal{F} \rangle$, at the boundaries as I increase the steric forces between rods.

Adjacent to the surface layer I observe a second spike in the density at $\approx 0.5\lambda$ (blue dashed line in Fig. 3.7), which is particularly sharp when steric interactions are strong. This is generated by rods which are also in contact with the wall but are orientated *perpendicular* to it (as inferred from the plot of the orientation parameter). This second layer consists of rods which are weakly driven (compared to first layer)

and are trapped against the channel wall. Since they are perpendicular to the wall they do not contribute to actively pushing the surface layer of of rods. These rods are unable to reorientate themselves due to strong *caging* [100] and are dragged along by the faster rods in the surface layer. Subsequent layers, particularly for hard systems, show some of the features of the two outer layers, but it becomes increasing difficult to distinguish distinct layers as I go into the interior of the system.

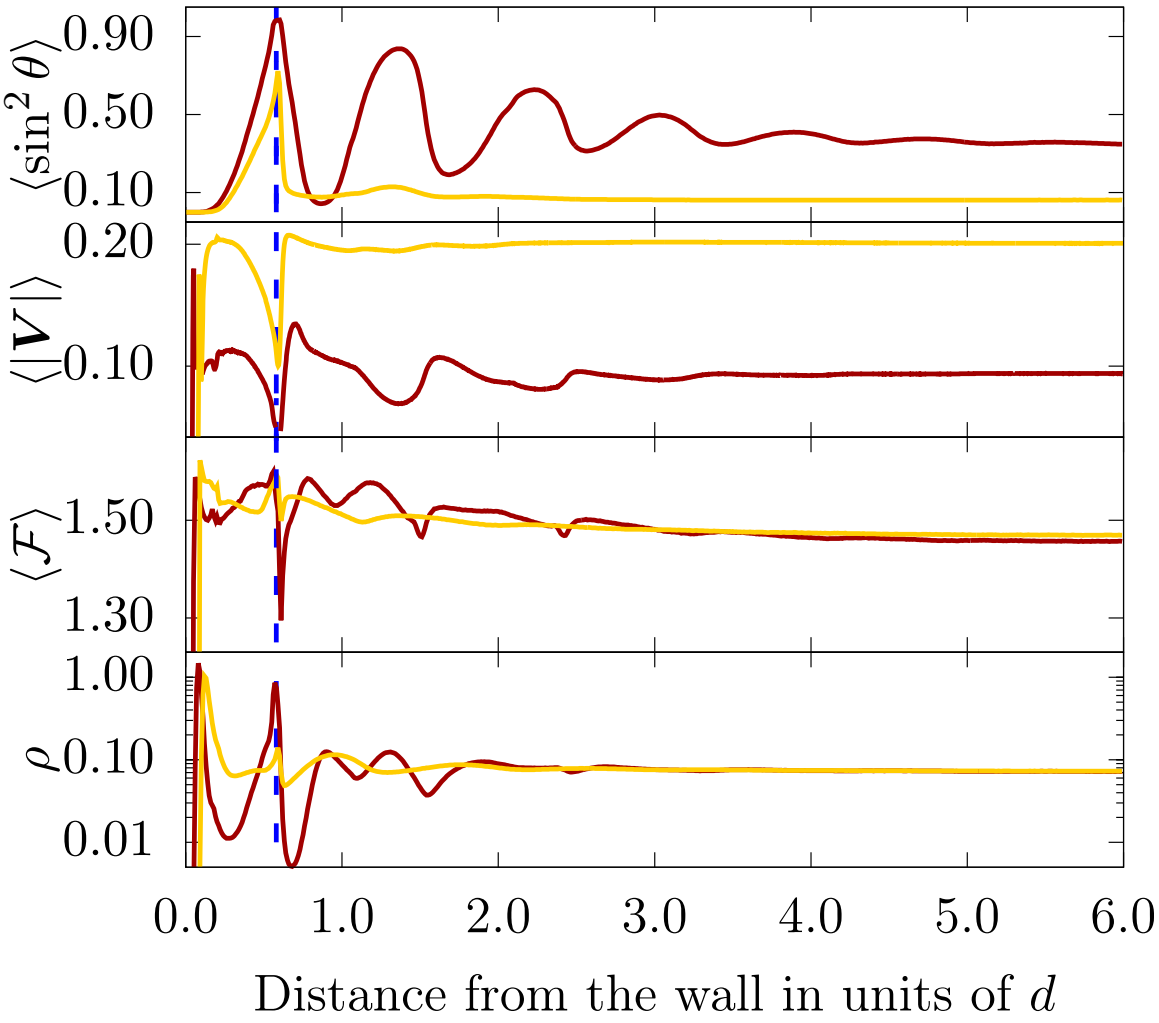

Figure 3.7: From top to bottom: average order parameter $\sin^2\theta$, average speed $|\boldsymbol{V}|$, average self-propellant force $\mathcal{F}$, average density ρ; $\sin^2\theta = 0$ means parallel to walls, whereas $\sin^2\theta = 1$ means perpendicular. Red and yellow curves denote systems with $\kappa = 10.0$ ($\gamma \approx 6.67$) and $\kappa = 1.0$ ($\gamma \approx 0.67$), respectively. The self propellant force for each rod is picked from a uniform distribution as described in the text. The system consists of a dense layer of rods at the channel walls followed by subsequent layers in the interior (the second one is highlighted by a vertical dashed line).

3.4.2 Heterogeneous populations with randomly assigned repulsive coefficients

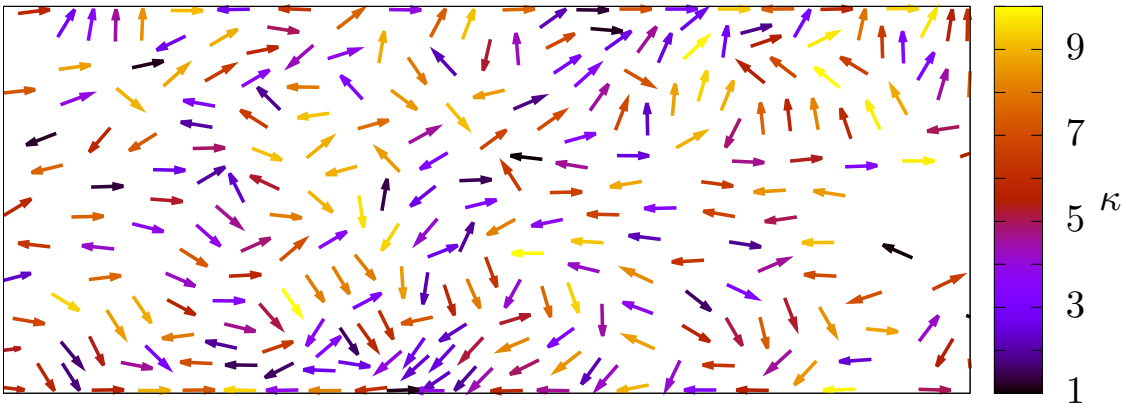

Figure 3.8: A snapshot of a system with heterogeneous softness. All active rods are represented by arrows coloured according to the values of their assigned hardness; the colour bar shows the range of κ magnitudes, while $\mathcal{F} = 1.0$ in this case.

I now consider the inverse situation whereby every rod has its own randomly assigned value of κ (taken from the uniform distribution, $\kappa \in [1.0, 10.0)$, but the magnitude of the self propellant force $\mathcal{F}$ for each rod in the population is the same, with sets of experiments generated with different values of $\mathcal{F}$.

To compute the interaction between rods with different hardnesses I introduce a Lorentz-Berthelot [158] combining rule for an effective potential. For any two rods α and β the average κ for the interaction between them, is given by,

$$\kappa_{\alpha\beta} = \sqrt{\kappa_\alpha \kappa_\beta}. \tag{3.11}$$

Figure 3.8 shows a representative snapshot for a system with $\kappa \in [1.0, 10.0)$ and $\mathcal{F} = 1.0$. Soft and hard rods are coloured blue and yellow, respectively, while a colour bar indicates rods with hardnesses intermediate between these two extremes.

As before I plot the averaged quantities of the system in Fig. 3.9 and find that the system is composed of a series of layers. The outer layer with $\lambda \approx 0.0$ is composed on average of the hardest rods. Surprisingly, the average velocity of the rods in this

layer is relatively high compared to the rest of the system. Next to the outermost layer is an internal layer of slower moving softer rods which are perpendicular to the walls. Immediately behind these surface layers is a region containing very soft rods which are locally trapped into dense clusters.

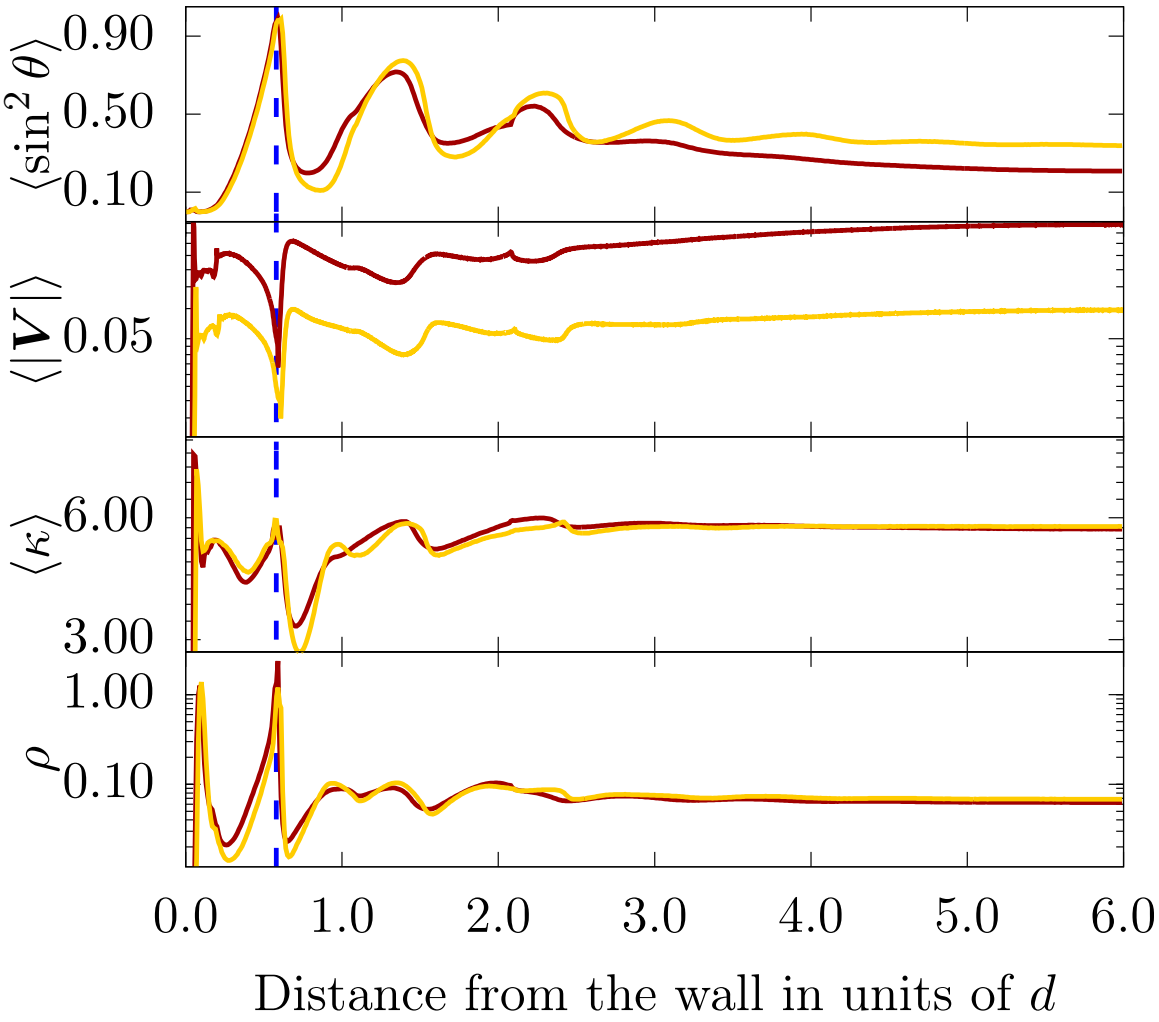

Figure 3.9: From top to bottom: average order parameter $\sin^2\theta$, average speed $|\boldsymbol{V}|$, average hardness κ, average density ρ. Red curves denote systems with $\mathcal{F} = 2.0$ ($\gamma = 2.75$), yellow curves with $\mathcal{F} = 1.0$ ($\gamma = 5.5$). The hardness of the rods is picked from a uniform distribution as described in the text. The first of internal layers is indicated by the vertical dashed line.

3.5 Doubly heterogeneous systems in a rectangular channel

The final case is where both the hardness and the self-propellant force for each rod is assigned from a random distribution. I use the same distributions as in the previous cases, that is $\kappa \in [1.0, 10.0)$ and $\mathcal{F} \in [1, 2)$, resulting in $\gamma \approx 3.67$.

A representative snapshot of the system is shown in Fig. 3.10, where the top figure shows the rods coloured according to their assigned self propellant force and the bottom figure shows the same rods coloured according to hardness.

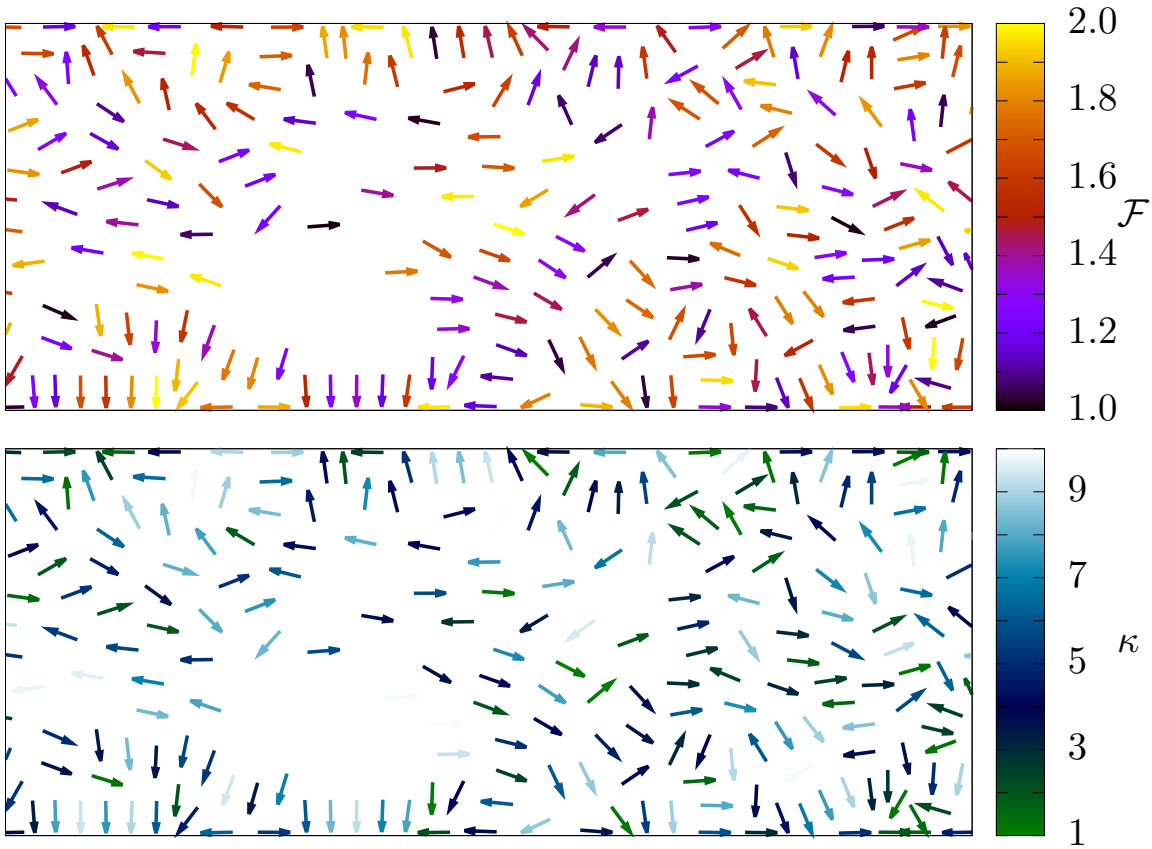

Figure 3.10: Snapshots of a doubly heterogeneous system. Top: rods are coloured according to their values of $\mathcal{F}$; bottom: rods are coloured according to their values of κ.

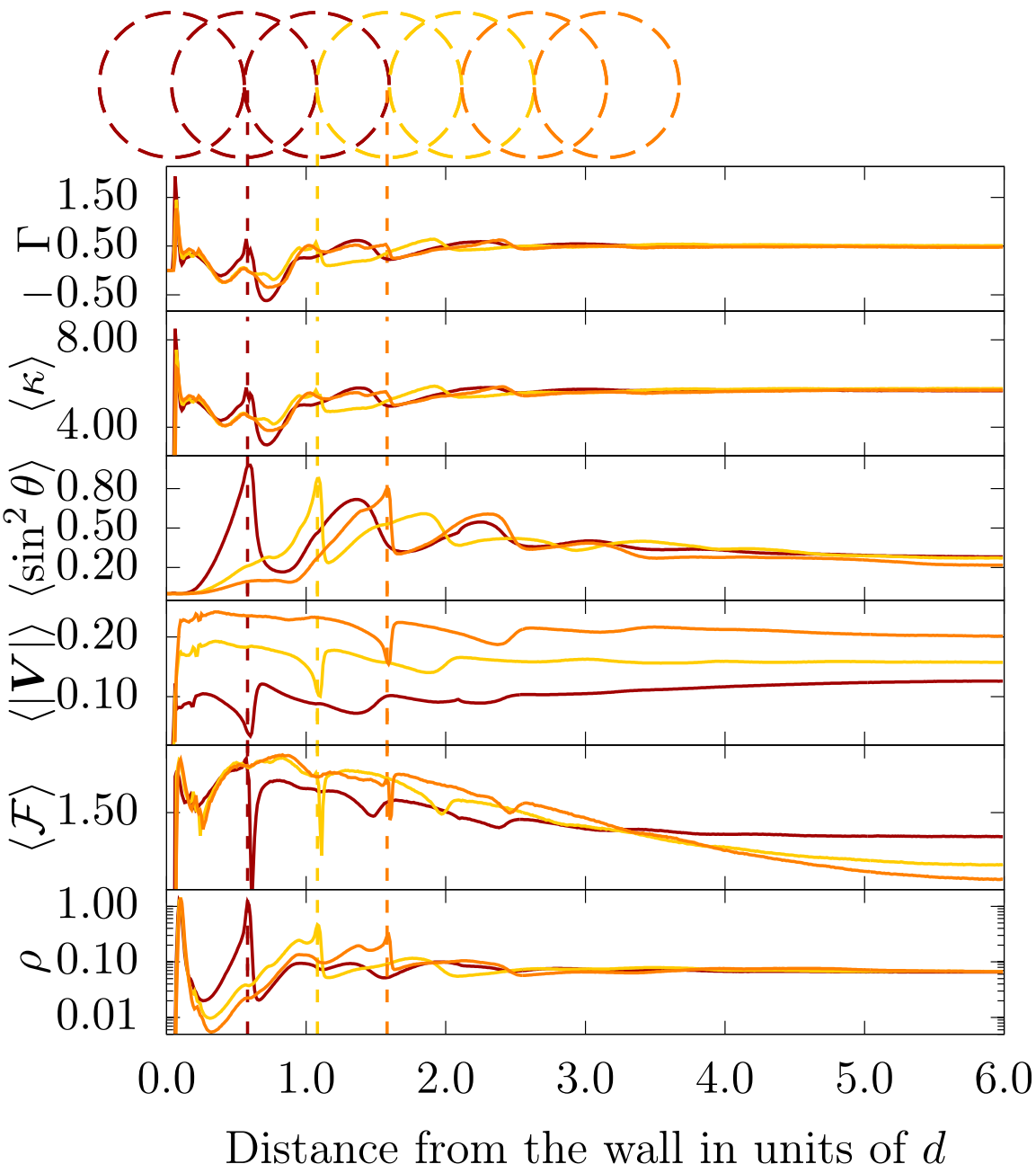

Figure 3.11: Distributions in doubly mixed systems, from top to bottom: Γ defined by Eq. (3.12), average hardness κ, average order parameter $\sin^2\theta$, average speed $|\boldsymbol{V}|$, average self-propellant force $\mathcal{F}$, and average density ρ. Values of κ and $\mathcal{F}$ of the rods are picked from uniform distributions as described in the text. Red curves denote systems where rods are composed of three segments, yellow and orange stand for systems with five and seven segments, respectively. The first of the internal layers is indicated by the vertical dashed line of corresponding colour. Subsequent layers are also highlighted by dashed lines. The disks at the top of the figure represent rods of different lengths aligned perpendicularly to the wall, corresponding to the peaks in the graphs.

The behaviour of the system can again be understood with reference to the various quantities plotted in Fig. 3.11. This doubly mixed system shows features from both the previous cases. The system is again composed of dense layers at the boundaries, but this time I find that the outermost layer consists of rods which are on average highly motile in terms of $\mathcal{F}$ *and* the hardest. In the particular case studied here, I observe evidence of subsequent layers but these decay quickly to give way to a disordered interior.

To ensure that these results are not specific to a single aspect ratio (that is length of rod versus its width) I show the outcome for simulations for a range of rod lengths (specifically rods composed of three, five, and seven segments in length) — see Fig. 3.11. In all cases I find there is an outer layer, composed of rods parallel to the walls, followed by a second layer at a distance half the length of the rod (i.e., composed of rods at the wall boundaries which are perpendicular to the walls).

To show that active rods at the boundaries are *both* motile and hard, I introduce a metric:

$$\Gamma(\boldsymbol{r}) = \frac{\langle \sum_{\alpha=1}^{N} (\mathcal{F}_\alpha - \bar{\mathcal{F}})(\kappa_\alpha - \bar{\kappa}) \delta(\boldsymbol{r} - \boldsymbol{r}_\alpha) \rangle_t}{\bar{\mathcal{F}} \bar{\kappa} \langle \sum_{\alpha=1}^{N} \delta(\boldsymbol{r} - \boldsymbol{r}_\alpha) \rangle_t}, \tag{3.12}$$

where $\bar{\mathcal{F}}$ and $\bar{\kappa}$ are the average motility and hardness of the rods, respectively. Thus, positive Γ corresponds to rods that are either hard with high self-propellant forces or soft with low self-propellant forces. Figure 3.11 shows that Γ has a strong peak right next to the wall. Furthermore, because both $\langle \kappa \rangle$ and $\langle \mathcal{F} \rangle$ are high in this region I deduce that the layer of surface rods is (on average) formed by hard rods with high self-propellant forces.

3.6 Conclusions

I have studied the properties of a swarm of actively driven rods in a rectangular channel. I have compared the case of a homogeneous swarm to that of a heterogeneous

swarm (whereby one or more of the dynamical features are randomly assigned).

In the case of the heterogeneous systems my key finding is that the channel wall drives the segregation of the population. Thus rods which are hard and fast moving are more likely to be found at the edge of the system, while soft and less motile rods are pushed in to the interior. I have deliberately confined these simulations to narrow channels and it remains to be seen if these results apply to wider systems in which vortex type behaviour is commonly seen.

While these features have been hinted at by previous simulations of binary mixtures of rods, here I demonstrate that segregation is present even in systems where the dynamical properties are given by a continuous range — as is the case for many bacterial communities.

An important test case for these findings maybe the work of Ilkanaiv *et al.* [149], where swarming *Bacillus subtilis* move on surfaces. In this experimental study the rod-like bacteria have their lengths and motilities distributed heterogeneously. For such populations I expect to see segregation if the bacteria are in the presence of a wall or confined within a channel.

While the system studied here is idealised model of some active systems (e.g., bacterial populations), nevertheless I hope that these findings might hint at a passive means of sorting active populations according to their dynamical properties. Indeed, these findings already suggest that boundaries can be used to enhance the concentration of rods with high motilities and strong steric interactions. The design of channel geometries that can then syphoned off these rods from the rest of the population (and their efficiency as sorting devices) will be the subject of my future publications.

Chapter 4

Statistical properties of confined active matter

4.1 Introduction

Active matter can exhibit a lot of patterns that can't be observed in passive systems. This also means that there are some statistical properties of active matter that are non-trivial as well. This chapter contains various metrics that have been used during my research but for some reasons haven't been included in Ch. 3.

4.1.1 Model & numerical scheme

I refer to Ch. 3 for a detailed explanation of the numerical scheme and the model used here as they are absolutely identical. Supplementary information is provided in the text below when required.

4.2 Mean squared displacement

4.2.1 Mathematical foundation

Visual observations of active systems reveal different possible regimes of motion that depend on system parameters such as $\kappa, \phi, \mathcal{F}$. Whereas such dynamic states can be classed manually, using the snapshots of systems at different times, a more robust way is to introduce a metric which value almost definitely characterizes the motion of

active rods. The difference between the dynamics of the hard and soft regimes can be observed by computing the mean squared displacement (MSD) for the centre-of-mass of the rods. I define the MSD according to Ref. [159] as a function of the lag τ between two different temporal states of a system:

$$\langle r^2 \rangle(\tau) = \left\langle \frac{1}{N} \sum_{\alpha=1}^{N} (\mathbf{C}_\alpha(t+\tau) - \mathbf{C}_\alpha(t))^2 \right\rangle_t , \tag{4.1}$$

where $\langle \cdot \rangle_t$ denotes canonical time average over a series of reference times t.

According to classical Brownian theory [159], there are two possible regimes of motion: ballistic when $\langle r^2 \rangle \propto \tau^2$ and diffusive when $\langle r^2 \rangle \propto \tau$. However, in general it's possible to observe more exotic phenomena with anomalous diffusion $\langle r^2 \rangle \propto \tau^\mu$ (super-diffusive or sub-ballistic regimes) where the anomalous diffusion exponent μ is not limited by two values $\{1, 2\}$ but rather can lie in range $[0, 2]$. In this case the upper limit is a purely ballistic motion and the lower one is a jammed state (in the sense that rods can't leave their local neighbourhood).

In the case of a swarm the displacement of the collective centre of mass can be non-zero [3, 160]. Thus, all my MSD measurements contain a centre of mass correction,

$$\mathbf{C}'_\alpha(t) = \mathbf{C}_\alpha(t) - \frac{1}{N} \sum_{\alpha=1}^{N} \mathbf{C}_\alpha(t),$$

this gives the diffusive behaviour of the rods without the background motion. The total distance traversed by a single active rod is calculated by 'unfolding' the x co-ordinate. The procedure for this is the following: every time a particle crosses the boundary, its corresponding folding number (index) is increased or decreased by one. Thus, at each time step it is possible to recover the total distance through multiplication of the index by the length of the channel and adding the position of the particle within the domain. The final formula for the displacement $\langle \tilde{r}^2 \rangle$ with the average flow

removed is,

$$\langle \tilde{r}^2 \rangle(\tau) = \left\langle \frac{1}{N} \sum_{\alpha=1}^{N} (\mathbf{C}'_\alpha(t+\tau) - \mathbf{C}'_\alpha(t))^2 \right\rangle_t . \tag{4.2}$$

An example of measurements based on equations 4.1 and 4.2 is presented in Fig. 4.1. From this I see that rods may move collectively along the channel in a ballistic manner, however, once the background motion is adjusted for I find that individual rods are seen to move diffusively, only reaching a relatively small distance (as compared to the centre of mass) from a given reference point within the time lag τ.

I can breakdown the example shown in Fig. 4.1 into a purely ballistic regime at short times, followed by an intermediate crossover point, and a diffusive-like behaviour at the end. From the last of these I can approximate the log-scaled mean squared displacement measurements with a linear function and extract an anomalous diffusion exponent μ (i.e. the gradient of the fitted line in Fig. 4.1):

$$\langle \tilde{r}^2 \rangle(\tau) \sim \tau^{\mu}. \tag{4.3}$$

Thus I can compute the exponent for the diffusive regime as a function of the system packing fraction ϕ, or as a function of the dynamical properties of the rods (i.e. by varying γ). I also suggest a more detailed analysis of the dynamics of active rods as a potential extension of this work. Rather than studying the whole displacement it is possible to study its spatial components independently. This may provide a better insight for this type of confined systems. In addition, rotational diffusion can be calculated to get a better understanding of system dynamics, especially of cases like in Fig. 4.4, C.

I use thirty realizations with different initial conditions to obtain the averaged anomalous MSD diffusion exponent. This obtained value is characteristic of the size of the system and duration for which the simulation is conducted. Fig. 4.2 shows the effect on the diffusive behaviour of the system due to changes in γ and packing

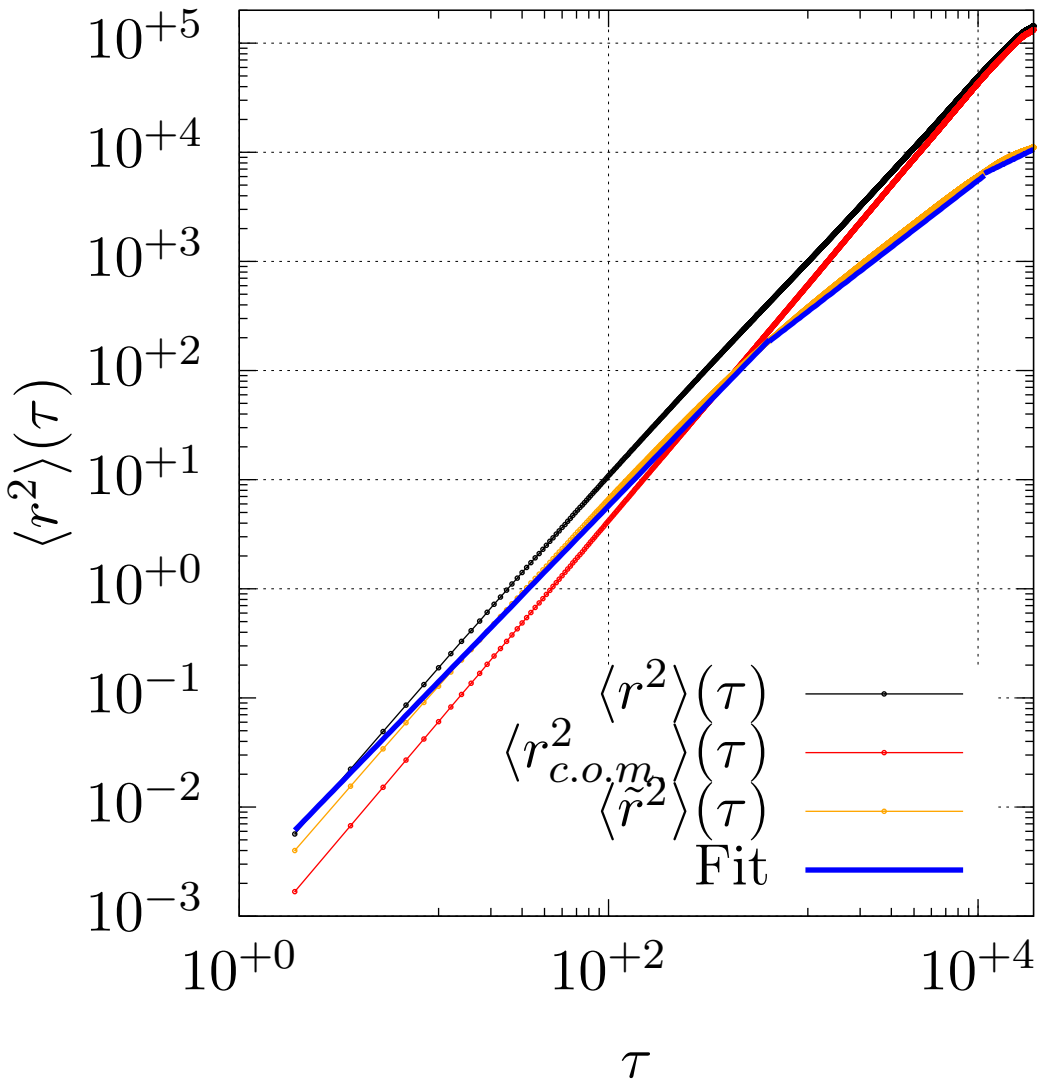

Figure 4.1: Mean squared displacement for a system with packing fraction $\phi = 1.0$, $\kappa = 5.0$ and $\mathcal{F} = 1.0$. r^2 is a measure of total MSD, $r^2_{c.o.m.}$ shows the displacement of the centre of mass, $\tilde{r}^2$ is for adjusted mean squared displacement. The first regime ranges from $\tau = 2$ to $\tau \approx 740$, the second one — up to $\tau \approx 10840$ and the last one covers the rest, almost *half* of the data points despite it being visibly small. The corresponding values of μ are $\approx 1.75, 1.31, 0.83$.

fraction, for the finite sized systems studied here. Running simulations for a longer time (see below) indicates the presence of a long transient behaviour (especially in the case of softly interacting rods). Nevertheless, the results plotted in Fig. 4.2 allow me to usefully correlate the diffusive behaviour of the system with its dynamic properties as observed in animations of the systems. The procedure of approximation

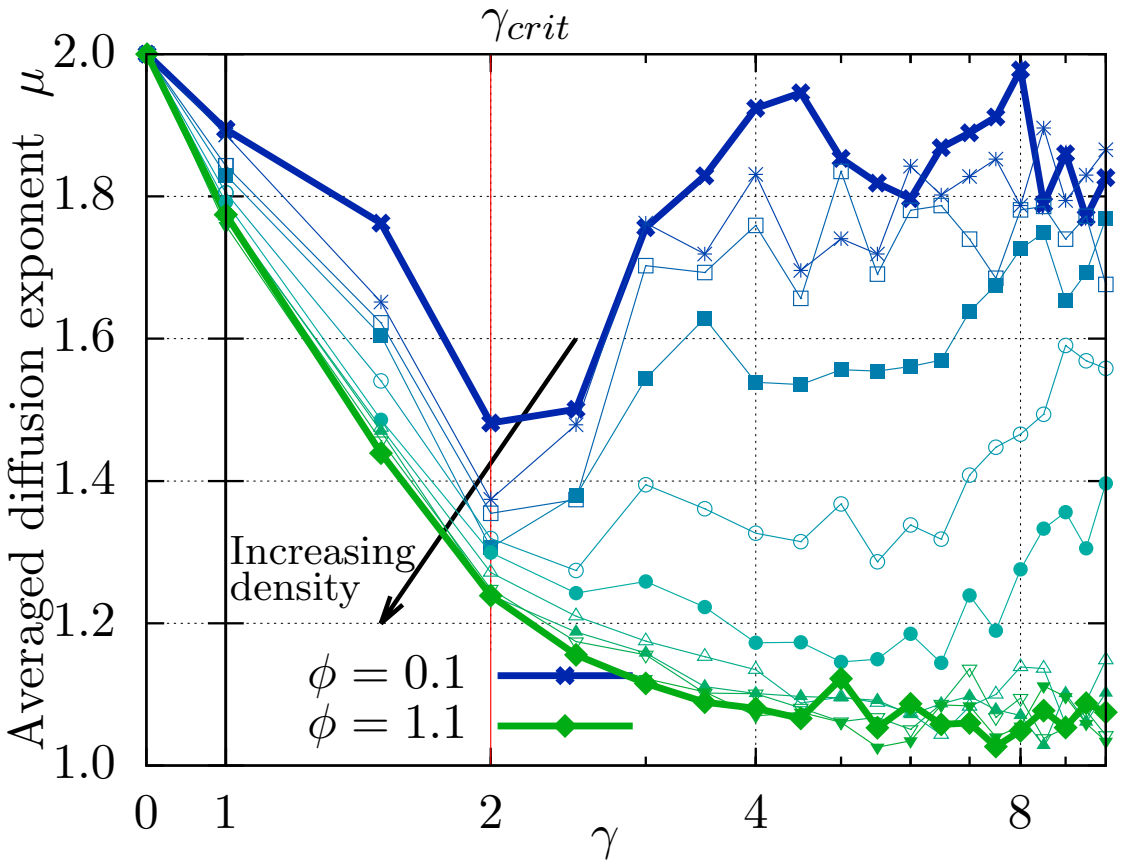

Figure 4.2: MSD exponent μ as a function of γ for various values of packing fraction ϕ. Semi-logarithmic ($\log_{10}$) scale is used on the interval (1,10) to capture different ranges of γ. The arrow denotes systems of increasing density.

itself is simple. I work under the *assumption* that every non-ballistic MSD can be divided into three regions: the initial ballistic regime, a transient region and the final anomalous diffusion. Thus, the logarithm of the MSD can be approximated with a straight line at each scale with the corresponding slope Since there is no clear points where these regimes start and end the best option is to use a piece-wise linear approximation here. That means the data is approximated with piece-wise continuous linear function comprised of three segments. Using the conventional method of least squares for this I extract the exponents μ of the anomalous diffusion. I note that the length of every MSD region *may* vary depending on the parameters of the system, however, for different realisations of the same system these regions stay *roughly* the same. The obtained results are provided in the subsection below.

4.2.2 Results

My finding is that as I increase γ making the system harder (or equivalently decreasing the driving force), collisions start playing a more significant role due to stronger scattering, leading to sub-ballistic behaviour (see Fig 4.2). I see that up to $\gamma_{crit} \approx 2.0$ the change in the averaged anomalous MSD diffusion exponent (i.e. μ) follows the same trend — irrespective of the system density. Beyond γ_{crit} the curves describing the diffusion exponents diverge strongly: sparse systems remain close to ballistic behaviour while dense systems rapidly approach the diffusive regime.

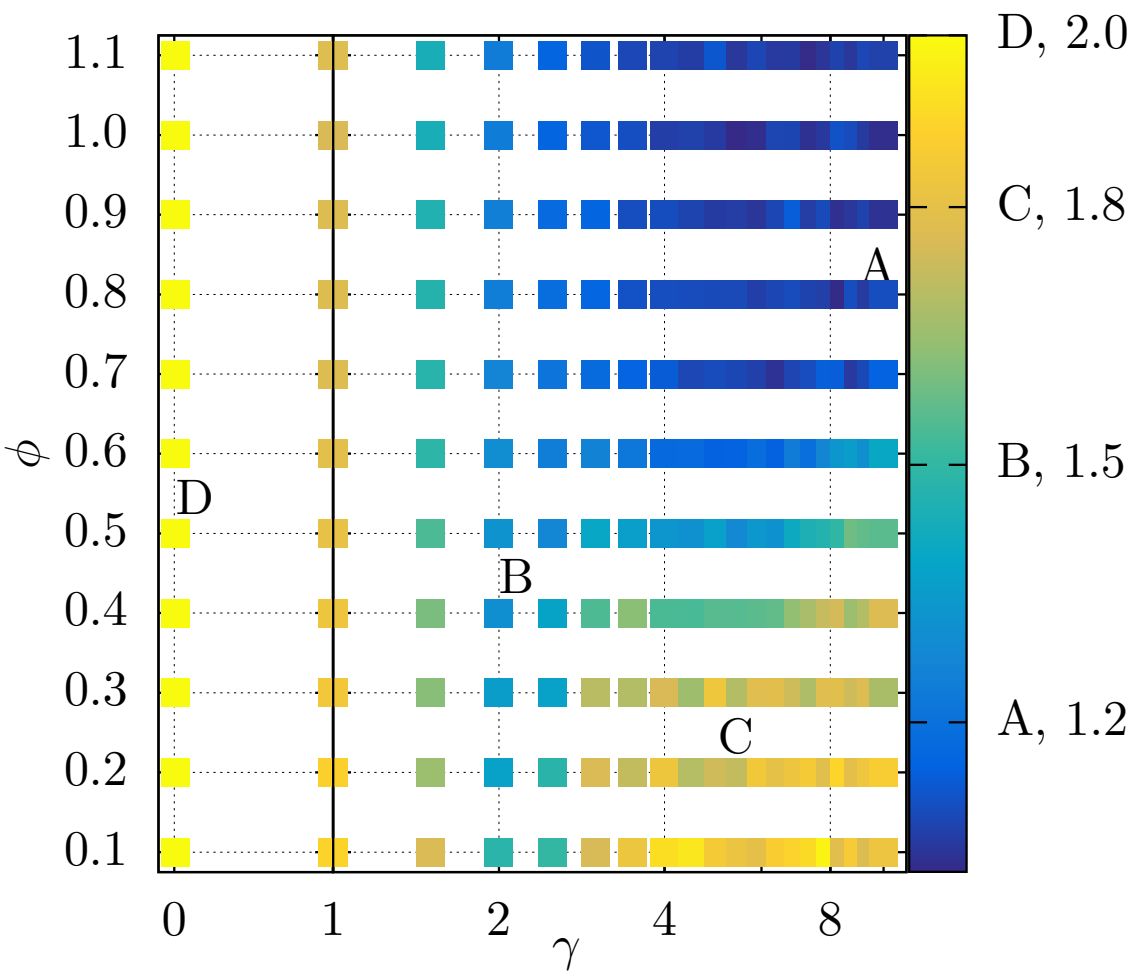

Figure 4.3: Averaged anomalous MSD diffusion exponent μ as a function of γ for various values of packing fraction ϕ represented as a phase diagram. Semi-logarithmic ($\log_{10}$) scale is used on the interval (1,10) to capture different ranges of γ. The colour bar shows the the range of the anomalous diffusion exponent μ.

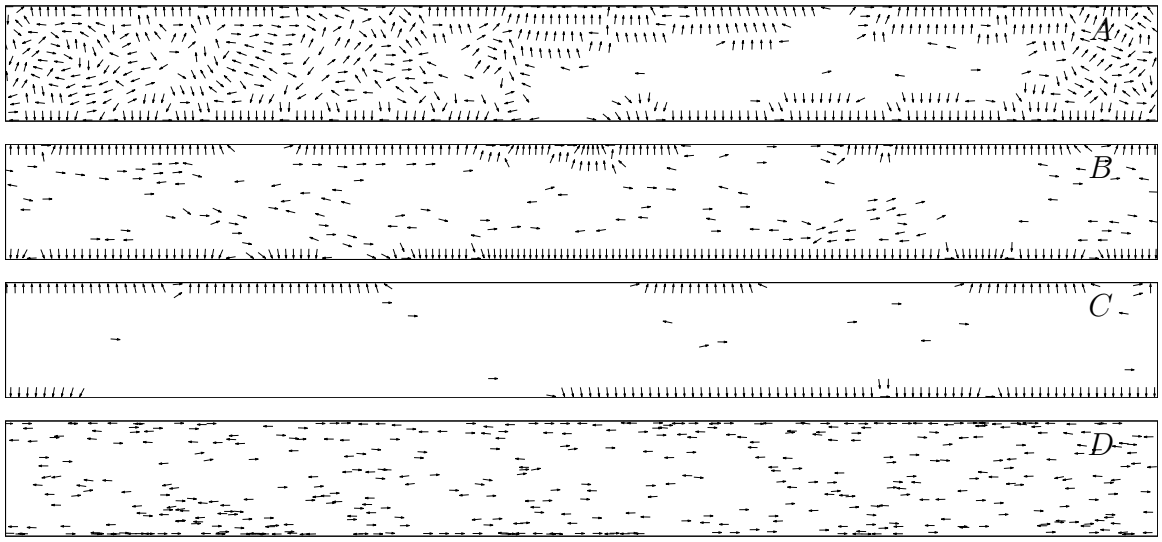

Figure 4.4: Snapshots of different phases: A) $\phi = 0.8, \gamma = 10.0$; B) $\phi = 0.5, \gamma = 2.0$; C) $\phi = 0.2, \gamma = 5.0$; D) $\phi = 0.5, \gamma = 0.01$.

To better understand the various diffusive regimes and their relationship to each other, I present the same data as in Fig. 4.2 in a manner suggestive of a phase diagram (see Fig. 4.3) — here the colour code indicates the magnitude of the anomalous diffusion exponent μ. While I do not observe strong boundaries there are clearly regions which display qualitatively different behaviour. In the following I discuss some of these regimes and give examples.

In the ultra soft regime (i.e. vanishingly small values of γ), I observe behaviour close to purely ballistic for all packing fractions (see Fig 4.3, 4.4 D). In this regime steric interactions are negligible and the rods move almost independently. The result is thin layers of rods running along the walls and parallel streams of particles in the interior.

With increasing γ, region B of the phase diagram (see Fig 4.3) demonstrates the emergence of collective behaviour. The interior is partially depleted of rods with a greater fraction of them now forced against the walls. The rods form giant clusters, which are aligned perpendicular to the wall, moving collectively along the walls as a single entity. This motion is due to the push generated by the small number of rods

trapped within the clusters which are not perfectly perpendicular to the walls. The combined motion of the internal (free moving) rods and the wall clusters leads to the observed super-diffusive motion.

Another interesting region of the phase diagram is when the system contains a low density but with high repulsive force. The rods form stable configurations which are almost perfectly perpendicular to the walls (see Fig 4.3, 4.4: C). Again these wall clusters only move when they contain 'defects', i.e. rods caged within the clusters that are not perpendicular to the walls. However, when a cluster is free of defects, its speed is negligible because of an almost perfect balance of steric, active and boundary forces.

In the last region A, with high densities and hard interactions, active rods form locally aligned boundary layers with a highly disordered interior that is densely populated (see Fig 4.3, 4.4: A), their collective motion is in the super-diffusive regime. Due to the high packing fraction, most rods are restricted to locally aligned boundary layers with little movement. However, I observe giant density fluctuations with sizeable voids in the interior where actively moving rods can still be found. Similar effects with respect to self-propellant force were observed in systems with active Brownian particles and disk-like confinements (see, for example, Ref. [161], Fig. 2).

Finally, I show that the diffusive behaviour of the system continues to evolve for larger systems (obtained by increasing the length of the channel) and at longer times (see Fig. 4.5). I examine a densely packed system (setting packing fraction $\phi = 1.1$) ensuring frequent collisions between rods, which allows me to more easily demonstrate this effect. I consider a soft system ($\gamma = 1.0$) and a hard system ($\gamma = 10.0$). My base dense systems contain ≈ 1000 active rods each. I scale the length of the channels down to $0.25L$ and up to $16L$ resulting in ≈ 250 and ≈ 16000 active rods accordingly. I also examine the effect of increasing the total number of iterations (up to a factor 16). I find that the system evolves extremely slowly with increasing channel length

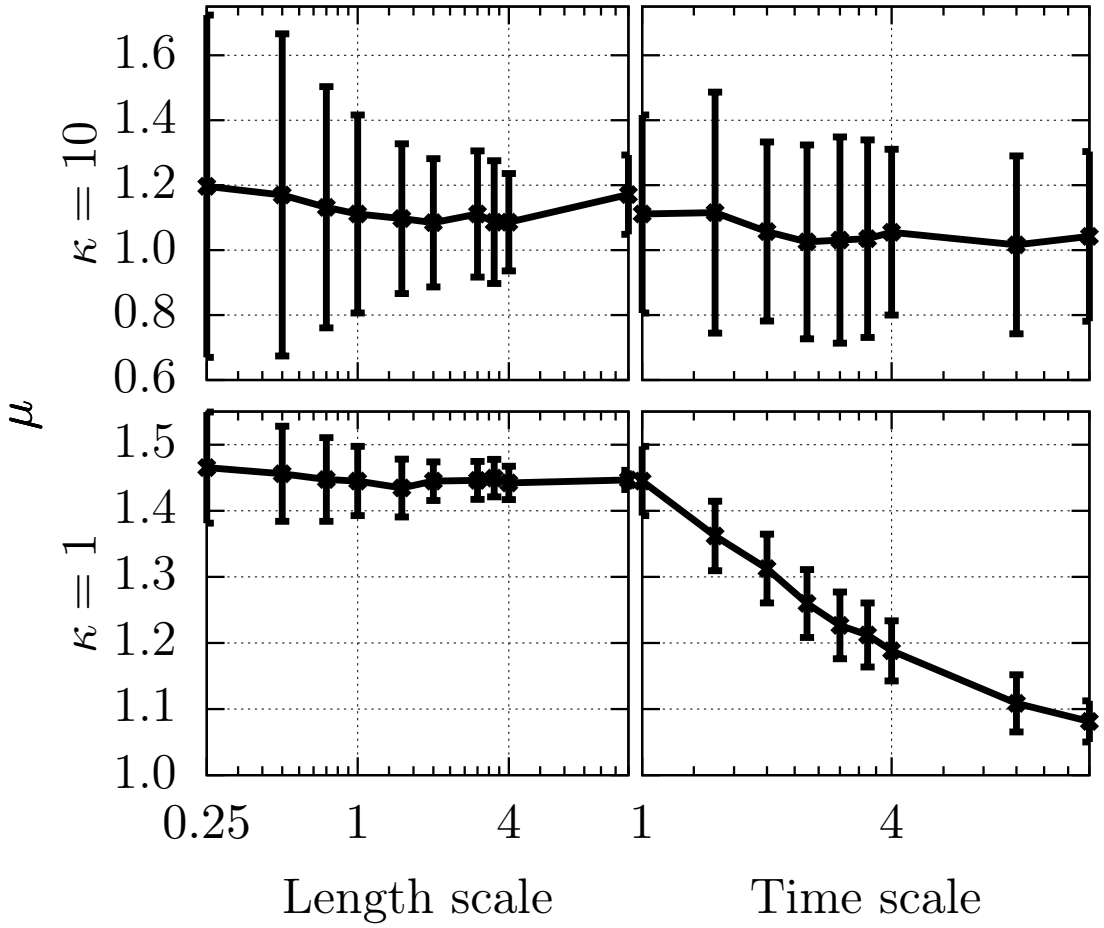

Figure 4.5: The MSD exponent μ at different time and space scales. Data is averaged over 100 different simulations.

(it may be that the narrow width of the channel allows the same diffusive behaviour to persist). However, in the case of soft systems — running the system for longer has a strong effect, indicating that ultimately the system is diffusive i.e. $\mu = 1$. Here I note that there is a difference in values of μ between Fig. 4.3 and Fig. 4.5, bottom left. This is caused by two reasons. First, there is an almost three-fold increase in the number of measurements per point — from 30 to 100. Second and most important here is that this particular area is a transient one between the diffusive and the ballistic one which makes it unclear. Nevertheless, I still conclude that the diagram in Fig. 4.3 can be used as an example of the practical i.e., qualitative behaviour of

the system for any sufficient finite time window.

4.3 Giant density fluctuations

In this section I discuss the results that I obtained from simulations of active rods in narrow periodic channels. In addition, I compare the systems I simulated to similar i.e., active systems, and provide a detailed analysis of the observed difference.

4.3.1 Simulation parameters

Here I re-use the same data that I used in Ch. 3. I also provide additional data from the Sec. 4.2 of this chapter.

4.3.2 Theory

Classical bulk phases like gases or liquids have their densities distributed uniformly. The rigorous mathematical theory behind this says that splitting the domain in d spatial dimensions into boxes of size l results in the average number of particles $\langle n \rangle = \rho l^d$ per box, where ρ is the number density of the system. Assuming that the standard deviation is given as $\Delta n = \sqrt{\langle n^2 \rangle - \langle n \rangle^2}$, it follows from the central limit theorem that in this case for every box the ratio $\Delta n / \sqrt{\langle n \rangle}$ has to stay constant [162, 163]. Whereas density fluctuations — deviations from the average value — are possible, their values are negligible.

On the contrary, active matter exhibit a peculiar behaviour that is called giant density fluctuations (GDF). Experimental observations (see Ref. [162]) as well as computer simulations of active matter (see Ref. [32]) reveal that the standard deviation of density Δn in active matter systems actually grows faster than its mean value $\langle n \rangle$ i.e., $\Delta n \propto n^{\omega}$, where $\omega > 1/2$. The subsection below contains the results that I extracted from simulations of active rods in narrow channels. I also provide a qualitative comparison of my measurements and other similar studies of active matter and discuss the difference.

4.3.3 Results

4.3.3.1 Measurements

First, I start with the procedure of measurements. As mentioned in Ch. 3, all channel have the same geometry i.e., width $W = 12.0$ and length $L = 120.0$. I note that, as I mentioned earlier in Ch. 2 the effective width of the channel is $W_e = 13.0$. That means the actual width of the channel is larger due to the fact that particles can partially penetrate the walls because of their point-like nature. An additional unit of length can noticeably change the values of the metric as I show below. All measurements are taken over 5×10^6 iterations, after the relaxation period is finished. The length of the period is 200 time units as it is explained in Ch. 3.

Earlier publications describing the same phenomena in other active systems do provide quantitative and qualitative results, however, the procedure of the measurements itself is not descriptive enough (see, for instance, Ref. [162]). The most detailed explanation I managed to find in Ref. [162] says that a square sub-domain of a particular size is picked and all deviations are measured over time. It looks like the same steps are applied in both fully confined and unbounded domains as, for example, in references [161] and [3]. However, there is an essential corner case which is missing in this analysis. Boundary effects are extremely important here as I explain below. For example, in Ref. [162] experimental observations of rod-like active particles in a disk-like confinement show no GDF at low packing fractions, whereas in fact this is not true in some cases. A simple example of a similar active system i.e., active rods in a disk-like chamber, that I provide in Fig. 1.5, e) reveals an uneven particle distribution caused by *caging*.

One more thing to deal with is the shape of sub-domains. Since the domain I used in simulations, has a rectangular shape, the maximal size of a square is limited by its width. This limits the scale of observations, another issue is that a lot of data is not used at all, degrading the resulting statistics. Here, I suggest the following procedure

of measurements: for calculations of the number density I pick bins of various size and shape such as squares and rectangles so that the whole domain is covered with identical bins to improve overall statistics. A few examples of systems with high density deviations are provided in Fig. 4.6.

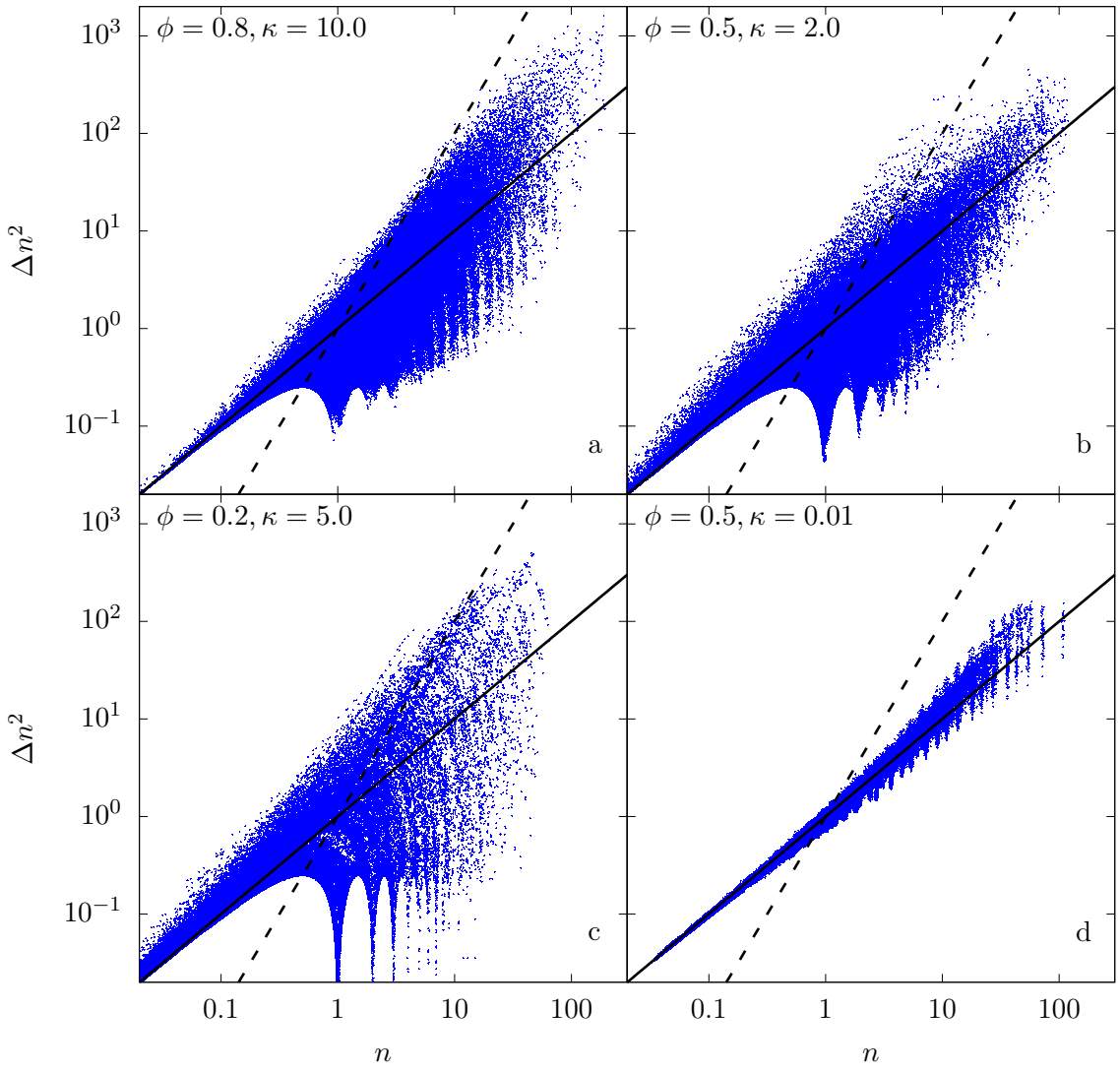

Figure 4.6: a)-d) The squared magnitude of giant density fluctuations against the average number of particles per bin. The solid and the dashed lines mark slopes 1 (ideal gas) and 2 (phase separated) [3], respectively. The results are provided for corresponding systems given in Fig. 4.4. The same binning procedure is applied to every system, the only difference is that systems have different packing fractions ϕ and different values of hardness κ.

The average number of particles per every cell is calculated over all iterations,

measuring GDF in every cell using the conventional formula $\Delta n^2 = \langle n^2 \rangle - \langle n \rangle^2$ is coming next. These values of Δn^2 reveal a fine structure in the obtained data (see, for example, Fig. 4.6, c). From this I infer that a certain fraction of the active rods forms something akin to a (liquid) crystal — that is confirmed by visual observations — resulting in drops in GDF at certain regular scales. Indeed, whereas particles can move as a single entity, their relative motion is sometimes negligible. That means the average number of particles per cell barely changes resulting in extremely small deviations.

I note here that this fine structure disappears when the hardness of active rods is sufficiently small resulting in an active gas. Increasing the packing fraction ϕ also takes its tall as can be see in Fig. 4.6, a since pairwise collisions start to play a more significant role in the systems and partially disrupt the boundary structures.

Strictly speaking, every sub-plot in Fig. 4.6 should have one more point when a bin has the same size as the domain itself. Whereas this point doesn't add anything to the analysis of the systems, it serves as a control value. It is clear than in a system with N particles there is only one bin that completely covers the domain meaning that it also contains $n = N$ particles. This results in zero deviations from the average values [1]. However, due to the logarithmic scale used to plot the data, adding this point is infeasible.

The algorithm has also been tested against a dummy system with *a priori* uniform distribution of particles and packing fraction $\phi = 1.1$. First, the measurements of GDF stay roughly constant in a wide range of scales (see Fig. 4.7), with some observable but minor deviations. These values can be explained by poor statistics i.e., low number of samples. Second, the same Fig. 4.7 shows that averaging of GDF values at the same scale looks like a valid approach.

[1] This value sometimes is not zero but rather $\approx 10^{-3}$ due to numerical errors, however, it doesn't change the overall picture.

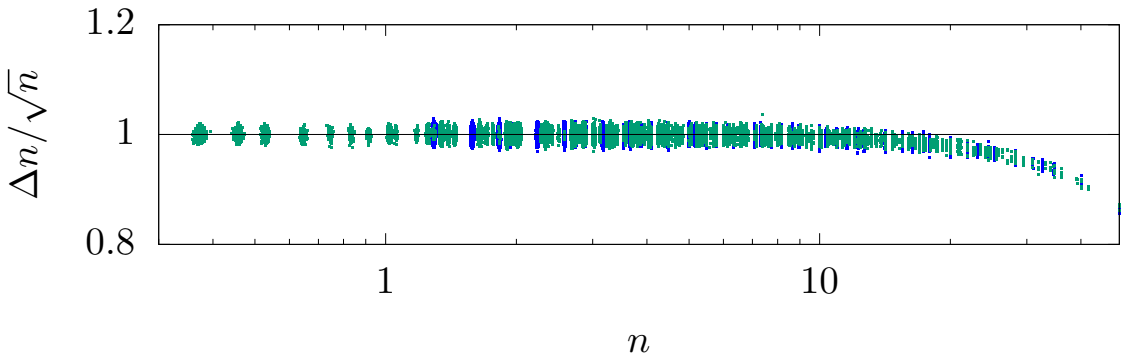

Figure 4.7: Blue dots: GDF measurements in a dummy system assuming that the initial value of width W is used for binning; green dots: the same measurements but based on W_e. The horizontal line corresponds to $\Delta n/\sqrt{n} = 1$.

4.3.3.2 Comparison to other active systems

For starters, I provide a comparative diagram (see Fig. 4.8) below that shows the behaviour of GDF at different packing fractions ϕ in systems with different values of hardness coefficient κ.

A more detailed consideration of all datasets reveals three distinctive scales. First, the deviations at small scales are almost non-existent, $\Delta n \sim \sqrt{n}$. The range of n slightly varies for different values of κ and ϕ, however, it is clear from Fig. 4.8 that for low κ this range is greater, ending at approximately $n \approx 1$.

Next, the deviations start to grow, even at low packing fractions till they reach a saturation point [164]. In terms of calculus, the function reaches its maximum and start to decrease after that. At the same time boundary effects described earlier in this section start to manifest themselves. That result in high and extremely low values of GDF *at the same* scales. Finally, after reaching the maximum, GDF start to decay, since at large scales everything is distributed more uniformly. I note here that the case of $\kappa = 0.01$ is a corner case that is non-biological and given mainly for illustrative purposes. Its behaviour is cardinally different as the deviations are insignificant at all scales and packing fractions.

The resulting behaviour is different compared to other active systems. First, there

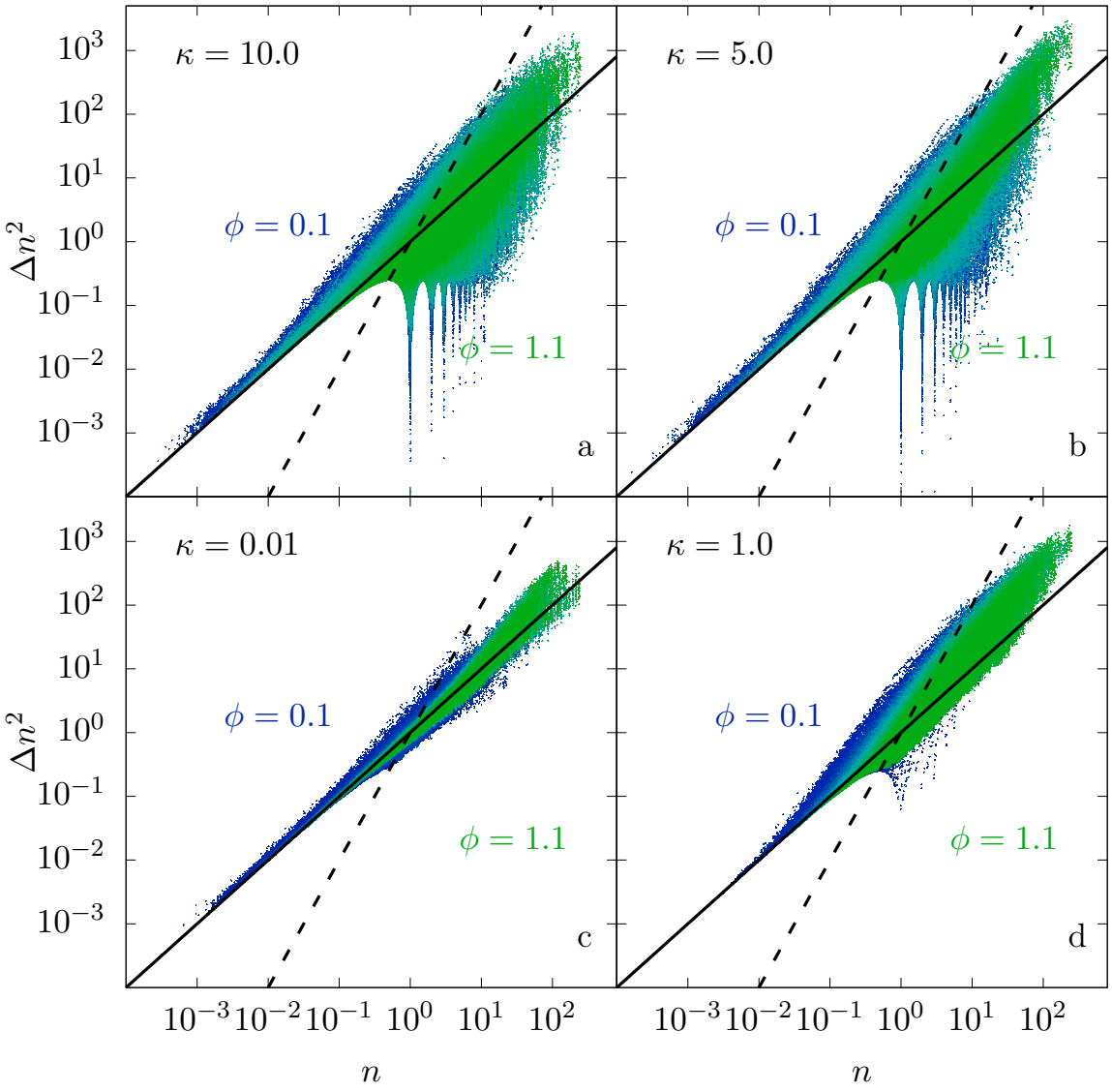

Figure 4.8: a)-d) The squared magnitude of GDF against the mean number of particles, for boxes of different sizes. Blue dots correspond to sparse systems i.e., $\phi = 0.1$ whereas green dots correspond to fully packed systems with $\phi = 1.1$. Values of κ are provided in each figure. The solid and the dashed lines mark slopes 1 (ideal gas) and 2 (phase separated) [3], respectively. The channel is split into $(2, 3, 4, 6, 8, 10, 13, 16, 26)$ strips in y direction and into $(2, 3, 4, 5, 6, 8, 10, 12, 16, 20, 24, 30, 40, 48, 60, 80, 120, 160, 240)$ strips in x direction, resulting in 171 different tilings.

is no distinctive regimes of activity in my systems as opposed to, for example, Ref. [161], where active noisy disks were confined within a disk-like chamber. Authors of this reference observed gas-like fluctuations at low densities, GDF in moderately populated systems and suppressed fluctuations in the jammed phase i.e., in dense

systems. Here, even when there is a hundred or so particles moving in a channel, they form dense clusters in the vicinity of the walls, resulting in GDF. The *caging* effect discussed in Ch. 3 doesn't allow these clusters to decay. My assumption is that adding noise can prevent such behaviour, however, this question is beyond the scope of this chapter. Further increasing of packing fraction ϕ does change the behaviour of the GDF but rather quantitatively than qualitatively. However, Ref. [161] reports that at large packing fractions the systems are completely jammed resulting in suppressed density fluctuations. This is clearly not the case here, nevertheless, I did run additional simulations where the self-propellant force was intentionally switched off. The results of GDF measurements coincide with those in Ref. [161] i.e., the system is jammed. That returns me to Ch. 3 where I discussed the importance of the balance between the active and the steric forces. It seems, that for GDF to completely disappear at large scales active rods have to be extremely hard so that there is almost no overlap between particles resulting in no empty spaces in the channel; the boundary effects in this case are also negligible.

4.4 Conclusions

In this chapter I have studied statistical properties such as MSD and GDF of active rods in periodic channels. I have studied various parameters of the (ϕ, γ) phase space and compared them to those of similar active systems.

Both metrics allow to reveal and categorize the underlying collective behaviour of confined active rods without any visual inspection of the systems themselves. The MSD exponent μ doesn't depend on the size of the system, however, the overall time of observation can be of importance in some cases. Nevertheless, the phase diagram of MSD given in this chapter represents the practical behaviour of the system for any sufficient finite time window. In addition, the results obtained here are qualitatively

similar to those observed in other confined active systems. That means this metric is valid for studying a wide rage of active systems.

The measurements of the GDF reveal relatively stable boundary effects emerging even in systems with soft active rods. Here, it is possible to observe phase separation in sparse systems as particles form meta-stable structures that stay in this state for long times. Further increasing of packing fraction ϕ results in more effective mixing, however, partial phase separation is still observable even in this case.

The following step here is to simulate heterogeneous systems and compare the results to those provided in this chapter. That might further prove the suggestion from Ch. 3 that the system dynamics is governed by the ratio of active and steric forces rather than by their absolute values.

Chapter 5

Conclusions

> Arrakis teaches the attitude of the knife — chopping off what's incomplete and saying: "Now it's complete because it's ended here."
>
> F. Herbert "Dune"

Nowadays, rapid development of computational technologies and numerical techniques allows to simulate large systems of active particles in various confined systems. This, however, doesn't solve other problems that come alongside simulations such as setting proper simulation parameters and further analysis of the results. Whereas advances in biological sciences allow to pick a variety of bacterial strains for detailed studies of microscopic active matter, active matter simulations usually use a simplified (quite often an oversimplified) model that is far from real systems. Moreover, as a relatively modern branch of science that is, in addition, cross-disciplinary it sometimes lacks consistency when in comes to data analysis. Thus, this thesis aims at two main points: correct modelling and correct analysis. As this branch of science continues to develop it requires a set of conventional tools, methods and metrics for general studies of active matter. Here, an attempt was made to do so, so that other people simulating active matter could get consistent results.

Summary

I give a brief introduction to coarse-grained active matter in Ch. 1. That includes the definition of active matter, a variety of simulation approaches that are usually used, a short historical reference and a set of possible applications.

In Ch. 2 I discuss a general approach to computer modelling of dry active matter. Whereas the model itself has been know for decades, the way to simulate active systems with different kinds of heterogeneity is less developed. I give an explanation of how active particles with different softness can interact.

Another point of this chapter is the main algorithm that lies beneath all simulations. Whereas the amount of computational power available to scientists keeps growing allowing to simulate larger systems, a way to improve performance of the algorithms is still important. In this chapter I explain how to incorporate some known techniques to to reduce the overall simulation time. I also provide a novel approach of simulating active systems with different boundaries and — what's more important — a way to do this effectively in terms of computational performance.

Ch. 3 contains the results of simulations of homogeneous & heterogeneous active systems in narrow channels. The main findings are the following: the presence of external walls causes heterogeneous systems to segregate. Active rods that are less motile and less hard are pushed back into the interior of the channel. Despite it being a very idealized case of an active system, it can be useful in simulations of real bacterial communities where properties of bacteria are not given by a single value but rather by a continuous range of values. The simulated system have been tested against similar systems but with longer active rods. The results confirm the initial assumption that such behaviour is intrinsic for such systems and should be observed in a wide range of scales.

Finally, I take a closer look at collective properties of confined active matter in Ch. 4. I consider two main metrics here: the mean square displacement and the giant density fluctuations. Both metrics reveal a few distinctive motion patterns that

naturally emerge in confined active systems. This allows to analyse the dynamics without direct observations of active systems.

Future work

The area of active matter is vast to say the least. It spans from simulations of interactions between a few individuals to simulations of bacterial communities comprised of dozens of thousands of single bacteria. However, it still requires a lot of work to be done in order to get a better understanding of underlying processes in active systems. Further steps here, I hope, are the following:

- to develop a general approach to simulations of real active communities if not a single computational package. Since many active systems can be described by the same or similar equations, that looks like a doable task. Whereas there are computer programs that allow to simulate active matter, they are of general purpose and the details of simulations are often lie beneath layers of abstraction making understanding and/or modification complicated.

- a lot of metrics that are used in the analysis of active matter are sometimes used once and get abandoned. Finding a publication 10 years later and trying to get similar results sometimes is impossible due to that. From that I can infer that there is a need for a set of conventional tools with a detailed description of how they work. That would allow to get consistent results even when the original research is for some reason out of reach.

- development of the existing code allowing it to contain various implementations of different boundary conditions and confinement topologies. That would allow to simulate more realistic systems such as microfludic chips. These are widely used in active matter studies and often have complex geometries and topologies.

Bibliography

[1] Vladimir Khodygo, Martin T. Swain, and Adil Mughal. Homogeneous and heterogeneous populations of active rods in two-dimensional channels. *Phys. Rev. E*, 99(2): 022602, feb 2019. ISSN 2470-0045.

[2] William Mattson and Betsy M. Rice. Near-neighbor calculations using a modified cell-linked list method. *Comput. Phys. Commun.*, 119(2-3):135–148, jun 1999. ISSN 00104655.

[3] Yaouen Fily, Silke Henkes, and M. Cristina Marchetti. Freezing and phase separation of self-propelled disks. *Soft Matter*, 10(13):2132–2140, sep 2013. ISSN 1744-683X.

[4] Alexandre P Solon, Y Fily, A Baskaran, M E Cates, Y Kafri, M Kardar, and J Tailleur. Pressure is not a state function for generic active fluids. *Nat. Phys.*, 11(August):1–7, 2015. ISSN 1745-2473.

[5] Sriram Ramaswamy. The mechanics and statistics of active matter. *Annu. Rev. Condens. Matter Phys.*, 1(1):323–345, 2010. ISSN 1947-5454.

[6] Craig W. Reynolds. Flocks, herds and schools: A distributed behavioral model. *ACM SIGGRAPH Comput. Graph.*, 21(4):25–34, 1987. ISSN 00978930.

[7] R D Alexander. The Evolution of Social Behavior. *Annu. Rev. Ecol. Syst.*, 5(1): 325–383, nov 1974. ISSN 0066-4162.

[8] H. Ronald Pulliam and Thomas B. Caraco. Living in groups: Is there an optimal group size? In Nicholas B. Davies and John R. Krebs, editors, *Behav. Ecol.*, pages 122–147. Blackwell, Oxford, 2nd edition, 1984.

[9] Mary C. Hager and Gene S. Helfman. Safety in numbers: shoal size choice by minnows under predatory threat. *Behav. Ecol. Sociobiol.*, 29(4):271–276, nov 1991. ISSN 0340-5443.

[10] Paul A. Schmidt and L. David Mech. Wolf Pack Size And Food Acquisition. *Am. Nat.*, 150(4):513–517, oct 1997. ISSN 0003-0147.

[11] M. Ballerini, N. Cabibbo, R. Candelier, A. Cavagna, E. Cisbani, I. Giardina, V. Lecomte, A. Orlandi, G. Parisi, A. Procaccini, M. Viale, and V. Zdravkovic. Interaction ruling animal collective behavior depends on topological rather than metric distance: Evidence from a field study. *Proc. Natl. Acad. Sci.*, 105(4):1232–1237, jan 2008. ISSN 0027-8424.

[12] Anton Peshkov, Sandrine Ngo, Eric Bertin, Hugues Chaté, and Francesco Ginelli. Continuous Theory of Active Matter Systems with Metric-Free Interactions. *Phys. Rev. Lett.*, 109(9):098101, aug 2012. ISSN 0031-9007.

[13] Dennis J. Evangelista, Dylan D. Ray, Sathish K. Raja, and Tyson L. Hedrick. Three-dimensional trajectories and network analyses of group behaviour within chimney swift flocks during approaches to the roost. *Proc. R. Soc. B Biol. Sci.*, 284(1849): 20162602, feb 2017. ISSN 0962-8452.

[14] Pulak K Ghosh, Peter Hänggi, Fabio Marchesoni, and Franco Nori. Giant negative mobility of Janus particles in a corrugated channel. *Phys. Rev. E*, 89(6):062115, jun 2014. ISSN 1539-3755.

[15] A M Menzel. Unidirectional laning and migrating cluster crystals in confined self-propelled particle systems. *J. Phys. Condens. Matter*, 25(50):505103, dec 2013. ISSN 0953-8984.

[16] H. H. Wensink, V. Kantsler, R. E. Goldstein, and J. Dunkel. Controlling active self-assembly through broken particle-shape symmetry. *Phys. Rev. E - Stat. Nonlinear, Soft Matter Phys.*, 89(1):1–5, 2014. ISSN 15393755.

[17] Che-ming J Hu, Ronnie H Fang, Kuei-chun Wang, Brian T Luk, Soracha Thamphiwatana, Diana Dehaini, Phu Nguyen, Pavimol Angsantikul, Cindy H Wen, Ashley V Kroll, Cody Carpenter, Manikantan Ramesh, Vivian Qu, Sherrina H Patel, Jie Zhu, William Shi, Florence M Hofman, Thomas C Chen, Weiwei Gao, Kang Zhang, Shu Chien, and Liangfang Zhang. Nanoparticle biointerfacing by platelet membrane cloaking. *Nature*, 526(7571):118–121, sep 2015. ISSN 0028-0836.

[18] Sepideh Bazazi, Jerome Buhl, Joseph J. Hale, Michael L. Anstey, Gregory A. Sword, Stephen J. Simpson, and Iain D. Couzin. Collective Motion and Cannibalism in Locust Migratory Bands. *Curr. Biol.*, 18(10):735–739, may 2008. ISSN 09609822.

[19] J. Buhl, D. J. T. Sumpter, I. D. Couzin, J. J. Hale, E. Despland, E. R. Miller, and S. J. Simpson. From Disorder to Order in Marching Locusts. *Science (80-.).*, 312 (5778):1402–1406, jun 2006. ISSN 0036-8075.

[20] D.M. Hunter, L. McCulloch, and P.A. Spurgin. Aerial detection of nymphal bands of the Australian plague locust (Chortoicetes terminifera (Walker)) (Orthoptera: Acrididae). *Crop Prot.*, 27(1):118–123, jan 2008. ISSN 02612194.

[21] Arianna Bottinelli, David T. J. Sumpter, and Jesse L Silverberg. Emergent Structural Mechanisms for High-Density Collective Motion Inspired by Human Crowds. *Phys. Rev. Lett.*, 117(22):228301, nov 2016. ISSN 0031-9007.

[22] Jesse L. Silverberg, Matthew Bierbaum, James P. Sethna, and Itai Cohen. Collective Motion of Humans in Mosh and Circle Pits at Heavy Metal Concerts. *Phys. Rev. Lett.*, 110(22):228701, may 2013. ISSN 0031-9007.

[23] Ioannis Karamouzas, Brian Skinner, and Stephen J. Guy. Universal power law governing pedestrian interactions. *Phys. Rev. Lett.*, 113(23):238701, dec 2014. ISSN 0031-9007.

[24] Jaeyoung Kwak, Hang Hyun Jo, Tapio Luttinen, and Iisakki Kosonen. Collective dynamics of pedestrians interacting with attractions. *Phys. Rev. E - Stat. Nonlinear, Soft Matter Phys.*, 88(6):1–6, 2013. ISSN 15393755.

[25] C. Reichhardt and C. J. Olson Reichhardt. Aspects of jamming in two-dimensional athermal frictionless systems. *Soft Matter*, 10(17):2932, 2014. ISSN 1744-683X.

[26] Daniel B. Kearns. A field guide to bacterial swarming motility. *Nat. Rev. Microbiol.*, 8(9):634–644, sep 2010. ISSN 1740-1526.

[27] J Henrichsen. Bacterial surface translocation: a survey and a classification. *Bacteriol. Rev.*, 36(4):478–503, dec 1972. ISSN 0005-3678.

[28] Marco G. Mazza. The physics of biofilms—an introduction. *J. Phys. D. Appl. Phys.*, 49(20):203001, may 2016. ISSN 0022-3727.

[29] Joost de Graaf, Henri Menke, Arnold J T M Mathijssen, Marc Fabritius, Christian Holm, and Tyler N Shendruk. Lattice-Boltzmann hydrodynamics of anisotropic active matter. *J. Chem. Phys.*, 144(13):134106, apr 2016. ISSN 0021-9606.

[30] Saverio E. Spagnolie and Eric Lauga. Hydrodynamics of self-propulsion near a boundary: predictions and accuracy of far-field approximations. *J. Fluid Mech.*, 700:105–147, 2012. ISSN 0022-1120.

[31] Jinglei Hu, Mingcheng Yang, Gerhard Gompper, and Roland G Winkler. Modelling the mechanics and hydrodynamics of swimming E. coli. *Soft Matter*, 11(40):7867–7876, 2015. ISSN 1744-683X.

[32] H. H. Wensink and H. Löwen. Aggregation of self-propelled colloidal rods near confining walls. *Phys. Rev. E*, 78(3):031409, sep 2008. ISSN 1539-3755.

[33] Amin Doostmohammadi, Michael F. Adamer, Sumesh P. Thampi, and Julia M. Yeomans. Stabilization of active matter by flow-vortex lattices and defect ordering. *Nat. Commun.*, 7(1):10557, apr 2016. ISSN 2041-1723.

[34] Hugo Wioland, Enkeleida Lushi, and Raymond E. Goldstein. Directed collective motion of bacteria under channel confinement. *New J. Phys.*, 18(7):075002, jul 2016. ISSN 1367-2630.

[35] Gaetano Napoli and Luigi Vergori. Hydrodynamic theory for nematic shells: the interplay among curvature, flow and alignment. *Phys. Rev. E*, 94(2):020701, aug 2016. ISSN 2470-0045.

[36] C.J. Olson Reichhardt and C. Reichhardt. Ratchet Effects in Active Matter Systems. *Annu. Rev. Condens. Matter Phys.*, 8(1):51–75, mar 2017. ISSN 1947-5454.

[37] Nikolai Nikola, Alexandre P. Solon, Yariv Kafri, Mehran Kardar, Julien Tailleur, and Raphaël Voituriez. Active particles on curved surfaces: Equation of state, ratchets, and instabilities. *Arxiv*, 098001(1):1–5, 2015. ISSN 0031-9007.

[38] A Pototsky, A M Hahn, and H Stark. Rectification of self-propelled particles by symmetric barriers. *Phys. Rev. E*, 87(4):042124, apr 2013. ISSN 1539-3755.

[39] Alejandro V. Silhanek. From vortex ratchets to rectification of self-propelled swimmers, 2014.

[40] Andreas Kaiser, Andrey Sokolov, Igor S. Aranson, and Hartmut Lowen. Mechanisms of Carrier Transport Induced by a Microswimmer Bath. *IEEE Trans. Nanobioscience*, 14(3):260–266, apr 2015. ISSN 1536-1241.

[41] Jens Elgeti and Gerhard Gompper. Wall accumulation of self-propelled spheres. *EPL (Europhysics Lett.*, 101(4):48003, 2013. ISSN 0295-5075, 1286-4854.

[42] Sven van Teeffelen, Urs Zimmermann, and Hartmut Löwen. Clockwise-directional circle swimmer moves counter-clockwise in Petri dish- and ring-like confinements. *Soft Matter*, 5(22):4510, 2009. ISSN 1744-683X.

[43] András Czirók, Eshel Ben-Jacob, Inon Cohen, and Tamás Vicsek. Formation of complex bacterial colonies via self-generated vortices. *Phys. Rev. E*, 54(2):1791–1801, 1996. ISSN 1063-651X.

[44] Hugo Wioland, Francis G Woodhouse, Jörn Dunkel, John O Kessler, and Raymond E Goldstein. Confinement Stabilizes a Bacterial Suspension into a Spiral Vortex. *Phys. Rev. Lett.*, 110(26):268102, jun 2013. ISSN 0031-9007.

[45] Chiu Fan Lee. Active particles under confinement: Aggregation at the wall and gradient formation inside a channel. *New J. Phys.*, 15, 2013. ISSN 13672630.

[46] Joost de Graaf, Arnold J. T. M. Mathijssen, Marc Fabritius, Henri Menke, Christian Holm, and Tyler N. Shendruk. Understanding the onset of oscillatory swimming in microchannels. *Soft Matter*, 12(21):4704–4708, 2016. ISSN 1744-683X.

[47] Yaouen Fily, Aparna Baskaran, and Michael F. Hagan. Dynamics and density distribution of strongly confined noninteracting nonaligning self-propelled particles in a nonconvex boundary. *Phys. Rev. E - Stat. Nonlinear, Soft Matter Phys.*, 91(1):1–11, 2015. ISSN 15502376.

[48] Frank Smallenburg and Hartmut Löwen. Swim pressure on walls with curves and corners. *Phys. Rev. E - Stat. Nonlinear, Soft Matter Phys.*, 92(3):032304, sep 2015. ISSN 15502376.

[49] D. Reguera and J. M. Rubi. Engineering tube shapes to control confined transport. *Eur. Phys. J. Spec. Top.*, 223(14):3079–3093, 2014. ISSN 19516401.

[50] Christian Kreuter, Ullrich Siems, Peter Henseler, Peter Nielaba, Paul Leiderer, and Artur Erbe. Stochastic transport of particles across single barriers. *J. Phys. Condens. Matter*, 24(46):464120, 2012. ISSN 0953-8984.

[51] Aloke Kumar, David Karig, Rajesh Acharya, Suresh Neethirajan, Partha P. Mukherjee, Scott Retterer, and Mitchel J. Doktycz. Microscale confinement features can affect biofilm formation. *Microfluid. Nanofluidics*, 14(5):895–902, 2013. ISSN 16134982.

[52] Jian-chun Wu and Bao-quan Ai. Forced transport of self-propelled particles in a two-dimensional separate channel. *Sci. Rep.*, 6(April):24001, 2016. ISSN 2045-2322.

[53] Andrea Costanzo, Jens Elgeti, Thorsten Auth, Gerhard Gompper, and Marisol Ripoll. Motility-sorting of self-propelled particles in microchannels. *EPL (Europhysics Lett.*, 107(3):36003, aug 2014. ISSN 0295-5075.

[54] Tamás Vicsek, András Czirók, Eshel Ben-Jacob, Inon Cohen, and Ofer Shochet. Novel Type of Phase Transition in a System of Self-Driven Particles. *Phys. Rev. Lett.*, 75 (6):1226–1229, aug 1995. ISSN 0031-9007.

[55] H H Wensink and H Löwen. Emergent states in dense systems of active rods: from swarming to turbulence. *J. Phys. Condens. Matter*, 24(46):464130, apr 2012. ISSN 0953-8984.

[56] Samuel R. McCandlish, Aparna Baskaran, and Michael F. Hagan. Spontaneous segregation of self-propelled particles with different motilities. *Soft Matter*, 8(8):2527, 2012. ISSN 1744-683X.

[57] Yuhai Tu and John Toner. How birds fly together: Long-range order in a two-dimensional dynamical XY model. *Phys. Rev. Lett.*, 75(23):4326–4329, jun 1995. ISSN 0031-9007.

[58] Hugo Wioland. *Self-Organisation of Confined Active Matter*. PhD thesis, University of Cambridge, 2014.

[59] Thomas Ihle. Towards a quantitative kinetic theory of polar active matter. *Eur. Phys. J. Spec. Top.*, 223(7):1293–1314, jan 2014. ISSN 1951-6355.

[60] Francesco Ginelli, Fernando Peruani, Markus Bär, and Hugues Chaté. Large-scale collective properties of self-propelled rods. *Phys. Rev. Lett.*, 104(18):1–4, 2010. ISSN 00319007.

[61] Liesbeth M. C. Janssen, Andreas Kaiser, and Hartmut Löwen. Aging and rejuvenation of active matter under topological constraints. *Sci. Rep.*, 7(1):5667, dec 2017. ISSN 2045-2322.

[62] H. H. Wensink, J. Dunkel, S. Heidenreich, K. Drescher, R. E. Goldstein, H. Lowen, and J. M. Yeomans. Meso-scale turbulence in living fluids. *Proc. Natl. Acad. Sci.*, 109(36):14308–14313, sep 2012. ISSN 0027-8424.

[63] Luis H. Cisneros, Ricardo Cortez, Christopher Dombrowski, Raymond E. Goldstein, and John O. Kessler. Fluid dynamics of self-propelled microorganisms, from individuals to concentrated populations. In *Anim. Locomot.*, pages 99–115. Springer Berlin Heidelberg, Berlin, Heidelberg, 2010. ISBN 9783642116322.

[64] Enkeleida Lushi, Hugo Wioland, and Raymond E Goldstein. Fluid flows created by swimming bacteria drive self-organization in confined suspensions. *Proc. Natl. Acad. Sci. U. S. A.*, 111(27):9733–9738, 2014. ISSN 1091-6490.

[65] Maxime Theillard, Roberto Alonso-Matilla, and David Saintillan. Geometric control of active collective motion. *Soft Matter*, 13(2):363–375, aug 2016. ISSN 1744-683X.

[66] H. Chaté, F. Ginelli, G. Grégoire, F. Peruani, and F. Raynaud. Modeling collective motion: variations on the Vicsek model. *Eur. Phys. J. B*, 64(3-4):451–456, aug 2008. ISSN 1434-6028.

[67] Volker Schaller, Christoph Weber, Christine Semmrich, Erwin Frey, and Andreas R Bausch. Polar patterns of driven filaments. *Nature*, 467(7311):73–77, 2010. ISSN 1476-4687.

[68] Fernando Peruani, Francesco Ginelli, Markus Bar, and Hugues Chate. Polar vs. apolar alignment in systems of polar self-propelled particles. *J. Phys. Conf. Ser.*, 297:012014, feb 2013. ISSN 1742-6596.

[69] Anton Peshkov, Igor S. Aranson, Eric Bertin, Hugues Chaté, and Francesco Ginelli. Nonlinear Field Equations for Aligning Self-Propelled Rods. *Phys. Rev. Lett.*, 109 (26):268701, dec 2012. ISSN 0031-9007.

[70] Sadato Yamanaka and Takao Ohta. Collision dynamics of traveling bands in systems of deformable self-propelled particles. *Phys. Rev. E*, 90(4):042927, oct 2014. ISSN 1539-3755.

[71] Tong Gao, Meredith D. Betterton, An-Sheng Jhang, and Michael J. Shelley. Analytical structure, dynamics, and coarse-graining of a kinetic model of an active fluid. *Phys. Rev. Fluids*, 2(9):093302, mar 2017. ISSN 2469-990X.

[72] Tyler N. Shendruk, Amin Doostmohammadi, Kristian Thijssen, and Julia M. Yeomans. Dancing disclinations in confined active nematics. *Soft Matter*, 13(21):3853–3862, 2017. ISSN 1744-683X.

[73] Kevin Doxzen, Sri Ram Krishna Vedula, Man Chun Leong, Hiroaki Hirata, Nir S. Gov, Alexandre J. Kabla, Benoit Ladoux, and Chwee Teck Lim. Guidance of collective cell migration by substrate geometry. *Integr. Biol.*, 5(8):1026, 2013. ISSN 1757-9694.

[74] Antoine Bricard, Jean-Baptiste Caussin, Debasish Das, Charles Savoie, Vijayakumar Chikkadi, Kyohei Shitara, Oleksandr Chepizhko, Fernando Peruani, David Saintillan, and Denis Bartolo. Emergent vortices in populations of colloidal rollers. *Nat. Commun.*, 6(May):7470, 2015. ISSN 2041-1723.

[75] Herbert Levine, Wouter-jan Rappel, and Inon Cohen. Self-organization in systems of self-propelled particles. *Phys. Rev. E*, 63(1):017101, 2000. ISSN 1063-651X.

[76] Hanshuang Chen and Zhonghuai Hou. Noise-induced vortex reversal of self-propelled particles. *Phys. Rev. E - Stat. Nonlinear, Soft Matter Phys.*, 86(4):2–7, 2012. ISSN 15393755.

[77] Yutaka Sumino, Ken H. Nagai, Yuji Shitaka, Dan Tanaka, Kenichi Yoshikawa, Hugues Chaté, and Kazuhiro Oiwa. Large-scale vortex lattice emerging from collectively moving microtubules. *Nature*, 483(7390):448–452, 2012. ISSN 0028-0836.

[78] Yao-Li Chuang, Tom Chou, Maria R. D'Orsogna, Yao-Li Chuang, Tom Chou, and Maria R. D'Orsogna. Swarming in viscous fluids: Three-dimensional patterns in swimmer- and force-induced flows. *Phys. Rev. E*, 93(4):043112, apr 2016. ISSN 2470-0045.

[79] Justas Dauparas and Eric Lauga. Flagellar flows around bacterial swarms. *Phys. Rev. Fluids*, 1(4):043202, aug 2016. ISSN 2469-990X.

[80] Amin Doostmohammadi and Julia M. Yeomans. Coherent motion of dense active matter. *Eur. Phys. J. Spec. Top.*, 227(17):2401–2411, mar 2019. ISSN 1951-6355.

[81] Nguyen H P Nguyen, Eric Jankowski, and Sharon C Glotzer. Thermal and athermal three-dimensional swarms of self-propelled particles. *Phys. Rev. E*, 86(1):011136, jul 2012. ISSN 1539-3755.

[82] David Saintillan and Michael J. Shelley. Orientational order and instabilities in suspensions of self-locomoting rods. *Phys. Rev. Lett.*, 99(5):1–4, 2007. ISSN 00319007.

[83] Luca Giomi. Geometry and topology of Turbulence in active nematics. *Phys. Rev. X*, 5(3):1–11, 2015. ISSN 21603308.

[84] Yingzi Yang, Feng Qiu, and Gerhard Gompper. Self-organized vortices of circling self-propelled particles and curved active flagella. *Phys. Rev. E*, 89(1):012720, jan 2014. ISSN 1539-3755.

[85] Antonio Suma, Giuseppe Gonnella, Davide Marenduzzo, and E. Orlandini. Motility-induced phase separation in an active dumbbell fluid. *EPL (Europhysics Lett.*, 108 (5):56004, dec 2014. ISSN 0295-5075.

[86] I. H. Riedel. A Self-Organized Vortex Array of Hydrodynamically Entrained Sperm Cells. *Science (80-.).*, 309(5732):300–303, jul 2005. ISSN 0036-8075.

[87] Ken H. Nagai, Yutaka Sumino, Raul Montagne, Igor S. Aranson, and Hugues Chaté. Collective Motion of Self-Propelled Particles with Memory. *Phys. Rev. Lett.*, 114(16): 168001, apr 2015. ISSN 0031-9007.

[88] Daiki Nishiguchi, Igor S Aranson, Alexey Snezhko, and Andrey Sokolov. Engineering bacterial vortex lattice via direct laser lithography. *Nat. Commun.*, 9(1):4486, dec 2018. ISSN 2041-1723.

[89] Hugo Wioland, Francis G. Woodhouse, Jörn Dunkel, and Raymond E. Goldstein. Ferromagnetic and antiferromagnetic order in bacterial vortex lattices. *Nat. Phys.*, 12(4):341–345, jan 2016. ISSN 1745-2473.

[90] Leonardo Apaza and Mario Sandoval. Active matter on Riemannian manifolds. *Soft Matter*, 14(48):9928–9936, 2018. ISSN 1744-683X.

[91] Rastko Sknepnek and Silke Henkes. Active swarms on a sphere. *Phys. Rev. E - Stat. Nonlinear, Soft Matter Phys.*, 91(2):1–15, 2015. ISSN 15502376.

[92] Murray Eisenberg and Robert Guy. A Proof of the Hairy Ball Theorem. *Am. Math. Mon.*, 86(7):571, aug 1979. ISSN 00029890.

[93] Maria R D Orsogna, Yao-li Chuang, Andrea L Bertozzi, and Lincoln S Chayes. Self-Propelled Particles with Soft-Core Interactions : Patterns , Stability , and Collapse. *Phys. Rev. Lett.*, 104302(March):104302, 2006.

[94] Arshad Kudrolli, Geoffroy Lumay, Dmitri Volfson, and Lev S. Tsimring. Swarming and Swirling in Self-Propelled Polar Granular Rods. *Phys. Rev. Lett.*, 100(5):058001, feb 2008. ISSN 0031-9007.

[95] Hamid Seyed-Allaei and Mohammad Reza Ejtehadi. Vortex with fourfold defect lines in a simple model of self-propelled particles. *Phys. Rev. E*, 93(3):032113, mar 2016. ISSN 2470-0045.

[96] Jean-Baptiste Caussin and Denis Bartolo. Braiding a flock: winding statistics of interacting flying spins. *Phys. Rev. Lett.*, 114(25):258101, jan 2015. ISSN 0031-9007.

[97] Juan P. Hernandez-Ortiz, Christopher G. Stoltz, and Michael D. Graham. Transport and collective dynamics in suspensions of confined swimming particles. *Phys. Rev. Lett.*, 95(20):1–4, 2005. ISSN 00319007.

[98] Juan P Hernandez-Ortiz, Patrick T Underhill, and Michael D Graham. Dynamics of confined suspensions of swimming particles. *J. Phys. Condens. Matter*, 21(20): 204107, 2009. ISSN 0953-8984.

[99] A Costanzo, R Di Leonardo, G Ruocco, and L Angelani. Transport of self-propelling bacteria in micro-channel flow. *J. Phys. Condens. Matter*, 24(6):065101, feb 2012. ISSN 0953-8984.

[100] Xingbo Yang, M Lisa Manning, and M Cristina Marchetti. Aggregation and segregation of confined active particles. *Soft Matter*, 10(34):6477–6484, 2014. ISSN 1744-6848.

[101] A. D. Borba, J. L. C. Domingos, E. C. B. Moraes, F. Q. Potiguar, and W. P. Ferreira. Controlling the transport of active matter in disorderd lattices of asymmetrical obstacles. aug 2019.

[102] Aidan T. Brown, Ioana D. Vladescu, Angela Dawson, Teun Vissers, Jana Schwarz-Linek, Juho S. Lintuvuori, and Wilson C K Poon. Swimming in a crystal. *Soft Matter*, 12(1):131–140, 2016. ISSN 1744-683X.

[103] Hamidreza Khalilian and Hossein Fazli. Obstruction enhances the diffusivity of self-propelled rod-like particles. *J. Chem. Phys.*, 145(16):164909, oct 2016. ISSN 0021-9606.

[104] Stefan H. Holm, Jason P. Beech, Michael P. Barrett, and Jonas O. Tegenfeldt. Separation of parasites from human blood using deterministic lateral displacement. *Lab Chip*, 11(7):1326, 2011. ISSN 1473-0197.

[105] Shashi Ranjan, Kerwin Kwek Zeming, Roland Jureen, Dale Fisher, and Yong Zhang. DLD pillar shape design for efficient separation of spherical and non-spherical bioparticles. *Lab Chip*, 14(21):4250–4262, sep 2014. ISSN 1473-0197.

[106] Hiromasa Okano, Tomoki Konishi, Toshihiro Suzuki, Takahiro Suzuki, Shinya Ariyasu, Shin Aoki, Ryo Abe, and Masanori Hayase. Enrichment of circulating tumor cells in tumor-bearing mouse blood by a deterministic lateral displacement microfluidic device. *Biomed. Microdevices*, 17(3):59, jun 2015. ISSN 1387-2176.

[107] J. A. Davis, D. W. Inglis, K. J. Morton, D. A. Lawrence, L. R. Huang, S. Y. Chou, J. C. Sturm, and R. H. Austin. Deterministic hydrodynamics: Taking blood apart. *Proc. Natl. Acad. Sci.*, 103(40):14779–14784, oct 2006. ISSN 0027-8424.

[108] Benjamin H Wunsch, Joshua T Smith, Stacey M Gifford, Chao Wang, Markus Brink, Robert L Bruce, Robert H Austin, Gustavo Stolovitzky, and Yann Astier. Nanoscale lateral displacement arrays for the separation of exosomes and colloids down to 20 nm. *Nat. Nanotechnol.*, (August), 2016. ISSN 1748-3387.

[109] Peter Galajda, Juan Keymer, Paul Chaikin, and Robert Austin. A Wall of Funnels Concentrates Swimming Bacteria. *J. Bacteriol.*, 189(23):8704–8707, dec 2007. ISSN 0021-9193.

[110] Kun-Ta Wu, Jean Bernard Hishamunda, Daniel T. N. Chen, Stephen J. DeCamp, Ya-Wen Chang, Alberto Fernández-Nieves, Seth Fraden, and Zvonimir Dogic. Transition from turbulent to coherent flows in confined three-dimensional active fluids. *Science (80-.).*, 355(6331):eaal1979, may 2017. ISSN 0036-8075.

[111] S. Elizabeth Hulme, Willow R. DiLuzio, Sergey S. Shevkoplyas, Linda Turner, Michael Mayer, Howard C. Berg, and George M. Whitesides. Using ratchets and sorters to fractionate motile cells of Escherichia coli by length. *Lab Chip*, 8(11):1888, 2008. ISSN 1473-0197.

[112] H A Guidobaldi, Y Jeyaram, C A Condat, M Oviedo, I Berdakin, V V Moshchalkov, L C Giojalas, A. V. Silhanek, and V. I. Marconi. Disrupting the wall accumulation of human sperm cells by artificial corrugation. *Biomicrofluidics*, 9(2):024122, mar 2015. ISSN 1932-1058.

[113] Bao-quan Ai, Qiu-yan Chen, Ya-feng He, Feng-guo Li, and Wei-rong Zhong. Rectification and diffusion of self-propelled particles in a two-dimensional corrugated channel. *Phys. Rev. E*, 88(6):062129, dec 2013. ISSN 1539-3755.

[114] Bahman Delalat, Vonda C. Sheppard, Soraya Rasi Ghaemi, Shasha Rao, Clive A. Prestidge, Gordon McPhee, Mary-louise Rogers, Jacqueline F Donoghue, Vinochani Pillay, Terrance G Johns, Nils Kröger, and Nicolas H Voelcker. Targeted drug delivery using genetically engineered diatom biosilica. *Nat. Commun.*, 6:8791, nov 2015. ISSN 2041-1723.

[115] Ouajdi Felfoul, Mahmood Mohammadi, Samira Taherkhani, Dominic de Lanauze, Yong Zhong Xu, Dumitru Loghin, Sherief Essa, Sylwia Jancik, Daniel Houle, Michel Lafleur, Louis Gaboury, Maryam Tabrizian, Neila Kaou, Michael Atkin, Té Vuong, Gerald Batist, Nicole Beauchemin, Danuta Radzioch, and Sylvain Martel. Magneto-aerotactic bacteria deliver drug-containing nanoliposomes to tumour hypoxic regions. *Nat. Nanotechnol.*, 11(11):941–947, nov 2016. ISSN 1748-3387.

[116] James R Baylis, Ju Hun Yeon, Max H Thomson, Amir Kazerooni, Xu Wang, A. E. St. John, Esther B Lim, Diana Chien, Anna Lee, Jesse Q Zhang, James M Piret, Lindsay S Machan, Thomas F Burke, Nathan J White, Christian J Kastrup, Alex E St John, Esther B Lim, Diana Chien, Anna Lee, Jesse Q Zhang, James M Piret,

Lindsay S Machan, Thomas F Burke, Nathan J White, and Christian J Kastrup. Self-propelled particles that transport cargo through flowing blood and halt hemorrhage. *Sci. Adv.*, 1(9):e1500379–e1500379, oct 2015. ISSN 2375-2548.

[117] Andreas Kaiser, Anton Peshkov, Andrey Sokolov, Borge ten Hagen, Hartmut Löwen, and Igor S. Aranson. Transport Powered by Bacterial Turbulence. *Phys. Rev. Lett.*, 112(15):158101, apr 2014. ISSN 0031-9007.

[118] Andreas Kaiser, Andrey Sokolov, Igor S. Aranson, and Hartmut Löwen. Motion of two micro-wedges in a turbulent bacterial bath. *Eur. Phys. J. Spec. Top.*, 224(7): 1275–1286, jul 2015. ISSN 1951-6355.

[119] A. Kaiser. *Emergent states in active fluids : From bulk to confinement.* PhD thesis, Heinrich Heine University Düsseldorf, 2014.

[120] Hoyeon Kim and Min Jun Kim. Electric Field Control of Bacteria-Powered Microrobots Using a Static Obstacle Avoidance Algorithm. *IEEE Trans. Robot.*, 32(1): 125–137, feb 2016. ISSN 1552-3098.

[121] Shuqiang Huang, Anna Jisu Lee, Ryan Tsoi, Feilun Wu, Ying Zhang, Kam W Leong, and Lingchong You. Coupling spatial segregation with synthetic circuits to control bacterial survival. *Mol. Syst. Biol.*, 12(2):1–13, 2016. ISSN 1744-4292.

[122] R. Di Leonardo, L. Angelani, D. Dell'Arciprete, G. Ruocco, V. Iebba, S. Schippa, M. P. Conte, F. Mecarini, F. De Angelis, and E. Di Fabrizio. Bacterial ratchet motors. *Proc. Natl. Acad. Sci.*, 107(21):9541–9545, may 2010. ISSN 0027-8424.

[123] Shengtao Lu, Fang Liu, Bengang Xing, and Edwin K L Yeow. Nontoxic colloidal particles impede antibiotic resistance of swarming bacteria by disrupting collective motion and speed. *Phys. Rev. E - Stat. Nonlinear, Soft Matter Phys.*, 92(6):1–10, 2015. ISSN 15502376.

[124] Kai Jian Huang, S. J. Qin, Zhong Chen Bai, Xin Zhang, and John D. Mai. Entropy-based separation of yeast cells using a microfluidic system of conjoined spheres. *J. Appl. Phys.*, 114(19), 2013. ISSN 00218979.

[125] George B. Arfken. *Mathematical Methods for Physicists.* Orlando, FL: Academic Press, 3rd edition, 1985.

[126] Fernando Peruani, Andreas Deutsch, and Markus Bär. Nonequilibrium clustering of self-propelled rods. *Phys. Rev. E*, 74(3):030904, sep 2006. ISSN 1539-3755.

[127] Hui-Shun Kuan, Robert Blackwell, Loren E. Hough, Matthew A. Glaser, and M. D. Betterton. Hysteresis, reentrance, and glassy dynamics in systems of self-propelled rods. *Phys. Rev. E*, 92(6):060501, dec 2015. ISSN 1539-3755.

[128] S. Broersma. Rotational Diffusion Constant of a Cylindrical Particle. *J. Chem. Phys.*, 32(6):1626–1631, jun 1960. ISSN 0021-9606.

[129] S. Broersma. Viscous Force Constant for a Closed Cylinder. *J. Chem. Phys.*, 32(6): 1632–1635, jun 1960. ISSN 0021-9606.

[130] M. Mercedes Tirado, Carmen López Martínez, and José García de la Torre. Comparison of theories for the translational and rotational diffusion coefficients of rod-like macromolecules. Application to short DNA fragments. *J. Chem. Phys.*, 81(4):2047–2052, aug 1984. ISSN 0021-9606.

[131] Knut Drescher, Jörn Dunkel, Luis H. Cisneros, Sujoy Ganguly, and Raymond E. Goldstein. Fluid dynamics and noise in bacterial cell – cell and cell – surface scattering. *Proc. Natl. Acad. Sci.*, 108:10940–10945, 2011.

[132] Taro Kihara. Convex Molecules in Gaseous and Crystalline States. In I. Prigogine, editor, *Adv. Chem. Phys.*, chapter 3, pages 147–188. John Wiley & Sons, Ltd, jan 1963. ISBN 9780470143513.

[133] Th. Kirchhoff, H. Löwen, and R. Klein. Dynamical correlations in suspensions of charged rodlike macromolecules. *Phys. Rev. E*, 53(5):5011–5022, 1996. ISSN 1063-651X.

[134] Masoud Abkenar, Kristian Marx, Thorsten Auth, and Gerhard Gompper. Collective behavior of penetrable self-propelled rods in two dimensions. *Phys. Rev. E*, 88(6): 062314, dec 2013. ISSN 1539-3755.

[135] Michael P. Allen and Dominic J. Tildesley. *Computer Simulation of Liquids*. Oxford University Press, Oxford, 2nd editio edition, nov 2017. ISBN 9780198803195.

[136] Lawrence R. Pratt and Steven W. Haan. Effects of periodic boundary conditions on equilibrium properties of computer simulated fluids. I. Theory. *J. Chem. Phys.*, 74 (3):1864–1872, feb 1981. ISSN 0021-9606.

[137] D. Frenkel. Simulations: The dark side. *Eur. Phys. J. Plus*, 128(1):10, jan 2013. ISSN 2190-5444.

[138] Sebastian Weitz, Andreas Deutsch, and Fernando Peruani. Self-propelled rods exhibit a phase-separated state characterized by the presence of active stresses and the ejection of polar clusters. *Phys. Rev. E*, 92(1):012322, jul 2015. ISSN 1539-3755.

[139] A. Kaiser, H. H. Wensink, and H. Löwen. How to capture active particles. *Phys. Rev. Lett.*, 108(26):268307, feb 2012. ISSN 0031-9007.

[140] R. Di Leonardo, D. Dell'Arciprete, L Angelani, and V Iebba. Swimming with an Image. *Phys. Rev. Lett.*, 106(3):038101, jan 2011. ISSN 0031-9007.

[141] Urs Zimmermann, Frank Smallenburg, and Hartmut Löwen. Flow of colloidal solids and fluids through constrictions: dynamical density functional theory versus simulation. *J. Phys. Condens. Matter*, 28(24):244019, jun 2016. ISSN 0953-8984.

[142] R Hockney and J Eastwood. *Computer Simulation Using Particles*. Taylor & Francis, jan 1988. ISBN 978-0-85274-392-8.

[143] Pedro Gonnet. A simple algorithm to accelerate the computation of non-bonded interactions in cell-based molecular dynamics simulations. *J. Comput. Chem.*, 28(2): 570–573, jan 2007. ISSN 01928651.

[144] Mahdi Zarif and Ali Naji. Confinement-induced alternating interactions between inclusions in an active fluid. dec 2019.

[145] Andrew J. King, Alan M. Wilson, Simon D. Wilshin, John Lowe, Hamed Haddadi, Stephen Hailes, and A. Jennifer Morton. Selfish-herd behaviour of sheep under threat. *Curr. Biol.*, 22(14):R561–R562, jul 2012. ISSN 09609822.

[146] Dirk Helbing. Traffic and related self-driven many-particle systems. *Rev. Mod. Phys.*, 73(4):1067–1141, dec 2001. ISSN 0034-6861.

[147] Fernando Peruani, Jörn Starruß, Vladimir Jakovljevic, Lotte Søgaard-Andersen, Andreas Deutsch, and Markus Bär. Collective Motion and Nonequilibrium Cluster Formation in Colonies of Gliding Bacteria. *Phys. Rev. Lett.*, 108(9):098102, feb 2012. ISSN 0031-9007.

[148] Eshel Ben-Jacob, Alin Finkelshtein, Gil Ariel, and Colin Ingham. Multispecies Swarms of Social Microorganisms as Moving Ecosystems. *Trends Microbiol.*, 24(4): 257–269, apr 2016. ISSN 0966842X.

[149] Bella Ilkanaiv, Daniel B. Kearns, Gil Ariel, and Avraham Be'er. Effect of Cell Aspect Ratio on Swarming Bacteria. *Phys. Rev. Lett.*, 118(15):158002, apr 2017. ISSN 0031-9007.

[150] Qun Chen and Bao-quan Ai. Sorting of chiral active particles driven by rotary obstacles. *J. Chem. Phys.*, 143(10):104113, sep 2015. ISSN 0021-9606.

[151] Mite Mijalkov and Giovanni Volpe. Sorting of chiral microswimmers. *Soft Matter*, 9 (28):6376, dec 2013. ISSN 1744-683X.

[152] Bao-quan Ai, Ya-feng He, and Wei-rong Zhong. Chirality separation of mixed chiral microswimmers in a periodic channel. *Soft Matter*, 11(19):3852–3859, may 2015. ISSN 1744-683X.

[153] Enys Mones, András Czirók, and Tamás Vicsek. Anomalous segregation dynamics of self-propelled particles. *New J. Phys.*, 17(6):063013, jun 2015. ISSN 1367-2630.

[154] Elshad Allahyarov and Hartmut Löwen. Length segregation in mixtures of spherocylinders induced by imposed topological defects. *Soft Matter*, 14(44):8962–8973, mar 2018. ISSN 1744-683X.

[155] Arman Boromand, Alexandra Signoriello, Janna Lowensohn, Carlos S. Orellana, Eric R. Weeks, Fangfu Ye, Mark D. Shattuck, and Corey S. O'Hern. The role of deformability in determining the structural and mechanical properties of bubbles and emulsions. *Soft Matter*, 15(29):5854–5865, apr 2019. ISSN 1744-683X.

[156] Daniel de las Heras and Matthias Schmidt. Better Than Counting: Density Profiles from Force Sampling. *Phys. Rev. Lett.*, 120(21):218001, may 2018. ISSN 0031-9007.

[157] Kristian Marx. *Self-propelled rod-like swimmers near surfaces*. PhD thesis, University of Cologne, 2011.

[158] H. A. Lorentz. Ueber die Anwendung des Satzes vom Virial in der kinetischen Theorie der Gase. *Ann. Phys.*, 248(1):127–136, 1881. ISSN 00033804.

[159] P. M. Chaikin and T. C. Lubensky. *Principles of condensed matter physics*. Cambridge University Press, Cambridge, 1995. ISBN 9780511813467.

[160] Andrea Cavagna, Silvio M. Duarte Queiros, Irene Giardina, Fabio Stefanini, and Massimiliano Viale. Diffusion of individual birds in starling flocks. *Proc. R. Soc. B Biol. Sci.*, 280(1756):20122484–20122484, jun 2012. ISSN 0962-8452.

[161] Silke Henkes, Yaouen Fily, and M. Cristina Marchetti. Active Jamming: Self-propelled soft particles at high density. *Phys. Rev. E*, 84(4):040301, jul 2011. ISSN 1539-3755.

[162] V. Narayan, S. Ramaswamy, and N. Menon. Long-Lived Giant Number Fluctuations in a Swarming Granular Nematic. *Science (80-.).*, 317(5834):105–108, jul 2007. ISSN 0036-8075.

[163] Corneel Casert. *Emergent collective motion from local interactions*. PhD thesis, Ghent University, 2017.

[164] Hugues Chaté, Francesco Ginelli, and Raúl Montagne. Simple Model for Active Nematics: Quasi-Long-Range Order and Giant Fluctuations. *Phys. Rev. Lett.*, 96(18): 180602, may 2006. ISSN 0031-9007.